

Dissertation  
in partial fulfilment of the degree  
Doctor rerum naturalium (Dr. rer. nat.)

# REVERBERATING BRAIN BITS

SCRUTINIZING INFORMATION ROUTING BY SYNCHRONIZATION

submitted by  
DMITRIY LISITSYN, M.Sc.

Date of Defense: December 21st, 2021

Bremen University  
Department of Physics  
Institute for Theoretical Physics

SUPERVISORS/GUTACHTER:  
Dr. Udo Ernst  
Prof. Dr. Andreas Kreiter

Dmitriy Lisitsyn

*Reverberating Brain Bits: Scrutinizing Information Routing by Synchronization*

December 2021

## ABSTRACT

---

At any given moment, the brain is subjected to a barrage of sensory information from the environment around us. Selective attention allows to focus on the behaviourally-relevant subset within this overwhelming information stream, depending on the task at hand, and ignore the rest. Attended signals are routed through to deeper parts of the brain, getting processed and reaching awareness, whereas the routing of non-attended signals is suppressed. Despite extensive evidence for attention-dependent changes in neural activity, the mechanism behind such flexible routing of information is not well understood.

One possibility is proposed by the routing by synchrony (RBS) mechanism – wherein modulation of effective connectivity between neural populations is established by gamma-rhythmic synchronization and coherence of their neural activities. Neural populations receiving attended signals can align their gamma-rhythmic activity to that of the sending populations, such that incoming spikes would arrive when the receiving population is most excitable, enhancing signal transfer. Conversely, non-attended signals arrive unaligned to the receiver’s rhythm, reducing their transfer. Experimental studies have already provided correlative evidence that gamma-rhythmic coherence between populations processing visual stimuli is modulated by attention. However, it remains to be shown whether the observed synchronization and coherence phenomena are responsible for flexible information routing causally. Here, we investigate RBS using two complementary approaches, aiming to establish a causal link between physiological phenomena and the neural mechanisms responsible for selective information processing.

In the first project, we make a prediction, based on previous experimental findings and the theory behind the RBS mechanism – information encoded within neural activity should itself be conveyed through gamma-rhythmic packages. To investigate this prediction, we perform an intricate analysis on neural recordings collected from monkeys performing a visual selective attention task, which utilized visual stimuli allowing to assess their information content within neural activity. New methods are developed, allowing to compute how stimulus information content depends on the gamma phase and amplitude of neural activity. The results are in agreement with the prediction, showing that stimulus information is indeed conveyed via gamma-rhythmic packages, in support of the RBS mechanism.

In the second project, via a modeling approach, we investigate the consequences of direct microstimulation of neural circuits involved in selective attention. Using stimulation pulses in order to control gamma-rhythmic coherence between neural populations would allow to directly test the efficacy of the RBS mechanism and potentially control information routing itself. We propose a method that relies on the inherent oscillatory dynamics of the system – applying minimal stimulation to nudge the natural activity of the network into a desired state. A closed-loop stimulation paradigm is developed, based on the phase-response characteristics of a biophysically realistic network performing selective routing of information. This allows us measure the contamination of stimulus information content by artificial pulses. Within the scope of our model, we demonstrate that precisely timed perturbations can be used to artificially induce the effect of attention by selectively routing visual signals to higher cortical areas and pinpoint caveats and limitations of utilizing this approach in vivo.



## PUBLICATIONS

---

Some ideas and figures presented in the dissertation have appeared previously in the following publications and conference presentations:

1. **Lisitsyn D.**, Grothe I., Kreiter A., and Ernst U. "Visual stimulus content in V4 is conveyed by gamma-rhythmic information packages". *The Journal of Neuroscience* **40** (Dec. 2020), pp. 9650-9662. doi: <https://doi.org/10.1523/jneurosci.0689-20.2020>
2. **Lisitsyn D.** and Ernst U. "Causally investigating cortical dynamics and signal processing by targeting natural system attractors with precisely timed (electrical) stimulation". *Frontiers in Computational Neuroscience* **13.7** (Feb. 2019). doi: <https://doi.org/10.3389/fncom.2019.00007>
3. **Lisitsyn D.**, Drebitz E., Grothe I., Kreiter A., and Ernst U. "Dissecting gamma phase and amplitude-specific information routing in V4 of macaque during selective attention". *BMC Neuroscience 2017 (CNS Antwerp)* Talk 18(Suppl 1):O14. doi: <https://doi.org/10.1186/s12868-017-0370-3>
4. **Lisitsyn D.** and Ernst U. "Model-based inferences into attention and bistability information routing control via precisely-timed perturbations". *Bernstein Conference 2016, Berlin*. Poster T34. doi: <https://doi.org/10.12751/nncn.bc2016.0158>
5. Rothe H., Stemmann H., Schander A., **Lisitsyn D.**, Kreiter A., Lang W., and Ernst U. "Analysis of neural signals from chronically implanted, novel multi-channel floating probes". *Bernstein Conference 2016, Berlin*. Poster T46. doi: <https://doi.org/10.12751/nncn.bc2016.0170>
6. **Lisitsyn D.**, Harnack D., and Ernst U. "Probing communication through coherence via phase-dependent analysis". *Society for Neuroscience (SfN) Annual Meeting 2015*. Poster 331.19(Q15)
7. **Lisitsyn D.**, Harnack D., and Ernst U. "Probing information routing mechanisms by precisely-timed electrical stimulation pulses: a modelling study". *BMC Neuroscience 2015 (CNS Prague)* Poster P70. doi: <https://doi.org/10.1186/1471-22.02-16-s1-p70>
8. **Lisitsyn D.**, Harnack D., and Ernst U. "Guiding attention: phase-response curve analysis of a communication through coherence model". *Bernstein Conference 2014 (Göttingen)*. Poster W14. 2014. doi: <https://doi.org/10.12751/nncn.bc2014.0035>



# CONTENTS

---

<b>I</b>	<b>THE PRECURSOR</b>	1
1	MOTIVATION	3
1.1	Outline . . . . .	6
2	BRIEF NEUROSCIENCE PRIMER	9
2.1	Neurons . . . . .	9
2.2	Modelling a neuron . . . . .	10
2.3	Electrophysiology . . . . .	12
2.4	Neural network organization . . . . .	13
2.5	The visual system . . . . .	15
2.6	Selective attention . . . . .	18
2.6.1	Key concepts and psychology of attention . . . . .	18
2.6.2	The neuroscience of attention . . . . .	19
2.7	Rhythmic neural activity . . . . .	20
2.7.1	Local circuit oscillation mechanisms . . . . .	21
2.7.2	Binding by synchrony . . . . .	22
2.7.3	Routing by synchrony . . . . .	22
2.7.4	Neural rhythms and stimulation . . . . .	24
<b>II</b>	<b>ANIMAL DATA ANALYSIS</b>	25
3	INFORMATION IN V4 IS GAMMA-RHYTHMIC	27
3.1	Introduction . . . . .	27
3.2	Materials and Methods . . . . .	28
3.2.1	Experimental model and subject details . . . . .	28
3.2.2	Surgical procedures and behavioral task . . . . .	28
3.2.3	Recording . . . . .	30
3.2.4	Data preprocessing and site selection . . . . .	30
3.2.5	Data analysis . . . . .	32
3.3	Results . . . . .	36
3.3.1	Information modulation by phase . . . . .	37
3.3.2	Information modulation by amplitude . . . . .	40
3.3.3	Information modulation by phase and amplitude . . . . .	40
3.3.4	Controlling for eye-movements. . . . .	43
3.4	Discussion . . . . .	43
4	DELVING DEEPER INTO V4	47
4.1	Introduction . . . . .	47
4.2	Results and Discussion . . . . .	48
4.2.1	Identifying the layer of the recording site . . . . .	48
4.2.2	Deep layer: information modulation by phase . . . . .	50
4.2.3	Deep layer: information modulation by amplitude . . . . .	52
4.2.4	Deep layer: information modulation by phase and amplitude . . . . .	54
5	GAMMA-RHYTHMIC INFORMATION IN V1	57
5.1	Introduction . . . . .	57
5.2	Results and Discussion . . . . .	58
5.2.1	V1 data, laminar location of recordings . . . . .	58

5.2.2	V1 information modulation by phase . . . . .	59
5.2.3	Attentional modulation of V1-V4 coherence . . . . .	60
5.2.4	V1 information modulation relative to V4 gamma . . . . .	63
<b>III</b>	<b>STIMULATION SIMULATION</b>	<b>67</b>
<b>6</b>	<b>CONTROLLING GAMMA-RHYTHMIC COHERENCE WITH MICROSTIMULATION</b>	<b>69</b>
6.1	Introduction . . . . .	69
6.2	Results . . . . .	71
6.2.1	Part 1: Stimulating a single population . . . . .	71
6.2.2	Part 2: Stimulation bistable multi-population model . . . . .	79
6.3	Methods . . . . .	92
6.3.1	Neurons and synapses . . . . .	92
6.3.2	Offline phase measurement . . . . .	92
6.3.3	Realtime phase measurement . . . . .	93
6.3.4	Significance level computation . . . . .	93
6.3.5	Conditioning of input drive on internal noise . . . . .	93
6.3.6	PRC and PDRC collection details . . . . .	94
6.4	Discussion . . . . .	94
6.4.1	Intra-population connectivity . . . . .	96
6.4.2	Local circuitry . . . . .	96
6.4.3	Transient synchrony . . . . .	96
6.4.4	Modeling the perturbation . . . . .	97
6.4.5	Simulating different levels of background noise . . . . .	97
6.4.6	Simulating frequency jitter . . . . .	97
<b>IV</b>	<b>CUMULATIVE OUTLOOK</b>	<b>99</b>
<b>7</b>	<b>OUTLOOK</b>	<b>101</b>
7.1	Animal data analysis . . . . .	101
7.1.1	Laminar ambiguity . . . . .	101
7.1.2	Future research – laminar recordings in V1 and V4 . . . . .	102
7.1.3	Beyond gamma – attention is mediated by multiple rhythms . . . . .	103
7.2	Modeling stimulation in the visual system . . . . .	104
7.2.1	Microstimulation relying on inherent network dynamics . . . . .	104
7.2.2	Future research - expanding the model . . . . .	105
7.2.3	Future research - testing state-dependent stimulation in animals . . . . .	106
7.3	Conclusion . . . . .	106
	<b>BIBLIOGRAPHY</b>	<b>109</b>

Part I

THE PRECURSOR



MOTIVATION

---

"It from Bit. Otherwise put, every it – every particle, every field of force, even the spacetime continuum itself – derives its function, its meaning, its very existence entirely – even if in some contexts indirectly – from the apparatus-elicited answers to yes or no questions, binary choices, bits.

It from Bit symbolizes the idea that every item of the physical world has at bottom – at a very deep bottom, in most instances – an immaterial source and explanation; that what we call reality arises in the last analysis from the posing of yes-no questions and the registering of equipment-evoked responses; in short, that all things physical are information-theoretic in origin and this is a participatory universe."

—John Archibald Wheeler [243]

The brain is, essentially, an information-processing machine. Through various sensory organs, it receives data from the outside world. This input data is routed throughout the brain, integrated, filtered and transformed, allowing an organism to attain some level of awareness about the world. Then, information from the brain is fed back into various muscles throughout the body, resulting in actions and behaviour. In other words, information processing is at the heart of all the cognitive functions performed by the brain, including processes such as attention, formation of knowledge, memory, making predictions, performing judgment and evaluation, reasoning, problem solving and decision making. The integration and computation of information involved in these functions involves the coordinated interaction of large neuron ensembles distributed within and across different brain areas. How this coordination is achieved is one of the fundamental and yet unresolved problems of modern neuroscience.

A critical component underlying the coordination of information throughout the brain is its ability to flexibly adapt and allocate resources appropriately depending on the context. A good practical example of this is provided by what is called the *cocktail party effect* [8]: in a noisy room with many ongoing conversations and music playing in the background, a person can focus on just one speaker, allowing to process and comprehend the contents from the desired source clearly, while filtering out the rest of the auditory input. This is a complex computational problem, since the voices of all speakers are superimposed into a single waveform received by our ears. One can switch the focus of attention between multiple speakers quickly. Crucially, the speed at which the brain can switch between different tasks and computational configurations is too fast to be explained by changes and adaptation of its anatomy, the physical connections within its neuronal circuits. This means that there has to be some functional mechanism that allows to flexibly modulate the effective strength of connections throughout the brain. The mechanism behind this context and task-dependent modulation of effective connectivity [3] is at the heart of cognition, allowing humans and other organisms to adapt their behaviour in response to changing context and task demands [3, 82, 83, 89]. What sort of a neural network configurations does the brain utilize that would allow for fast and flexible modulation of effective connectivity? How is flexible processing achieved?

The cocktail party effect presented above is an example of *selective attention*, one of the major cognitive functions relying on effective connectivity. Selective attention is the ability to allocate information processing resources to a selected, behaviourally relevant,

subset of the input sensory information – attention guides the flow of information. Without it, our brains would be overwhelmed by the vast amount of information present in the world, unable to filter out irrelevant information and focus on the relevant components. Studies on selective attention, in particular within the visual system, have made for a major source of insight on the possible mechanism behind modulation of effective connectivity.

The visual system consists of a hierarchy of brain areas, with a repeating pattern of convergent feedforward connectivity – with neurons in lower areas sending fanned-in projections to neurons in higher up areas [224]. A direct consequence of this convergent connectivity is the increase in the sizes of receptive fields (portion of visual field that a neuron is responsive to) as one goes up the visual hierarchy – neurons higher up in the hierarchy combine inputs from multiple neurons with smaller receptive fields from the preceding areas of the visual hierarchy. This makes it possible to set up a controlled experiment, presenting two neighboring visual stimuli, such that each stimulus is within a distinct receptive field of a neural population lower in the hierarchy, and both stimuli are within the receptive field on the higher-up population (Fig. 1).

A seminal study performed by Moran and Desimone in 1985 [163] utilized this setup. The researchers trained monkeys on a task to selectively attend to one of two neighboring oriented bar stimuli and ignore the other. Recordings of neural activity were collected from the lower area V1 (with each neuron’s receptive field containing just one stimulus) and the higher areas V4 and IT (with receptive fields containing both stimuli). The results showed that firing rate of neurons in the higher-up visual areas V4 and IT was as if just the attended stimulus is present. Simultaneously, the firing rate of neurons in the preceding visual area V1, the source of the feedforward input to V4 and IT, was seemingly unaffected by attention. In other words, the experiment demonstrated that attention modulates the effective connectivity from V1 neurons to neurons in V4/IT, crucially, through a mechanism that does not rely on firing rates alone. So, what sort of a neural mechanism would allow neural circuits to adapt the effective connectivity between its cells?

The research presented in this dissertation explores a prominent theory proposing one such mechanism, referred to as *routing by synchrony* (RBS) [98, 99, 122, 123] or *communication through coherence* (CTC) [77, 79]. The mechanism utilizes rhythmic neural

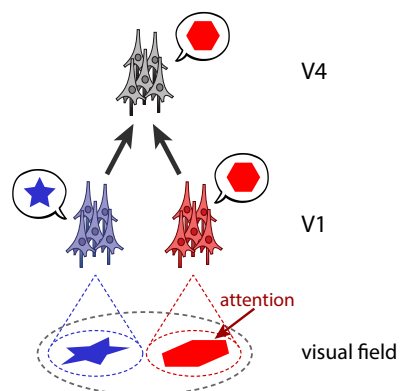


**Figure 1.1: Experimental setup and network configuration showcasing selective routing of information.** Two visual stimuli are presented within the visual field. The receptive field of each V1 population contains one stimulus. Both of these populations project to the same V4 population, whose receptive field contains both stimuli. When one of the stimuli is attended, the activity in V1 populations does not change, but V4 responds as if just the attended stimulus is present.

activity in the gamma frequency range (40-100Hz) – neurons processing visual stimuli have been found to exhibit oscillatory activity, with neighboring neurons synchronizing the discharge of their output into gamma-rhythmic bursts [80, 114]. The central idea behind the mechanism proposes that gamma rhythms in sending and receiving neurons (or local populations of neurons) can synchronize, establishing coherence between the rhythms with an appropriate, favorable phase-coupling such that the bursts of spikes from the sending neurons arrive to the receiving neurons when they are most excitable during their gamma cycle, enhancing the transfer of information. Conversely, sending and receiving neurons could also establish coherence at with an unfavorable phase-coupling, such that the bursts of spikes arrive to the receiving neurons when they are least excitable, suppressing information transfer. In this manner, effective connectivity between neurons can be modulated by controlling the phase, as well as the overall level of gamma-rhythmic coherence between them.

In support of the RBS mechanism, in 2012, two independent studies utilized a similar experimental setup described above, showing that V1 neurons processing an attended stimuli do establish coherence with the downstream V4 neurons, whereas V1 neurons processing non-attended stimuli establish little or no coherence with the receiving V4 cells [29, 98]. However, this experimental evidence was purely correlative in nature, unable to show a causal link between gamma-rhythmic coherence and modulation of effective connectivity. Cumulatively, whether rhythmic activity serves a functional role or not remains a subject of debate in the scientific community, with the opposing view stating that the observed gamma-rhythmic synchronization could merely be an epiphenomenon, a side effect of neural circuitry without functional significance [157, 200].

Working out the intricacies of how neural circuitry achieves flexible information routing could have major implications for clinical neuroscience. From an information theoretic point of view, cognitive dysfunction can be thought of as the inability of neural circuitry to properly coordinate and process information. Further, there is a substantial body of research providing evidence that cognitive dysfunction is associated with abnormal rhythmic activity in the gamma-frequency range, with studies showing such a link across a wide spectrum of disorders [14, 222]: Parkinson's [241], Alzheimer's [208, 223], schizophrenia [127, 133], attention-deficit/hyperactivity [11, 135], anxiety [174], major depression [74], bipolarity [137], etc. Some clinical studies have successfully employed targeted stimulation paradigms in order to stimulate specific brain regions at a particular frequency in order to alleviate cognitive impairment in human subjects [141, 199]. However, most such studies utilized high frequency (130Hz) stimulation, in a purely experimental manner, without theoretical underpinnings explaining how or why a particular stimulation protocol affects information processing [143]. Finding causal support for the role of gamma in neural information processing would allow the clinical research to make major translational progress, moving from speculative observational evidence towards concrete methods to identify and treat such disorders [86].

Further insight into how the brain achieves flexible information routing could also lead to advancements in the research field of artificial intelligence and machine learning. In the past decade, *deep convolutional network* algorithms have led to major breakthroughs, allowing to achieve unprecedented performance in specialized tasks such object [125] and speech [108] recognition, as well as more complex tasks such as surpassing previous human and algorithm performance at games such as chess [203] and Go [202]. The structure of deep convolutional networks was inspired by neuroscience. Here, "deep" stands for a network having many layers of neuron-like units. Lower layers contain more units, such that the connectivity from lower to higher layers is convergent.

This results in having features represented by units in one layer of the artificial network combined to represent more abstract features in the next layer, analogous to the hierarchical processing found in visual system of the human brain [224]. However, a prominent factor present in networks used in machine learning is their lack of flexibility – artificial neural networks fail to adapt and generalize across different stimuli domains or tasks – for instance, a network trained to detect and identify human faces fails miserably at detecting anything else. Thus, major efforts are employed in order to produce what is referred to as *artificial general intelligence* – an intelligent algorithm that would be capable to generalize previously acquired knowledge, attaining the ability to understand and learn any intellectual task that a human can [20, 95]. Some of the recent advances in the field have employed new algorithms, called *transformers*, which enact a form attention called *soft attention* within the system, allowing units within a layer to dynamically select which inputs from the previous layer to operate on, in particular improving performance on tasks with temporal components, e.g. the order of words during a language translation task [228]. While all of this sounds analogous to the role of attention in the brain, the new transformer architecture does not utilize any sort of oscillators producing rhythmic activity. Further research towards understanding the role of the brain’s rhythmic activity could potentially be the key to move the field closer to producing general artificial intelligence [233, 234].

In summary, modulation of effective connectivity between neurons is critical for cognition, allowing for flexible routing of information across brain areas. A visual selective attention task serves as the paradigmatic experiment relying on modulation of effective connectivity – two visual stimuli are each processed by distinct V1 neurons, which project onto the same V4 neurons. Information transfer between V1 and V4 is enhanced for V1 neurons processing attended stimuli, and suppressed for non-attended stimuli. Experimental evidence shows that such flexible attention-dependent information routing cannot not rely purely on neural firing rates. Rather, a mechanism relying on gamma-rhythm coherence between activities of sending and receiving neurons is proposed – routing by synchrony. Further investigation into the mechanism would shed light on how the brain achieves modulation of effectively connectivity and has further potential to impact clinical neuroscience and machine learning research. Can we find experimental support linking information routing directly to observed gamma dynamics? Is it possible to control information routing by controlling gamma-rhythmic coherence between neural populations?

## 1.1 OUTLINE

The proceeding dissertation is organized in the following manner:

- Chapter 2 provides an expanded introduction, starting from basic neuroscience principles that then build up to a comprehensive review of the history and existing literature on the subject of the gamma-rhythmic information routing mechanism.
- Part II, composed of three chapters, presents a series of data analyses performed on V1 and V4 neural activity recordings collected from two monkeys performing a visual selective attention task using a similar configuration to the one employed by Moran and Desimone 1985 [163], utilizing visual stimuli that allow to compute their information content within neural activity. The data set was collected and presented by Grothe et al 2018 [99], which showed that V4 neural activity contains significantly more attended than non-attended stimulus content. We utilize

this data-set to perform an analysis exploring the role of gamma-rhythmic synchronization and coherence in attention-dependent information routing from V1 to V4.

In Chapter 3, we propose a hypothesis, built upon existing experimental evidence on attention-dependent gamma synchronization and coherence between V1 and V4. The hypothesis states that if attentional information routing utilizes the RBS mechanism, then we expect that attended stimulus information content within V4 to be conveyed through gamma-rhythmic packages, whereas non-attended information content should exhibit no such effect. We develop a method that allows us to extract gamma phase- and amplitude-dependent signal information content within neural activity. This allows us to directly test the hypothesis, with the results showing that attention-dependent stimulus information content is modulated by V4's gamma rhythm. In chapter 4, we investigate gamma rhythm's role for feedback, as opposed to feedforward information processing. In chapter 5, we explore the role of gamma synchronization on stimulus information content within V1 as well as the role of gamma coherence between V1 and V4 on information routing. Cumulatively, the results from the chapters show a direct link between gamma-rhythmic synchronization/coherence and feedforward attention-dependent information routing, confirming our hypothesis and showing a direct and causal link between stimulus information routing and gamma-rhythmic activity.

- In part III, we propose a closed-loop stimulation paradigm in order to control gamma coherence between sending and receiving neurons, while observing the impact on information routing. Using microstimulation pulses in order to control coherence would allow to directly test the efficacy of the RBS mechanism. The closed-loop algorithm utilizes minimal electric perturbations, by relying on real-time state of the system, in order to work out the appropriate moment in time to apply a single electric perturbation in order achieve a desired phase coupling between neural populations. This approach is unique, since many experimental and clinical paradigms have employed continuous periodic stimulation in order to establish and maintain a desired effect, without consideration for state of the system. The paradigm is tested within a biophysically-constrained model of neural populations akin to the V1 and V4 populations processing stimuli during a selective attention task. In order to make the activity of the model comparable to real neuron activity, we test the efficacy of the paradigm for models affected by increasing levels of noise. Cumulatively, by testing the paradigm within the model, we develop and prepare all the necessary tools to perform a similar experiment in vivo. Such an experiment would provide conclusive evidence resolving any doubt concerning the RBS mechanism. Further, the proposed approach – relying on system state, minimizing the amount of the electric stimulation, and combined with concrete understanding of the underlying network dynamics – could enable further progress in clinical studies on cognitive disorders.
- Finally, in part IV, the outlook, we discuss and expand on the impact of the performed investigations. Various challenges faced throughout the research projects are addressed. We expand beyond the scope of the presented research by discussing the role of gamma within the bigger picture, the role of other rhythms and their interaction with gamma. Utilizing the insight acquired throughout the performed projects, we propose a series of further experiments, data analyses and models in order to further understand the role of neural rhythms in cognition.



## 2.1 NEURONS

Neurons are the fundamental units of the brain, responsible for acquiring, processing and disseminating information about an organism's body and its environment. They do so by sending and receiving electro-chemical signals across wide networks of interconnected units forming the neural circuitry of the brain. The main components of a neuron are the *soma* – the body of the cell, *dendrites* – extensions with many tree-like branches where the neuron receives signals from other cells, and an *axon* – a long (up to a meter or more!) cable-like projection that ends in branched terminals responsible for delivering signals to other cells. The axon terminals of one cell terminate at the dendrites of another cell at a location called the *synapse* – signals travelling down the axon of the presynaptic (or sending, or upstream) cell get transmitted to the dendrites of the postsynaptic (or receiving, or downstream) cell.

A neuron is not intrinsically a good conductor of electricity, rather relying on elaborate mechanisms that generate electrical signals based on the flow of ions (e.g.  $K^+$ ,  $Na^+$ ,  $Cl^-$ ,  $Ca^{2+}$ ) across the cell's plasma membrane. The flow of ions across the membrane is controlled by *ion channels* and *ion pumps* – complex proteins embedded within the cell's membrane. Ion pumps consume energy in order to transfer ions against the concentration gradient, establishing and maintaining a difference of ion concentrations inside and outside a cell. Ion channels let ions diffuse rapidly down the concentration gradient. For many types of ion channels, their permeability is controlled by the membrane potential – *voltage-gated channels*. By default, without any extra input currents into the cell, the overall flow of ions across the cell's membrane produces a negatively polarized equilibrium – the *resting membrane potential*, typically -40 to -90 mV.

If the membrane potential of a neuron becomes sufficiently depolarized (e.g. due to an input current),  $Na^+$  voltage-gated channels open up, causing a rapid flow of  $Na^+$  ions into the cell, causing rapid depolarization. Once the membrane potential is sufficiently high,  $K^+$  channels open, causing a flow of  $K^+$  ions out of the cell, rapidly re-polarizing the neuron and causing the  $Na^+$  channels to close again. This sudden opening and closing of ion channels within the cell body propagates down the cell's axon, producing an *action potential* (also called a *spike*). The action potential is an all-or-nothing event — for a specific cell, the magnitude of its action potentials are consistent, independent on how each one is initiated. Following an action potential, the cell needs some time, referred to as *refractory period*, to be ready to release another spike. The release of an action potential is often referred to as firing of the neuron, hence, *firing rate* refers to how many spikes are elicited by a neuron within a period of time. Multiple action potentials are often referred to as a *spike train*.

At the end of the axon, at the presynaptic terminal, an action potential results in the release of *neurotransmitters* from *synaptic vesicles* into the *synaptic cleft*, the space between the presynaptic axons and postsynaptic dendrites (for chemical synapses). These neurotransmitters bind to *receptors*, special channels within in the dendrites of the postsynaptic cell, activating them and resulting in a flow of ions across the postsynaptic cell's membrane that deflect the its membrane potential from its resting state. Crucially,

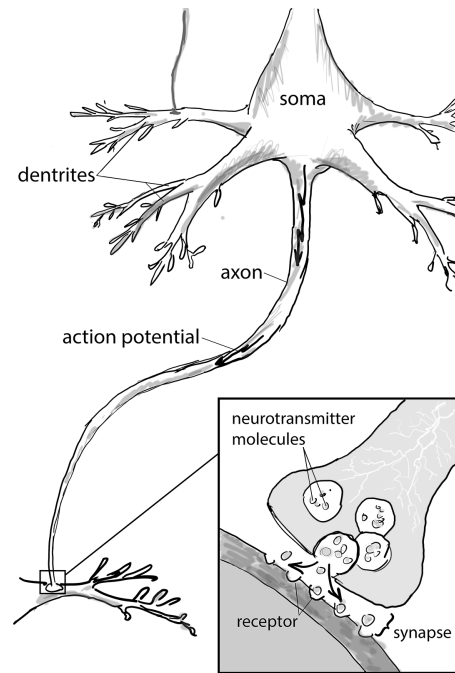


Figure 2.1: Neuron anatomy

a presynaptic neuron releases the same set of neurotransmitters from all of its axon terminals. This effectively means that for a particular neuron, the effect of its action potential can either depolarize/excite its post-synaptic targets, or hyperpolarize/inhibit its post-synaptic targets (bringing the membrane potential away from the firing threshold) – known as *Dale's principle* [212]. This leads to one of the major identifiers of neuron type — whether a cell is *excitatory* or *inhibitory*.

In addition to being identified as inhibitory or excitatory, there are many sub-types of neurons, varying across multiple attributes, such as the shape and spread of their dendrites, size of soma, axon length, etc. Of particular interest for our research, *interneurons* are relatively small inhibitory cells whose axons are relatively short, projecting locally to other cells in their vicinity. These units have been found to play a vital role in generating rhythmic neural activity [245] (covered in detail in a following section on brain rhythms). *Pyramidal neurons* are among the fundamental excitatory units; they project both locally and across larger distances across different areas of the brain.

Within the neural circuitry of the brain, a single neuron receives input from multiple (up to many thousands) of cells. Generally, the balance between input excitation and inhibition – *homeostasis* – ensures proper neural function [45, 235]. Too much inhibition and the post-synaptic neuron stays hyperpolarized and never fires; too much excitation and the neuron never stops firing. Cumulatively, a post-synaptic unit's spiking activity is rarely the same as that of its inputs. At each synaptic relay, the information content present within the input activity is transformed, for example amplifying or attenuating the signal from subsets of the input signals. Typically, a single neuron plays a relatively minor role within the scope of the network of interconnected units it belongs to.

## 2.2 MODELLING A NEURON

Neurophysics, in many cases synonymous with computational/theoretical/mathematical neuroscience, employs mathematical models, computational simulations and theo-

retical analysis in order to understand the principles behind brain function. Modeling studies aim to capture the essential features of a biological network by employing the appropriate levels of abstraction depending on the research scope and granularity of the analyzed biological system. For the research presented in this dissertation, we utilize single-neuron models that aim to recreate biologically plausible spiking activity.

A common way to model a single neuron is that of an electrical circuit, the input-output membrane voltage model, describing the relationship between the neuronal membrane currents at the input stage and the membrane voltage and spiking activity at the output stage in accordance to Kirchhoff's law. Such models generally consist of a set of nonlinear differential equations based on the time derivative of the law of capacitance:

$$C_m \frac{dV(t)}{dt} = - \sum_i I_i(t, V)$$

where on the left side of the equation,  $C_m$  is the cell's membrane capacitance,  $V$  is the membrane potential and on the right side we have the sum of the various currents  $I_i$  flowing through the membrane. A series of classical experiments by Hodgkin and Huxley from 1952 [110–113] utilized the voltage clamp method to work out the nonlinear equations of various voltage-dependent ionic currents of a giant squid neuron, providing a model that closely recreated the membrane's voltage behaviour including the generation and shape of action potentials. Each voltage-dependent ionic current was given by:

$$I(t, V) = g(t, V) \cdot (V - V_{eq})$$

where  $V_{eq}$  is the equilibrium potential for the specific ionic channel and  $g(t, V)$  is its voltage-gated conductance (inverse of resistance). The conductance for each channel is further expanded in terms of its maximal conductance  $\bar{g}$ , cumulatively resulting in the following voltage-current relationship accounting for a cell with sodium (Na) and potassium (K) channels:

$$C_m \frac{dV(t)}{dt} = -\bar{g}_K n^4 (V - V_K) - \bar{g}_{Na} m^3 h (V - V_{Na}) - \bar{g}_l (V - V_l)$$

Here,  $g_l$  stands for the constant conductance associated with current leaking out from the cell due to passive ionic channels.  $n$ ,  $m$  and  $h$  are dimensionless quantities between 0 and 1, determining the voltage-gating properties associated with potassium and sodium channels and ensuring that the action potential shape is similar to the biological one. Ultimately, for many studies including our own, one only needs to ensure the proper timing of the spikes, without much concern for their shape. For these purposes, it is common to utilize mathematically simpler models, such as the *leaky integrate-and-fire* (LIF) model.

LIF model describes a neuron's membrane voltage as a function of the input current, predicting the spike times without all of the biophysical details that shape an action potential. When the voltage of an LIF neuron reaches the threshold potential  $V_{th}$ , the neuron is said to have released a spike and its membrane potential is immediately reset back to the resting potential  $V_R$ . Otherwise, its behaviour can be described with a differential equation, similar to the Hodgkin-Huxley model:

$$C_m \frac{dV(t)}{dt} = -\bar{g}_l (V - V_l)$$

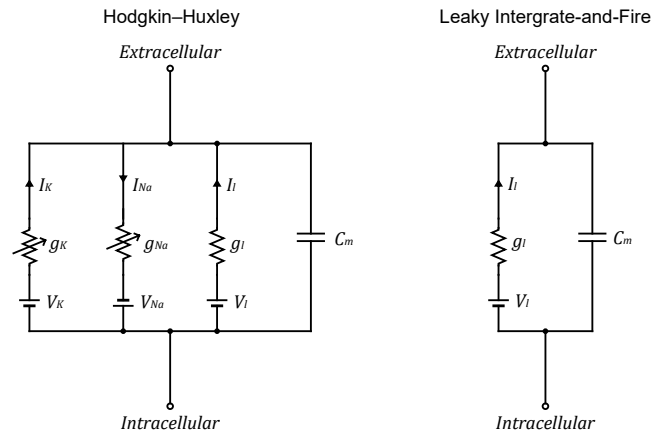


**Figure 2.2:** Electrical circuit diagrams for Hodgkin-Huxley and Leaky Integrate-and-Fire neuron models

Overall, there are quite many versions of similar conductance-based neuron models, adapted to recreate certain neuron behaviours, such as burst spiking, adaptation, synaptic plasticity, etc. In the modeling study presented in this dissertation, we used the *quadratic integrate-and-fire* model, covered in detail in the relevant chapter. This model is a reduction of the Hodgkin-Huxley model, keeping biophysically accurate behaviour of the cell's potential prior to releasing a spike, and utilizing the thresholding approach for spike generation from the LIF model.

### 2.3 ELECTROPHYSIOLOGY

A number of techniques are employed in order to record and study brain activity. Some techniques are *invasive*, involving surgical implantation of measuring devices, and some are *noninvasive*, allowing to access the brain activity without any surgery. Common non-invasive techniques, falling into the category of *neuroimaging*, include:

- *Functional Magnetic Resonance Imaging* (fMRI) – detects changes in the blood oxygenation throughout the brain that occur in response to neural activity. fMRI has a spatial resolution of a few millimeters and is capable of recording from the entire brain simultaneously, however the recorded signal has a rather low temporal resolution of multiple seconds.
- *Electroencephalography* (EEG) – records the electrical activity of the brain through electrodes placed on the surface of the scalp. It has a spatial resolution of about a centimeter and a temporal resolution of about a millisecond.
- *Magnetoencephalography* (MEG) – is similar to EEG but instead of sensing the electrical fields it records the magnetic fields generated by neural currents. Its spatial and temporal resolution are similar to EEG.

While the benefits of non-invasive techniques are paramount, their lack of spatial or temporal resolution does not allow to study the fine details of neural network dynamics and function, especially at the level of assessing the activity of individual neurons. *Electrophysiology* includes a number of invasive techniques, involving the insertion of electrodes directly into brain tissue. Of these, intracellular electrodes allow to record voltage and currents across the membrane of a single cell. Techniques involving intracellular recordings include:

- *Voltage clamp* – lets the experimenter "clamp" the voltage of a cell at a desired value, allowing to assess how ionic currents of a neuron behave at a specific voltage.
- *Current clamp* – keeps constant current into the cell to observe changes in voltage.
- *Patch clamp* – instead of a sharp electrode, this method involves using a micro-pipette to attach to a patch of a cell's membrane, which allows to either study the ionic channels within the patch itself, or displacing the patch to allow intracellular recording.

The research presented in this dissertation is focused on inter-areal neural dynamics, looking to assess the activity of local populations of neurons at a millisecond level temporal resolution. The non-invasive techniques allow to assess neural population activity, however they either lack the necessary temporal resolution (fMRI) or lack the necessary spatial resolution (EEG). Intracellular recording techniques allow to only focus on a single cell at a time. Consequently, the analyses performed in this dissertation relies on invasive *extracellular recordings*. These techniques involve placing the electrode into the brain tissue in the medium between intact neurons and recording the extracellular electric fields. These recordings result in a signal containing contributions from fast, millisecond-level precision spikes of nearby neurons, as well as slower synaptic currents of a larger local population of cells.

Filtering an extracellular recording with a high-pass filter ( $>500\text{Hz}$ ) and taking the absolute value of the result extracts the *entire spiking activity* (ESA), with neurons closest to the electrode showing up as high amplitude deflections in the signal [60]. ESA is a continuous signal representing the spiking activity of the local population of neurons. Consequently, taking a threshold of the high-pass filter of an extracellular recording allows to extract the spiking activity of a few neurons closest to the electrode, a discrete spike-times signal referred to as multi-unit activity (MUA). Further, analysing the waveform of each spike allows to categorize the spiking activity of individual cells.

Taking the low-frequency component of an extracellular recording provides the *local field potential* (LFP). LFP is commonly used as an indicator for the activity of a local population of neurons. However, the precise nature of LFP is not fully understood, including how far the local population of neurons extend, or the level of contribution of neurons distant from the electrode. The composition of LFP varies depending on the local network configuration, making it particularly tough to recreate it accurately in models [64]. For instance, the synaptic currents summed up in the LFP signal occur as a result of the input activity to the local neurons, weighted by their distance to the electrode, however, due to recurrent connectivity, the signal ends up as a complex mixture of input activity as well as the local output activity [38, 101].

## 2.4 NEURAL NETWORK ORGANIZATION

The number of neurons within a mature human brain is estimated to be 86 billion [105], with an average of roughly 7000 synaptic connections from each cell to other units [57], resulting in estimates of a  $10^{14}$  to  $10^{15}$  connections in total. This enormous number of neurons and their connections is simplified by the high levels of organization. Neighboring interconnected neurons form *local populations*, which combine to form distinct *functional areas* of the brain. *Systems of the brain* are then composed of multiple interconnected functional areas, with each system being responsible for a different function (e.g. the sensory systems: visual, auditory, somatosensory, etc).

Each system is composed of multiple cortical areas that form an organized functional pathway [156, 224, 242]. Although there are certainly neural projections between distant areas of the brain, a large portion of neural connections are confined between the serial, neighboring areas within a pathway. Neurons and connections participating in information flow from lower-order areas to high-order areas are referred to as ascending or *feedforward* or *bottom-up*. Connectivity from the higher-order areas down to lower-order areas is referred to as descending or *feedback* or *top-down*.

For the sensory systems, lower-order areas, starting with the peripheral sensory cells (e.g. in the retina of the eye, the cochlea of the inner ear, the surface of the skin), transfer stimuli information to higher-order areas which in turn project onto further higher-order areas up the functional pathway. Feedforward connectivity exhibits a strong convergent nature, having many neurons from lower-order areas project to a single neuron in a higher-order area. Thus, the information representation of the sensory stimuli within neural activity starts with simple features in the lower-order areas, growing in complexity as multiple projections from lower-order areas converge and get processed at each successive step up the functional pathway.

An important feature of the organization of most sensory systems is that the neurons are arranged *topographically* throughout successive stages of feedforward processing. Neighboring groups of cells in the retina project to neighboring groups of cells in the thalamus, which in turn projects to neighboring regions in the primary visual cortex and so on to higher-order secondary and tertiary visual areas. Thus, at each successive synaptic relay, neurons form an orderly *neural map* of information from the receptive surface. The spatial *receptive field* of a neuron (or a local population of neurons) refers to the area of the sensory space (or range of frequencies in the case of the auditory system) that the neuron is responsive to. Due to the strong converging nature of feedforward connectivity, the size of receptive fields increases at each successive step up the functional pathway [91].

Within each functional pathway, feedforward projections from one area to the next are accompanied by reciprocal feedback projections. These projections relay the information generated by higher-level cognitive functions, such as memory and attention, and are responsible for modulating the activity of neurons in the lower-order areas within the global context of sensory input, pre-existing knowledge, emotional state, stimulus expectation. One of the major processes implemented by such top-down connectivity is attention, selecting relevant information out of otherwise overwhelming amount of feedforward sensory input. Without such filtering, it would be difficult to handle the large amount of information. The mechanism behind selective processing of feedforward information is the primary subject of this dissertation, covered in more detail in a following section. A large portion of information processing – responsible for brain functions such as sensory perception, cognition, motor control and language – occurs within the area of the brain closest to the surface – the neocortex.

The *neocortex* is a major part of the brain, consisting of roughly 2mm of tissue closest to the surface. It contains a vast amount of the brain's functional areas and is responsible for many cognitive functions such as sensory perception, cognition, generation of motor commands, spatial reasoning and language. It has a very high density of neurons, roughly 20% excitatory and 80% inhibitory, referred to as *grey matter* (named so for what it looks like anatomically). The volume below the grey matter is primarily composed of the axon connections from the neurons above – *white matter*. Most of the neocortex has a uniform structure consisting of six distinctive layers, with each layer containing a consistent set of neuron types within a functional area. Neurons within a column of

neocortex have nearly identical receptive fields and are thought to form a local processing network. A *cortical column* is often considered to be a canonical microcircuit of the brain [56]. The neurons within each layer of a column exhibit repeating connectivity profiles – inter-laminar projections within the column itself, projections to and from other neighboring columns, and inter-areal connections to and from other areas of the brain. It has been found that feedforward intra-areal projections originate in the upper three layers (called *superficial* or *supragranular*) and terminating at layer IV (called the *granular* layer), whereas the lower layers (referred to as deep layers or *infragranular*) send feedback projections terminating at layers I and VI in lower-order areas [70]. Related to this, upper and lower layers of the neocortex have been found to exhibit distinct patterns of rhythmic neural activity.

The visual system is the largest and most intensively studied system, leading to many of the discoveries about cognitive function and the structure of neural network organization. It also happens to be the area utilized in the studies presented in this dissertation. The following section covers some of the intricacies of the visual system, revisiting and expanding the concepts presented above. The reader should remember that many of the findings and discoveries about the functional organization of the visual system correspond to similar structure within the other functional systems.

## 2.5 THE VISUAL SYSTEM

The following text on the visual system has been summarized from the following textbooks: chapters 25-29 of *Principles of Neural Science* by Kandel et al. [119] and chapter 12 of *Neuroscience* by Purves et al. [181].

Vision is the sense that humans and many other species depend on most. The visual system can be divided into a number of distinct sub-regions that can be arranged hierarchically, with simple visual features represented within neural activity within the lower-order areas, which then combine through convergent connectivity to form more complex feature representation in higher-order areas [224]. For many mammalian species, in particular for primates, early visual areas retain a topographical organization throughout the functional pathway, also referred to as *continuous retinotopic mapping*, having neighboring neurons receptive to a confined region of the visual field.

Prior to sensory information entering the cortex, the visual system starts at the retina of the eye, where specialized cells called *photoreceptors* activate in response to absorbing photons of light. Photoreceptors are divided into two types: *rods* are responsible for vision under dim illumination; *cones* are categorized by the range of wavelengths of light that they respond to, allowing for color vision. For primates, the density of cones is dramatically higher in the center of the retina, allowing for much higher acuity in the region, an effect that propagates up the visual system. Within the retina, the photoreceptors project onto bipolar cells, which in turn project to *retinal ganglion cells*. The ganglion cells receive input from multiple photoreceptors and perform simple feature extraction, characterized by their *center-surround* receptive fields – *on-center* cells activating in response to an annulus with a bright center surrounded by a ring of darkness, *off-center* cells activating in response to a dark center surrounded by a ring of brightness. The ganglion cells in the retina project to the *lateral geniculate nucleus* or *LGN* in the *thalamus* which acts as a relay point for visual information from the retina to the *primary visual cortex*, located at the posterior of the brain.

A prominent hypothesis in neuroscience argues that information processing in the cortex occurs through distinct pathways or "streams" of information processing – the *two stream hypothesis*. It's important to note that one should not over-emphasize the in-

dependence of the two streams as experimental evidence has shown there is interaction between them [151]. One stream, called the *dorsal pathway*, extends from the back of the brain through the top and then towards the front of the brain. This functional pathway, often referred to as the *where stream*, is involved in information processing concerning object location and movement. Cumulatively, the dorsal pathway performs visuo-motor integration and is responsible for spatial awareness and vision-related movement guidance. The other stream, referred to as the *ventral pathway*, extends from the back of the brain, towards the bottom left and right sides of the brain. This visual pathway, often referred to as the *what stream*, is involved in processing of shape and form of visual stimuli, cumulatively performing object recognition. Both streams are comprised from series of distinct areas. The majority of neural connections are between adjacent areas within a stream, referred to as *serial connectivity*, although there is also connectivity between the two pathways themselves, referred to as *parallel connectivity*. The research presented in this dissertation primarily involves the early visual areas in the ventral stream, in particular areas V1, V2 and V4, covered in detail below. However, the results and conclusions arising from these explorations are relevant across both streams as well as other functional systems.

The primary visual cortex, usually shorthand as area V1 and historically referred to as the striate cortex for looking "stripy", is the starting location for both streams. It combines the center-surround information content of the inputs from the LGN, resulting in having its neurons respond selectively to an array of simple features. V1 neurons selectively respond to brightness, orientation, spatial frequency, direction of motion and temporal frequency (e.g. in the case of a drifting grating). Typically, a neuron in V1 has a receptive field size ranging around 0.5-5 degrees, with smaller fields towards the center/fovea and larger fields with increasing eccentricity. Additionally, V1 begins integration of information from the two eyes, resulting in an *ocular dominance map*. All these features are organized into distinct maps of selectivity that span the region. These maps of functional organization coexist, overlaying each other and resulting in any particular cluster of neurons activating in response to a specific combination of stimulus features. Thus, a neuron in V1 is most excitable, or tuned to a *gabor* visual stimulus – a grating, localized in visual space with a specific orientation and spatial frequency. Neighboring neurons possess nearly identical response properties to a stimulus, forming a cortical column. A small segment of the visual cortex corresponding to a particular part of the visual field contains cortical columns that span all the possible feature values. One of the information processing operations of V1 is thought to be edge-detection – a simple filtering of the visual input to enhance edges and contours. Critically, V1 activity shows very little modulation by attention.

The primary visual cortex projects to the next step in the visual system – the secondary visual cortex also known as the prestriate cortex or just visual area V2. The receptive field sizes of a neurons in V2 are roughly 2 times greater than V1. This area retains the gabor-like information coding from V1 while integrating the ocular dominance information, allowing the neurons to assess the depth of the elements within the visual scene to perform some rudimentary segmentation of the visual input into foreground and background elements. From area V2, feedforward projections are split into the ventral and dorsal streams. V2 projects to area V3, which can be subdivided into dorsal and ventral subdivisions, each with distinct connections to areas within the corresponding stream. V2 also projects to area V4 in the ventral stream.

For the dorsal "where" stream, neurons within the dorsal subdivision of V3 send projections towards to the top of the brain, the parietal lobes, into area V5, often referred

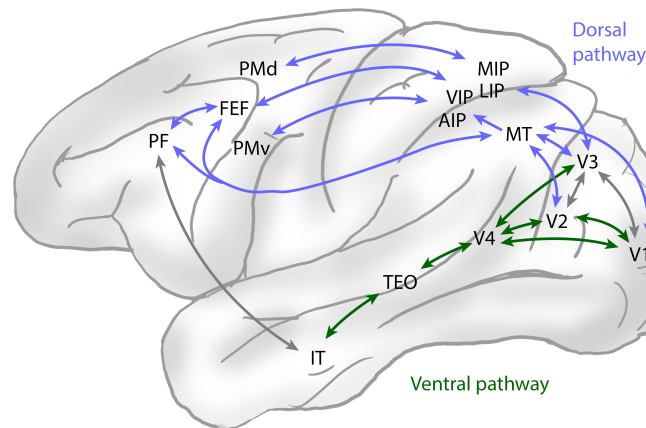


**Figure 2.3:** Visual system of macaque, ventral and dorsal pathways

to as area MT, middle temporal area. This area also receives direct input from area V1 and V2 and contains neurons that are highly selective for direction and speed of motion. Area MT connects with areas VIP (ventral intraparietal), and LIP (lateral intraparietal) – involved in visual attention and eye movements, area MIP (medial intraparietal) – representing space in terms of head/eye/nose-centered coordinates and used for visual control of reaching and pointing, and AIP (anterior intraparietal) – containing neurons responsive to shape size and orientation of objects and integrating visuo-motor information utilized for grasping and manipulating hand movements. These regions of the brain are connected with areas in the front of the brain, the frontal cortex, including areas FEF (frontal eye field), which plays an important role in visual attention and guiding eye movements, and areas PMd (dorsal premotor cortex) and PMv (ventral premotor cortex) – with neurons in these areas serving the role of preparation and guidance of movement in relation to the to objects in the immediate space surrounding the body. These areas are considered to be the final stage in the dorsal stream. They are connected to areas within the prefrontal cortex (PF), which carries out higher cognitive functions such as memory and decision making, sending information back down the dorsal pathway to enable goal-oriented information processing.

In the ventral "what" stream, area V4 receives most of its feedforward input from area V2 and some from V1. The receptive field size of a neurons in V4 are roughly 4 times greater than in V1. The neurons within this area retain tuning for orientation, color, brightness and spatial frequency present within the inputs from the lower-order areas. Some neurons are tuned for object features of intermediate complexity, like simple geometric shapes and texture. Critically, V4 is the first visual area in the ventral stream that has been found to exhibit strong attentional modulation. Area V4 sends strong converging projections to higher-order areas in the ventral stream, to area TEO in the temporal cortex and onwards to neurons in the inferotemporal cortex (IT). The receptive field of IT neurons tend to be large, with many neurons being responsive to nearly the whole visual field. Further, these neurons do not respond to simple features like spots or oriented bars, but rather exhibit consistent responses to complex forms. A subset of IT neurons is selective for facial images, with cells being selective for specific faces. Further, IT neurons are usually invariant against changes to stimulus size, contrast, color or position within the visual field. The IT cortex is considered to be the final stage in the ventral stream. It is connected to higher-order brain areas such the prefrontal cortex

and hippocampus, responsible for cognitive processes such as learning and memory formation, sending modulation signals that propagate back down the ventral pathway.

Cumulatively, for each stream, through convergent connectivity of the afferent projections, successive areas in the feedforward direction contain neurons with larger receptive fields and response properties that are tuned to increasingly complex features of the visual input. In the feedback direction, information from higher-order areas is relayed from higher-order to lower-order areas, modulating the activity within lower-order areas to select subsets of afferent signals, boosting behaviourally-relevant information at the cost of non-relevant inputs. This selective processing of information is a fundamental cognitive process – *selective attention*.

## 2.6 SELECTIVE ATTENTION

Selective information processing is one of the critical characteristics of the mammalian brain, allowing to quickly adapt information processing in response to the complex and rapidly changing sensory input and behavioural demands. While this flexibility could, in principle, be achieved through direct anatomic changes in synaptic connectivity, such modifications are on a considerably slower time scale than required for many cognitive processes. Thus, some sort of a functional mechanism is necessary in order to adapt the effective connectivity through the brain. In our investigations, attention serves as the characteristic cognitive function that employs flexible information processing. Broadly speaking, attention is the cognitive function responsible for allocating neural resources to process a subset of external or internal information at the expense of resources that might have been allocated to other concurrent information.

### 2.6.1 Key concepts and psychology of attention

A popular example of selective attention is referred to as the *cocktail party effect*, where a listener can selectively attend to one voice, tuning out other simultaneously ongoing conversations and sounds around them. Similar effects are found throughout the other sensory modalities. One of the earliest theories of selective attention was proposed by 1950s by psychologist Colin Cherry [49] and later complemented by Donald Broadbent [31] in the 1950s, stating that the capacity to process information is limited and unattended information is filtered out from the processing stream early on in the sensory system – the *early-selection model*. These ideas were expanded further by Anne Triesman, noting that at least some information from the unattended source is getting processed, for instance when hearing your name grabs your attention in an otherwise unattended conversation [219]. This finding has led to the proposal of the *late-selection model*, where an attentional mechanism is only employed after some level of higher-level processing is completed, determining what input information enters consciousness. Psychological theories of attention were revisited further, incorporating the concept of *perpetual load* [130]. Perceptual load is the idea that there's a limited capacity of information processing available to be allocated across the set of input information, thus the complexity of a task and the brevity of presentation strongly influences the amount of information routing of attended and non-attended components. If a task is simple, the perceptual load is low, allowing for more processing available for non-attended inputs and allowing them to reach higher processing levels where late-selection mechanisms operate. If

a task is complicated or the amount of time to process and input is sufficiently small, non-attended components do not get processed.

Many studies on attention involve a subject consciously directing their attention to a particular aspect in the sensory environment. This type of voluntary attention is called *endogenous*, with attention being directed via a top-down source. Endogenous attention can be further categorized as *overt* – involving orientation of head and eyes to a stimulus, improving information processing of the desired stimuli by facing the source of the sound or placing a visual stimulus in the center of the fovea; or *covert* – where attention is directed without moving the head or eyes. Many studies focused on overt attention involve analyzing patterns of gaze throughout a scene [81, 120], whereas studies focused on covert attention typically involve holding fixation on a particular point while presenting cued (to be attended) or uncued (non-attended) stimuli at particular locations of the visual field [47, 65]. In contrast to conscious top-down processes, attentional shifts can also occur involuntary, driven by bottom-up stimulus information. This sort of attention is referred to as *exogenous*. Here, attention is directed towards a subset of the sensory input with high salience – the degree to which a portion of the sensory input is different from its surroundings. Cortical areas such as LIP and FEF have been found to provide a sort of an information-allocation priority map, referred to as a *salience map*, based on local stimulus features within a scene [69, 126, 216].

A noteworthy series of psychological studies examining the effect of covert attention on perception were performed by von Helmholtz in the late 19th century [238, 239]. In one of the studies, subjects were asked to fixate on a central fixation point on a board in a dark room which had random letters written on at various eccentricities away from the fixation point, unrecognizable until the board was briefly lit up. The experiment showed that participants were only able to discriminate the letters located within restricted regions of the visual field which the subjects covertly attended prior to switching on the light. This illustrates the link between attention and selective information processing during *visual spatial attention*. Further studies showed that attention results in an increased sensitivity to stimulus changes within the attended region, indicated by the subjects' behavioural performance in an experiment, e.g. by the accuracy and reaction times of their responses [67, 179]. Attention can also be directed towards a particular named feature, *feature-based attention* [155], such as color or shape of the presented stimulus, or even a combination of features present within complex objects, *object-based attention* [63]. In these cases, rather than increasing information processing within a region of the visual field, attention is thought to increase the information processing capabilities specific to a desired feature or combination of features across the entire visual field.

### 2.6.2 *The neuroscience of attention*

Psychological studies have allowed to examine attentional processes in terms of subjects' behaviour, drawing conclusions based on subjects' performance, such as accuracy and reaction times when performing a carefully designed task. Neuroscience studies attempt to find neural correlates and work out the neural mechanisms underlying the resulting behavioural effects. A variety of effects have been reported on neural activity of single neurons or local population of neurons when comparing the activity when processing attended versus non-attended stimuli, at various stages of the visual pathway.

Within single units, attention tends to increase the mean firing rate, improving the signal to noise ratio of the encoded information [142, 165, 190, 220]. However, *Mitchell et al. 2009* [162] found that the attentional effect on firing rates in V1 is rather small,

accounting for just a fraction, 9.5%, of the differences in performance between the attended conditions. In the same study, the researchers analyzed the paired correlations of neural spiking activity, finding that task-irrelevant activity fluctuations were significantly reduced when processing attended stimuli. Crucially, multiple studies have also found significant effects of attention on the rhythmic activity of the neural populations – covered in more detail in the next section.

The above effects were acquired from experiments with only one stimulus, attended or non-attended, within the receptive field of a neuron or population of neurons. In order to study attention dependent routing of information, it is necessary to assess the activity of neurons that contain both attended and non-attended stimuli within their receptive field. A study by *Moran and Desimone 1985* [163] performed precisely such an experiment by recording neural spiking activity in areas V4 and IT. Within the receptive field of the recorded neurons, the researcher placed either an effective stimulus (eliciting a high-firing rate), or an ineffective stimulus (eliciting a low-firing rate), or both simultaneously, with the task to attend to one of the stimuli. By comparing the firing rates between the conditions, the researchers found that when two stimuli were present within the receptive field, neurons respond as if just the attended stimulus was present. Simultaneously, the researchers found that V1 neurons, containing one of the two stimuli and responsible for sending stimulus information to V4 and IT, did not exhibit attention-dependent changes in their firing rates.

These findings from the above experiment have been replicated for other areas in the visual pathway [99, 131, 142, 185, 186, 220], showing that attending to a stimulus results in having its representation enhanced in downstream populations while suppressing the representation of a non-attended stimulus. Crucially, this effect cannot be explained solely by the small effects of attention on the firing rate within lower-area sender neurons, e.g. V1 neurons that project to V4. This poses the central question explored by the research in this dissertation: *where* and *how* does attention intervene in the neural circuitry and neural dynamics between sending and receiving neurons.

There are multiple possible points where attention can intervene [99]. In early intervention point, attention could modulate the output of the sender populations resulting in a stronger input signal to V4 from the V1 population with the attended stimulus in its receptive field – input gain modulation. In the intermediate intervention point, attention could modulate the interaction between sending and receiving populations with the attended signal from V1 getting enhanced en route to V4 – afferent signal gating. In the late intervention point, attention could modulate the response of the receiver population at its output stage – output gain modulation. In the next section, we finally introduce rhythmic neural activity.

## 2.7 RHYTHMIC NEURAL ACTIVITY

Rhythmic neural activity, also referred to as neural oscillations, were observed as soon as the first methods of recording of a brain's electrical activity were developed over a century ago, first in rabbits and dogs in 1875 by Adolf Beck [53], and then in human brains with the invention of the *Elektrenkephalogramm* (EEG) by Hans Berger in 1924 [118]. Since then, oscillatory neural activity has been found to be widespread throughout biological neural networks, observed at many levels of neural organization, and linked to many cognitive functions [39, 77]. When an area in the visual cortex of a subject is activated by a stimulus within its receptive field, neurons tend to engage in rhythmic synchronization in the gamma-band (30-90Hz) [76, 80, 96].

Oscillatory neural activity in a group of neurons arises as the result of synchronized firing of the cells in a temporally-rhythmic manner, resulting in alternating periods of low and high levels of neural activity. Rhythmic neural activity can be characterized by its frequency, amplitude and phase, occurring at various frequency bands, which got their names from the order in which they were observed – *alpha* (8-12Hz), *beta* (13-30Hz), *gamma* (>30Hz), and afterwards *delta* (1-4Hz) and *theta* (4-8Hz).

### 2.7.1 Local circuit oscillation mechanisms

There are two network setup candidates that have been found responsible for generation of self-sustained gamma neural rhythms within local populations of neurons [41]. Both circuits rely on inhibitory interneurons (I) that project locally within a cluster of neurons, acting as a rhythmic pace-maker within the local population.

In one setup, a sub-population of the inhibitory cells exhibit strong recurrent connectivity to itself – *I-I connectivity* [33, 121, 240, 246]. In this setup, the inhibitory cells are sufficiently excited by an external input to begin firing, which, after a delay, causes the cells to get suppressed by their own recurrent inhibitory input, which, in turn, removes the recurrent inhibition allowing the population to start firing again. The inhibitory cells also project to the local excitatory pyramidal neurons, enforcing their rhythm across the local population.

In the second network setup, the sub-populations of excitatory and inhibitory cells send and receive reciprocal projections – *E-I connectivity* [27, 33, 68, 247]. In this case, spikes from the excitatory population cause the inhibitory cells to start firing, which consequently suppress the excitatory neurons, which then cause the inhibitory cells themselves to stop firing without their excitatory drive, allowing the excitatory neurons to start firing again and repeating the cycle.

Both circuits are proposed to be driving attentional gamma oscillations [217]. In both circuits, the delay between a neuron population firing off a burst of spikes and the subsequent effect of these spikes on the receiving neurons sets a range of frequencies of oscillations that can be produced. Raising (or lowering) the level of excitatory drive to either network raises (or lowers) the frequency at which it oscillates within a relatively narrow range of frequencies. In this way, a network is said to be *resonant* to the specific frequency-band, generating or enhancing rhythmic activity when its neurons are

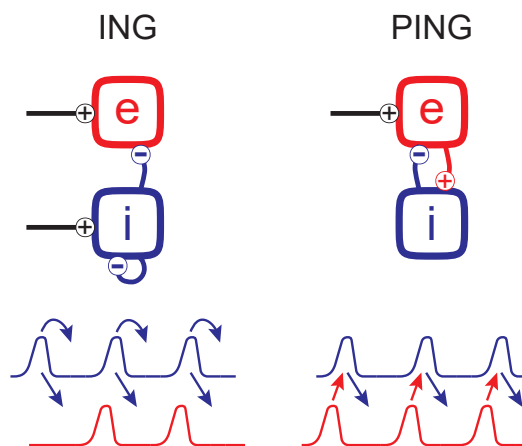


Figure 2.4: ING and PING oscillation mechanisms

driven from an outside source. In the case of gamma oscillations, the first mechanism is often referred to as ING (interneuron gamma) and the second is referred to as PING (pyramidal-interneuron gamma) [13, 26, 244].

### 2.7.2 *Binding by synchrony*

One of the major functions proposed to be enacted by neural rhythms is that of "solving" the *binding problem*. The binding problem asks the question of how features of individual objects, sensory (e.g. seeing an object) or abstract (e.g. a thought), are grouped together or segregated into discrete concepts. Within the constructive nature of the feedforward visual system, how do all the features of an object (e.g. its color and its shape coded by separate neurons) get combined to cumulatively form the perception of that object as its own individual thing?

The theory, called *binding-by-synchrony* (BBS) proposed that neurons coding for features of some object are "bound" together by firing synchronously in the gamma rhythm whereas neurons that do not code for features of an individual object do not synchronize [160, 200, 204]. In essence, rhythmic activity would allow to exploit the time domain to bind stimulus features together, allowing to flexibly group widely distributed neurons into coordinated assemblies. A number of studies have shown support for this theory, showing neurons processing the same stimulus within an area do exhibit gamma-rhythmic synchronizaton in their responses [66, 124]. However, other investigations found that such gamma-rhythmic synchronization is not consistent, present for certain perceptually-bound stimuli but decreased or absent for others [90, 116, 183, 215]. The debate whether gamma-band synchronization plays a fundamental functional role [78, 123] or is merely an epiphenomenon arising from neural circuit organization, accompanying cognition without a functional role [157, 200] remains a subject of major debate today.

Eventually, later experiments indicated that synchronized oscillatory activity is not only stimulus driven, e.g. feedforward, but also depends on feedback processes such as anticipation of an attention-demanding task [106, 167, 189]. Direct links to attention-dependent routing were shown by *Fries et al. 2001* [76], finding that spikes in V4 occur during specific phases of V4's gamma-band LFP activity when V4 neurons encode an attended stimulus but do not align to specific phases when the neurons encode a non-attended stimulus. Similar findings have been replicated for other visual areas [23, 34, 97, 213]. Cumulatively, these experiments led to the development of a new theory, linking synchronization to selective routing of information, referred to as *routing-by-synchrony* (RBS) or *communication-through-coherence* (CTC).

### 2.7.3 *Routing by synchrony*

The RBS mechanism, formalized in 2005 [77] and then refined in 2015 [79], proposes that a sending and receiving populations of neurons establish coherence between their gamma rhythms, allowing to control the efficacy of information transfer between them. In detail, gamma synchronization has been found to affect information processing at all stages of interaction between sending and receiving populations:

### 2.7.3.1 *Sender population: synchronization enhances impact of output activity*

In the pre-synaptic/sending population, gamma-rhythmic synchronization of neural activity focuses the spiking output into periodic bursts, increasing their post-synaptic impact by the nature of delivering a higher amount of spikes simultaneously, allowing for enhanced spike coincidence detection in the post-synaptic population. A study directly demonstrating this effect was performed by *Zandvakili and Kohn 2015* [254], showing that spiking activity in post-synaptic V2 was preceded by elevated levels of gamma-rhythmic coordination of spiking activity in pre-synaptic V1.

### 2.7.3.2 *Receiver population: synchronization modulates input gain*

In the post-synaptic/receiver population, gamma-rhythmic activity results in a periodic modulation of excitability, with a period of when a population is inhibited and not prone to firing followed by a period of when the population is excitable and prone to firing. In support, researchers used optogenetic stimulation to entrain neurons in the somatosensory cortex of rats, showing that both neuronal [46] and behavioural [201] responses were enhanced in accordance with the enforced rhythm. *Ni et al 2016* [172] replicated the effect for the visual cortex, utilizing optogenetic entrainment of V4 during a selective-attention task. In chapter 3, rather than linking rhythmic activity to behaviour, we go straight for the source – linking signal information content encoded within neural activity with gamma dynamics.

### 2.7.3.3 *Coherence between sending and receiving neurons*

When the two populations establish coherence at an appropriate, favorable phase, the bursts of spikes from the sending population arrive to the receiver population when it is most excitable, enhancing information transfer. Theoretically, the two populations can also establish coherence in an unfavorable phase, with the bursts of spikes from the sender population arriving to the receiver when its least excitable. Thus, coherence between sending and receiving neurons can be used for selective information routing. In support, two independent experiments, by *Grothe et al. 2012* [98] and by *Bosman et al. 2012* [29], found that a V1 population processing an attended stimulus establishes strong coherence in the gamma-band with the receiving neurons in V4. Meanwhile, a V1 population processing a non-attended stimulus exhibits similar levels of gamma activity, but does not establish coherence with V4.

Existing research has not directly analyzed the precise phase relationship between the sending and receiving populations. Moreso, there has not been a direct investigation into how the different levels of coherence for attended and non-attended conditions would affect information transfer between the two populations. In chapter 5, we investigate these dynamics within a limited V1 recordings dataset.

### 2.7.3.4 *Laminar specificity*

In the original formulation of RBS in 2005 [77], Fries proposed that coherence in the gamma-band occurs at zero-phase lag, allowing for bidirectional transfer of information, in the feedforward and feedback directions, mirroring the previously established findings for the synchronized neural assemblies in the binding-by-synchrony theory. Even though bidirectional transfer of information according to RBS is possible in theory, recent studies revealed that gamma-rhythmic influence occurs specifically in the feedforward direction, corresponding to the laminar-specific anatomic connectivity, originating

in the superficial layers of the sending populations arriving to the input layer 4 in the receiving population [15, 34, 145, 168, 225].

Feedback influences were found to occur in a different frequency band, beta, originating in the deep layers of the cortex. Consequently, in 2015, Fries updated the formulation of the RBS mechanism, specifying the laminar and feed-forward specificity of gamma-rhythmic coherence. The effect of stimulus information coding in dependence of the laminar-specific rhythms has not been explored. Consequently, this laminar distinction proved to be critical in the data-analyses presented in chapter 3, requiring to split the data set into surface and deep recording sites. This allowed us to perform a pilot study examining how stimulus information is coded within the deep, feedback-specific layers of V4, presented in chapter 4.

#### 2.7.4 *Neural rhythms and stimulation*

Previous studies have been successful at utilizing optogenetic microstimulation, allowing researchers to form strong causal conclusions about the functional significance of gamma synchrony [46, 172, 201]. Specifically, the researchers employed periodic pulses of optogenetic stimulation in order to completely entrain a target population of neurons, enforcing an artificial rhythm onto a local population. However, similar stimulation paradigms have not been used in order to establish coherence between sending and receiving neurons.

Is it possible to control the phase of rhythmic activity without continuous entrainment perturbations to the system? By exploiting the nature of oscillator dynamics, theoretical studies have shown that it is possible to deliver a precise pulse of the required amplitude in order to achieve a desired phase-shift in the activity or to potentially completely reset the phase of an oscillation [2, 28, 42]. This concept is captured by *phase-response curves*, where the delivery of a single stimulation pulse at a specific phase of the activity results in a consistent effect on the ongoing dynamics, e.g. shifting the gamma phase.

Can we manipulate neuronal synchronization and coherence while leaving other aspects of neural activity unchanged to show effects on neural information transfer? Delivering minimal amounts of stimulation in order to control rhythmic activity, while simultaneously allowing natural oscillatory dynamics to occur would be extremely beneficial. Such a paradigm would allow to form concrete indisputable conclusions about the role of natural rhythmic activity. Existing modeling studies have relied on extremely stable oscillatory dynamics, without much consideration for the level of noise and instability present within biological networks, which avoids numerous practical issues that would occur *in vivo* [170].

In chapter 6, we construct and study a biophysically plausible model, exhibiting information routing by synchronization. The model allows us to simulate the effect of phase-specific perturbations within a network of populations, utilizing a closed-loop paradigm in order to causally control information routing within the system. Further, we are able to address numerous practical issues, such as the development of methods in order to assess real-time phase in order to deliver precise pulses as well as analyzing the efficacy of the approach in relation to the amount of noise within the network.

Part II

ANIMAL DATA ANALYSIS



Selective visual attention allows the brain to focus on behaviorally relevant information while ignoring irrelevant signals. As a possible mechanism, routing-by-synchronization was proposed: neural populations receiving attended signals align their gamma-rhythmic activity to that of the sending populations, such that incoming spikes arrive at excitability peaks of receiving populations, enhancing signal transfer. Conversely, non-attended signals arrive unaligned to the receiver's oscillation, reducing signal transfer. Therefore, visual signals should be transferred through gamma-rhythmic bursts of information, resulting in a modulation of the stimulus content within the receiving population's activity by its gamma phase and amplitude. To test this prediction, we quantified gamma phase-dependent stimulus content within neural activity from area V4 of two male macaques performing a visual attention task. For the attended stimulus, we find highest stimulus information content near excitability peaks, an effect that increases with oscillation amplitude, establishing a functional link between selective processing and gamma activity.

### 3.1 INTRODUCTION

Visual information processing is computationally demanding, requiring the brain to handle a continuous, high-dimensional stream of sensory input signals. Selective attention helps to reduce this computational complexity by focusing on signals which are behaviorally relevant at the expense of other, irrelevant signals [130]. Selective processing is already observed at the single neuron level: when presented with two stimuli inside their receptive fields (RFs) of which one is attended, V4 neurons respond primarily as if only this stimulus was present [99, 163, 185]. However, there is only a small attention-dependent modulation of firing rates of the V1/V2 populations providing the input signals from the two visual stimuli to V4 [142, 149, 153, 163, 165, 194]. Hence, selective responses in downstream areas cannot result exclusively from upstream rate modulations, suggesting that selective attention relies on a different mechanism in order to dynamically change effective connectivity depending on task demands.

One influential idea proposes inter-areal synchronization of oscillatory neural activity in the gamma-band frequency (40Hz-100Hz) in order to enact dynamic modulation of effective connectivity between presynaptic and postsynaptic populations [77, 79, 122, 123]. In this scheme, gamma-rhythmic activity serves multiple functions. For presynaptic populations, it coordinates their spiking output into periodic bursts, increasing their postsynaptic impact [10, 76, 209, 213, 254]. These periodic bursts of spikes focus stimulus information into gamma-rhythmic packages [249]. For postsynaptic populations, gamma-rhythmic activity enacts modulation of gain of its inputs, with alternating windows of high and low excitability [9, 41, 172, 195, 232]. When both sending and receiving populations exhibit gamma-rhythmic activity, they can establish coherent states with coupled phases (Fig. 3.1A). In a favorable state for information routing, the gamma-rhythmic bursts of spikes from the presynaptic population arrive at the receiving population during windows of high excitability, resulting in enhanced information transfer. In an unfavorable phase relationship, the spikes arrive predominantly during windows of

inhibition in the receiver population, resulting in suppressed information transfer. Thus, effective connectivity between presynaptic and postsynaptic populations can be modulated by establishing an appropriate phase relationship between their gamma rhythms. This mechanism has been referred to as communication-through-coherence (CTC) [77, 79], or as routing-by-synchrony (RBS) [98, 99, 122, 123, 176]. In support, research has shown that V4 populations establish stronger phase coherence with the presynaptic populations processing attended stimuli as opposed to those processing non-attended stimuli [29, 98].

Cumulatively, RBS posits that stimulus information arrives to V4 from lower visual areas in the form of gamma-rhythmic information packages, where the phase relationship between the sending and receiving populations determines whether information get passed on or suppressed (Fig. 3.1B). Additionally, the gamma oscillation amplitude is not constant [30, 152, 207], so one also expects selective routing to be enhanced (or diminished) during periods of higher (or lower) amplitude gamma activity.

Here, we directly investigate whether selective information transfer of extended, time varying signals in V4 complies with the RBS mechanism. For this purpose, we quantify attended and non-attended stimulus information content (SIC) within V4's neural activity at different phases and amplitudes of successive gamma-oscillation cycles. If gamma synchronization and selective information routing were causally linked to each other, we expect SIC to be modulated by phase with its maximum corresponding to V4's excitability peaks (Fig. 3.1B). This effect should be consistently higher for the attended signal compared to the non-attended, increasing (or decreasing) during periods of high (or low) gamma activity.

## 3.2 MATERIALS AND METHODS

### 3.2.1 *Experimental model and subject details*

All procedures and animal care were in accordance with the regulation for the welfare of experimental animals issued by the federal government of Germany and were approved by the local authorities. Data from two adult male rhesus monkeys (*Macaca mulatta*) were used for this study. Parts of the data have been used in a previous publication [99].

### 3.2.2 *Surgical procedures and behavioral task*

Details about the surgical preparation, behavioral task and recording details have been described in detail in past publications [98, 99]. In short, animals were implanted under aseptic conditions with a post to fix the head and a recording chamber placed over area V4. Before chamber implantation, the monkeys had been trained on a demanding shape-tracking task (Fig. 3.2A). Neural signals were measured from area V4 with 1–3 epoxy-insulated tungsten microelectrodes (125  $\mu\text{m}$  diameter; 1–3  $\text{M}\Omega$  at 1 kHz; Frederic Haer). Reference and ground electrodes for Monkey F were platinum-iridium wires below the skull at frontal and lateral sites. The reference for Monkey B was a platinum-iridium wire placed posteriorly below the skull, and the ground was a titanium pin at the posterior end of the skull.

The task (Fig. 3.2A) required fixation throughout the trial within a fixation window (diameter 1–1.5 degrees of visual angle) around a fixation point in the middle of the screen. Eye position was monitored at 100 Hz using a video-based eye tracking system

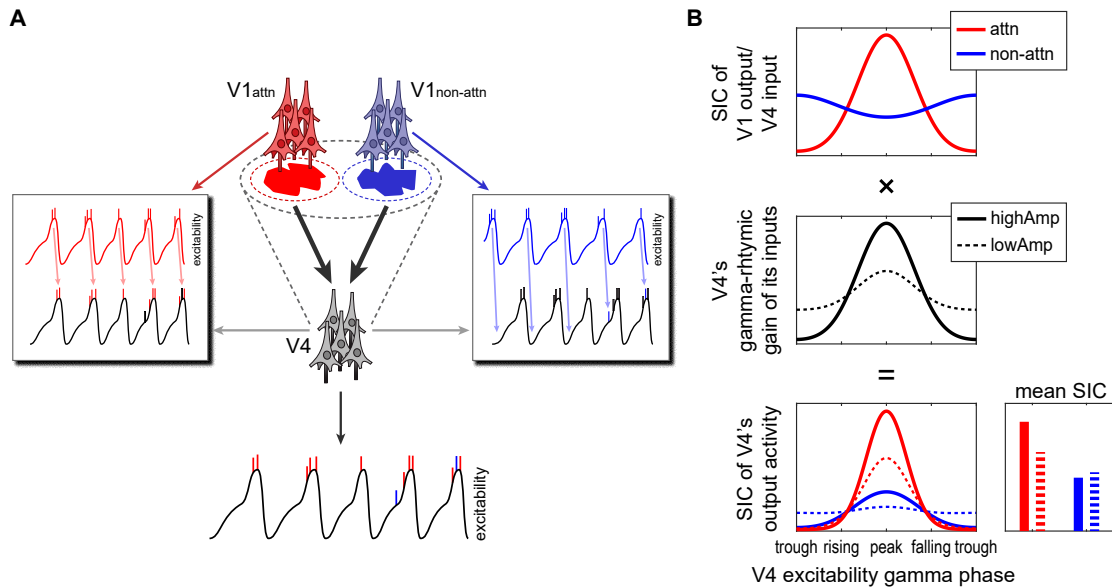


**Figure 3.1: Routing by synchrony mechanism predicts modulation of stimulus information content within V4's gamma-rhythmic neural activity, depending on V4's gamma phase and amplitude.**

**A.** Schematic outline of the routing by synchrony (RBS) mechanism, which allows downstream neurons to process stimulus information mediated by selected subsets of afferent inputs while suppressing the information provided by other inputs. Two stimuli (red and blue shapes) compete for being processed by a downstream V4 population with a large receptive field (RF) containing both stimuli indicated by the gray dashed oval. Each visual stimulus is contained within RFs of separate V1 populations (red and blue dashed ovals) evoking spiking activity within their corresponding V1 population (red and blue vertical bars in the insets). The V1 populations exhibit gamma-rhythmic activity, causing their spikes to occur in bursts. These bursts of spikes act as input to V4, which exhibits its own gamma-rhythmic activity (gray oscillatory lines in the insets). The rhythmic activity of the V1 population corresponding to the attended stimulus is synchronized with V4's gamma rhythm in a favorable phase relationship, such that its spikes arrive at V4 when it is most excitable (left inset, red arrows). This effectively evokes spiking activity in V4, resulting in a reliable transfer of the attended stimuli's information. Conversely, the rhythmic activity of the V1 population with the non-attended stimulus in its RF exhibits substantially less phase-locking with V4's gamma rhythm [29, 98], resulting in many cycles where the bursts of spikes arrive at V4 when it is least excitable, failing to evoke further spikes (right inset, light blue arrows). In consequence, the transfer of the non-attended stimulus signal is suppressed.

**B.** Scheme showcasing how the information contained within attended and non-attended stimuli (stimulus information content, SIC), should be modulated depending on V4's gamma phase and amplitude in accordance with RBS. Assuming that the upstream cortical population processing the attended stimulus establishes a favorable phase relationship with V4 as shown in (A, left inset), the highest amount of attended SIC should arrive during V4's excitability peak (red line in top plot). Assuming that for the non-attended stimulus, the corresponding upstream population establishes substantially less phase-locking with V4, and in a predominantly anti-phasic relationship, we expect SIC modulation to be much lower, with a slightly higher amount of non-attended SIC arriving at V4's excitability trough than at its peak (blue line in top plot). The middle plot shows V4's gamma-rhythmic gain (solid black line for high amplitude gamma activity and dashed black line for low amplitude). Modulating the phase-specific SIC inputs to V4 (top plot) by V4's gain (middle plot) provides a prediction of how attended and non-attended SIC should depend on V4's excitability gamma phase and amplitude within its output activity (bottom plot). The corresponding bar plot (bottom right) displays the average SIC within V4's output activity independent of phase, demonstrating how attended and non-attended SIC should change during V4's high amplitude versus low amplitude gamma activity (solid colored bars for high amplitude condition and dashed colored bars for low amplitude condition).

(monkey B: custom made, monkey F: IScan Inc). If the animal moved its eyes away from the fixation point, the trial was immediately terminated. Microsaccades within the fixation window were extracted by computing eye movement speed and extracting windows where it exceeded 3 standard deviations of its mean.

After a baseline period, the monkeys had to covertly attend to one of two statically presented, closely spaced stimuli (shapes) that was cued (static/cue period). Then both shapes started morphing into other shapes. The monkeys were trained to respond by releasing a lever when the cued initial shape reappeared at a pseudo-randomly selected position in the shape sequence, after two to five morph cycles. The animals had to ignore reappearance of the initial shape in the distracter sequence. The shapes were placed at equal eccentricity. Stimuli were presented with a refresh rate of 100 Hz on a 22 inch CRT monitor containing 1152 x 864 pixels (monkey B) or 1024 x 768 pixels (monkey F), which was placed at a distance of 92 cm (monkey B) or 87 cm (monkey F) in front of the animal.

In order to be able to track the information content of the stimuli within the neural activity, we used filled shapes and tagged the neural activity they evoke with imposed broadband luminance fluctuations ('flicker') on the stimuli: we changed the luminance of the shapes by choosing a random, integer gray pixel value with each frame update of the display. For monkey F, the values were drawn from an interval [128, 172], and for monkey B, from the full range [0, 255], corresponding to luminance fluctuations in a range of 6.9-12.5 and 0.02-38.0  $\text{Cd}/\text{m}^2$ , respectively. Both shape streams had their own independent flicker time series of luminance values. Note that the flickering of the stimuli was not relevant to perform the task. A few trials were included in which only one stimulus was presented for offline controlling of response strength to individual stimuli.

### 3.2.3 *Recording*

The electrodes' signals were amplified by a factor of 1000 (Monkey B; USB-ME-256 System, Multi-Channel Systems GmbH) or 5000 (Monkey F; MPA32I and PGA 64, 1-5000 Hz, Multi-Channel Systems GmbH) and digitized at 25 kHz. For positioning stimuli, receptive fields were mapped manually while the monkey was fixating centrally, followed by an automated mapping procedure consisting of rapid presentations of circular dots. Stimuli were placed at equal eccentricity in the RF such that they induced similarly strong gamma-rhythmic activity [99]. This requirement was successfully fulfilled in 16 recording sessions, resulting in 35 recording sites in total (Monkey F: 23 sites, Monkey B: 12 sites).

### 3.2.4 *Data preprocessing and site selection*

From the recorded raw data, we extracted the local field potential (LFP) as a proxy reflecting average neural activity around the recording site, and the entire spiking activity (ESA) as a measure of local spiking activity [60]. All filters used in the process were realized as forward-backward FIR-filters to preserve the phase of the original signal, using the function 'eegfilt' from EEGLab [54] with standard parameters for the cutoffs:

- For obtaining the LFP signal, we extracted the low frequency component from the 25 kHz raw neural recordings by applying a bandpass FIR filter with band stops at 1 and 200 Hz.

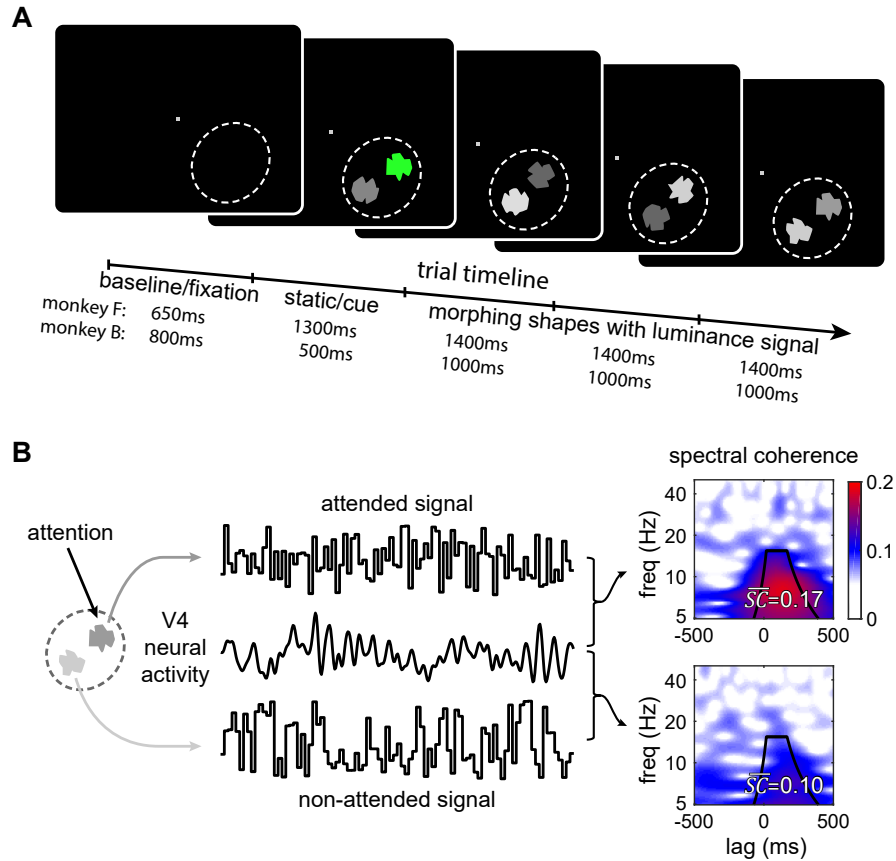


**Figure 3.2: Behavioral task and quantification of stimulus information content.**

**A.** Stimulus sequence. After the monkey presses a lever, the trial starts with the appearance of a fixation spot (baseline period). Shortly afterwards, two stimuli in the form of static shapes are presented within the RF of the V4 recording site (dashed ellipse). One of the shapes is cued to be memorized and attended with green shading while the other shape has to be ignored (static period). Then the cued shape reverts to gray and both stimuli begin to morph into different shapes. After a number of morph cycles, the initially cued shape reappears in the attended location. If the animal releases the bar within a short time window around the reappearance of the cued shape, a reward is delivered.

**B.** Throughout the morphing period, each shapes' luminance was modulated in time by a random white-noise signal. These luminance fluctuations were irrelevant to the task but served as independent tags for signals originating from the stimulus to be attended, and from the stimulus to be ignored. We evaluated spectral coherence between the recorded neural signals and each input signal to quantify stimulus information content (SIC) in V4 activity. By pooling across relevant lag and frequency bins from the spectral coherence (indicated by the black lines) a single value ( $\overline{SC}$ ) was acquired for each signal.

- For obtaining the ESA signal, the raw data was first bandpass-filtered from 400 Hz to 2500 Hz. We then took the absolute value of the result, and subsequently applied a second bandpass FIR filter with band stops at 1 and 200 Hz to simplify phase dissociation (see detailed explanation below).

Finally, both signals were down-sampled to 1000 Hz and z-score normalized, yielding  $y_{LFP}$  and  $y_{ESA}$  used in our data analysis explained in the next section. For ensuring that the recording sites were within the superficial layers of V4 we employed an additional selection criterium: The shape of the visual evoked potential (VEP) caused by the stimulus onset shows the characteristic time course expected for the superficial layers, which starts with a negative deflection as opposed to the initial positive deflection observed in the deeper layers [92, 168]. We computed the VEP for each recorded site by averaging its LFP over trials. These selection criteria left 12 recording sites for monkey F and 10 for Monkey B.

The experimental setup involved having two stimuli within the V4's RF; each location was cued to be attended for half of the recorded trials in each session. We decided to split the trials of each recording site by the attended location, providing us with 24 data sets for monkey F and 20 data sets for monkey B. This was possible because  $\overline{SC}$  values from trial sets split by attended location were as statistically independent as  $\overline{SC}$  values from different recording sites, suggested by the fact that the distributions of the differences between the split sets and the full sets were not significantly different (Wilcoxon signed rank test).

### 3.2.5 Data analysis

Data analysis consisted of several processing steps applied to the LFP and ESA signals in sequence (Fig. 3.3). Briefly, first gamma phase and amplitude were extracted from the LFP, and gamma phase converted to excitability phase by assessing the spike-field coupling from ESA and LFP activity. Then, gamma excitability phase was used to isolate the signal values occurring at specific phases to form a phase-specific signal. Periods of high (low) gamma amplitude were selected to form an amplitude-specific signal. In the final step of the analysis, stimulus information content in the neural signals was assessed by computing the spectral coherence between the luminance flicker and the dissociated LFP or ESA signals. In the following sections, each of those steps are explained in detail.

#### 3.2.5.1 Extraction of gamma phase and amplitude

By applying a wavelet transform with Morlet kernels, we first computed the average power spectrum of the LFP signal  $y_{LFP}$  during the period in which the stimuli were morphing until 200 ms before a correct response, and normalized it by the average power spectrum observed before stimulus onset in the baseline period (separately for each recorded site). The spectra revealed clear peaks in the gamma frequency range, of which we extracted a lower and upper frequency limit by taking location at half of the highest point around the peak (approximately 40 to 100 Hz for monkey F recordings, and 50 to 110 Hz for monkey B). Subsequently, gamma activity was obtained by applying a forward-backward FIR band-pass filter to the LFP with cutoff frequencies determined by the lower/upper frequency limits. By applying the Hilbert transform to the result, we obtained LFP's gamma phase  $\Phi_{LFP}$  and amplitude  $A_{LFP}$ .

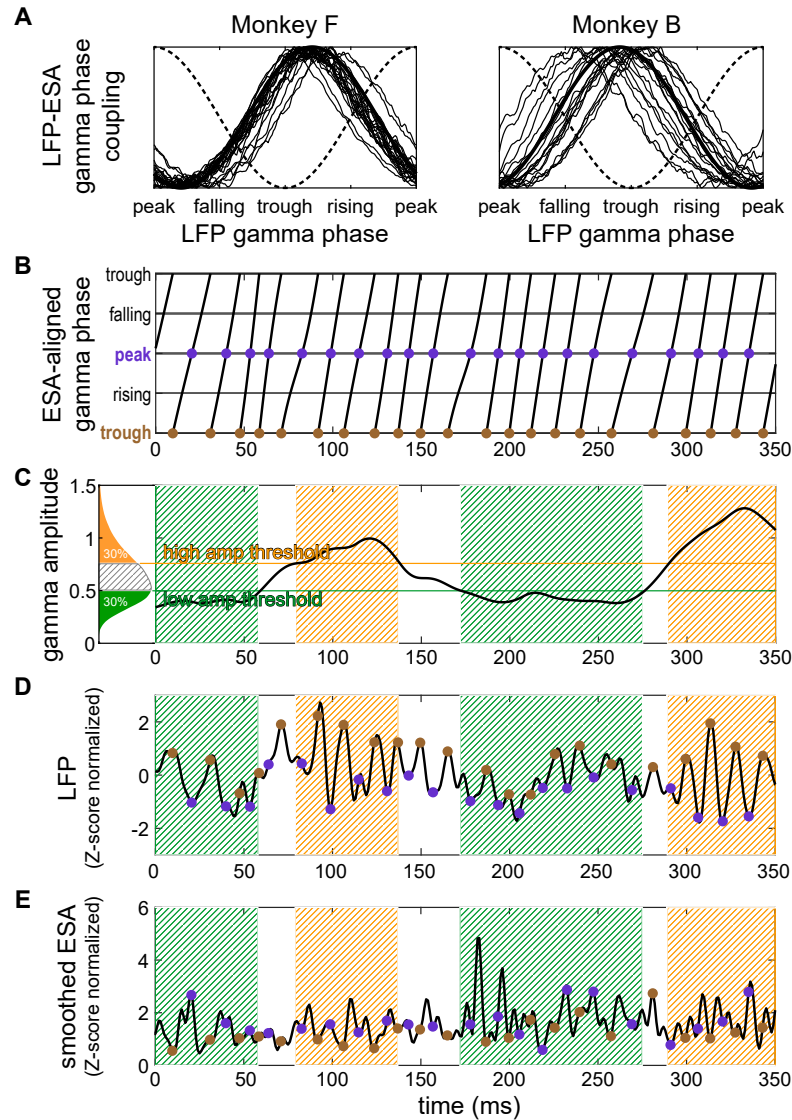


**Figure 3.3: Extraction of gamma phase- and amplitude-specific neural signals.**

**A.** Normalized spike-field coupling in the gamma frequency range, computed from ESA and LFP signals, for all the recording sites for each animal (thin lines for each site, bold line for the mean across sites). The peak of spiking activity consistently occurs at roughly the trough of LFP's gamma cycle (indicated by dotted line), as expected for the superficial layer [225]. By shifting LFP's gamma phase by the appropriate amount, individually for each trial set, we attain the ESA-aligned gamma phase, which is used as a proxy for excitability gamma phase throughout the rest of the analysis.

**B.** Time course of ESA-aligned gamma phase corresponding to a 350ms snippet of a trial. The locations of peaks are marked with purple dots, and excitability troughs with brown dots.

**C.** Corresponding gamma amplitude with 30% highest and 30% lowest thresholds marked with horizontal lines. The thresholds are computed from the distribution of amplitudes gathered across the whole set of trials, shown to the left of the main plot. Periods of time when the amplitude surpassed the high threshold are shaded in orange, and periods of time below the low amplitude threshold are shaded in green.

**D.** The corresponding LFP neural activity with precise peak and trough times of the ESA-aligned gamma phase identified in (B), and high and low amplitudes identified in (C). By using the corresponding samples of the neural activity (either purple or brown dots for peak vs trough, or orange or green time periods for high vs low amplitude, or a combination of both), we can compute the amount of SIC within the selected components of the neural activity. Note that the LFP is obtained by low-pass filtering the recorded signal and thus each value represents neural activity from a small time window around it.

**E.** Same as in (D), but for the corresponding ESA signal.

Next, we would like to know when in each gamma oscillatory cycle neuronal activity is maximal, as a proxy for maximal excitability. Ideally, phases of high (or low) excitability should roughly correspond to high (or low) spiking activity. Unfortunately, the recorded ESA reflects only a small number of neurons next to the recording site, resulting in a signal that is too noisy to reliably extract gamma phase and amplitude. On the other hand, while the LFP provides a clean and reliable measure of the local populations' rhythmic activity, its recording is affected by conduction delays and phase-shifts that depend on the recording electrode impedance as well as its precise location and orientation within the neural tissue [16, 17, 84, 169], making it a poor proxy for excitability's phase. To resolve this issue, we related gamma phase information from the LFPs to spiking activity contained in the ESA by computing the mean ESA value for each LFP gamma phase, thus obtaining an estimate for the spike-field coupling. By subtracting the phase for which spike-field coupling was maximal from  $\Phi_{LFP}$  we acquired the ESA-aligned gamma phase  $\Phi_{ESA}$ , which served as a proxy for excitability gamma phase throughout the entire analysis. For the amplitude of excitability's gamma rhythm, we kept LFP's amplitude  $A_{LFP}$ .

### 3.2.5.2 Phase and amplitude dissociation, wavelet transform

Extraction of gamma phase-specific components of the neural recording signals  $y$  was performed before using a wavelet transform  $W_f$  to obtain a frequency-resolved neural signal representation, while dissection with respect to gamma amplitude was performed thereafter. Applying these three operations in sequence yields the dissected and spectrally resolved neural activity  $\tilde{z}(t, f) = D_A[W_f \circ D_\varphi[y(t)]]$ . Here we write amplitude and phase dissection as formal operations  $D_A$  and  $D_\varphi$ , respectively, which were realized as follows.

For performing phase dissociation, we first determined the time points  $t_{k\varphi}$  at which the excitability phase passed through a desired target phase (e.g.,  $\varphi = 0$  for peaks, or  $\pi$  for troughs). These times were then used to create a new signal  $D_\varphi[y]$  by sampling from the original signal  $y(t)$  (LFP or ESA) at those points. In conjunction with the then following integration over time during the wavelet transform, we can formally write this notching operation by using the  $\delta$ -distribution:

$$D_\varphi[y](t) := \sum_k \delta(t - t_{k\varphi})y(t).$$

Note that in order to obtain the phase-dependency curves of the SIC, we evaluated it for a finite set of gamma phases with equal spacing. For this reason, we wanted the 'notched' signal  $y(t_{k\varphi})$  to represent not only activity at exactly the time point  $t_{k\varphi}$ , but also in its vicinity. This was trivially the case for the LFP since it was originally obtained by low-pass filtering. For the more rapidly varying ESA, we had to apply a second bandpass filter (see description above), in order to avoid 'missing' an activation peak by notching the signal at a slightly different time.

Amplitude dissociation was realized by first obtaining the distribution of gamma amplitudes throughout each individual recording session. From this distribution, we selected the 70th (and 30th) percentiles to use as high (and low) amplitude thresholds  $A_{hi}$  (and  $A_{low}$ ). Using these thresholds, we selected time periods exhibiting high (or low) oscillation amplitudes by means of indicator functions:

$$I_{hi}(t) = \Theta(A(t) - A_{hi})$$

$$I_{low}(t) = \Theta(A_{low} - A(t))$$

where  $\Theta$  denotes the Heaviside function. Using these indicator functions, the amplitude specific spectra  $D_A[\tilde{y}](t, f)$  takes the form

$$D_A[\tilde{y}](t, f) := I_{hi/low}(t)\tilde{y}(t, f)$$

If only phase dissection was performed (no amplitude selection), we used the identity function for  $D_A$ , thus  $D_A[\tilde{y}] = \tilde{y}$ , and if only amplitude dissection was performed (no phase selection), we used the identity function for  $D_\phi$ , thus  $D_\phi[y] = y$ .

### 3.2.5.3 Spectral Coherence

To evaluate how much the luminance fluctuation  $x(t)$  of a shape contributed to the neural activity  $z(t)$ , we utilized spectral coherence (SC). First, we computed the spectrograms  $\tilde{x}(t, f)$  and  $\tilde{z}(t, f)$  where  $f$  is the frequency and  $t$  is the time, using a wavelet transform with Morlet kernels. Here  $\tilde{z}(t, f)$  represents the neural signals which already underwent phase- and/or amplitude dissociation in conjunction with the wavelet transform as described in the preceding section. The transform yields complex valued coefficients representing the amplitude and phase of the signals. By evaluating the normalized cross-correlation between  $\tilde{x}$  and  $\tilde{z}$  we obtained the spectral coherence measure

$$SC_{xy}(f, \tau) = \frac{\left| \sum_{p,t} \tilde{x}(f, t) \cdot \tilde{y}(f, t + \tau) \right|^2}{\left( \sum_{p,t} |\tilde{x}(f, t)|^2 \right) \left( \sum_{p,t} |\tilde{y}(f, t + \tau)|^2 \right)}$$

where  $\tilde{x}^*$  indicates the complex conjugate of  $\tilde{x}$ ,  $\tau$  is the lag between the two signals, and where the sums are performed over the population of trials  $p$  included in the computation for the time points  $t$  in each trial.

Due to the normalization terms in the denominator, the values of  $SC_{xz}$  lie between zero and one. All integrals were computed over all times for which  $t$  and  $t + \tau$  lie within a selected time period during a trial, i.e. from the beginning of the second morph cycle until 200ms before the monkey's response. Summation was performed either over all trials from all recording sites for cumulative population analyses, or over individual sets of trials from single sites, separated by the attended location.

Once SC is calculated, we compute the pooled value  $\overline{SC}$  over a region of interest in frequency-time lag space to reduce a two- dimensional result to a single value. The region of interest was defined as a frequency dependent cone of width  $\pm \frac{7}{6}T$  around  $\frac{1}{2}T + t_{onset}$ , where  $T = 1/f$  and  $t_{onset}$  denotes the onset delay of the neural response in V4 after stimulus onset which was 50ms in monkey F and 60ms in monkey B (see Grothe et al., 2018 [99]). We first took the average across lags within the frequency-dependent region of interest, and then took the mean of the time averages from 5 up to 15 Hz. 15 Hz was selected as upper the limit, since the majority of the individual sets results did not yield significant SC above this value.

### 3.2.5.4 Confidence intervals and statistical tests

For assessing significance of each  $\overline{SC}$  measure, we computed the 95% chance level of its value being different from zero (indicated by the gray shading towards the bottom of each plot in figures 3.4A, 3.6A and 3.7). This was done by taking the 95th-percentile from the distribution of  $\overline{SC}$ -measurements gathered by pairing the neural recording signal with 200 surrogate luminance flicker signals.

95% confidence intervals for  $\overline{SC}$  were gathered by bootstrapping across trials. From a set  $S$  of  $N$  trials, we randomly sampled trials with replacement, generating another set  $S^*$  with the same number of trials  $N$ , many of which are duplicates of each other. Using this new data, we calculated our desired test statistic  $\overline{SC}^*$ . This procedure was repeated 20000 times, creating a distribution of  $\overline{SC}^*$  values, from which we extracted the 2.5% and 97.5% quantiles.

In order to assess whether a test statistic  $\overline{SC}_1$  (computed from data extracted from set  $S_1$  with  $N_1$  trials) is significantly different from  $\overline{SC}_2$  (computed from set  $S_2$  with  $N_2$  trials), a non-parametric permutation statistical test was used [144]. By randomly shuffling the trials between the two sets, we created new sets  $S_1^*$  with the same number of trials  $N_1$  and  $S_2^*$  with  $N_2$  trials, each containing no trial duplicates but rather a mixture of trials from the original sets, which are then used to compute the test statistic  $\overline{SC}_1^* - \overline{SC}_2^*$ . This procedure was repeated 20000 times, generating a null distribution for the test statistic, allowing to calculate the significance level p-value by evaluating the proportion of this distribution that fell above/below the true value of the statistic,  $\overline{SC}_1 - \overline{SC}_2$ , computed from the original data sets. In cases where 100% of the null distribution is above/below the true statistic, the p-value is reported as  $p < 1/20000$ .

To assess whether a distribution of  $\overline{SC}$ -measures is significantly different between two conditions (i.e. whether the data clouds in the scatter plots in upcoming figures 3.4B and 3.6B lie above or below the diagonal), we determined whether the ratios between the  $\overline{SC}$  values for individual sets are significantly different from 1 by using the Wilcoxon signed rank test on the distribution computed via  $\log(\overline{SC}_1/\overline{SC}_2)$ .

### 3.3 RESULTS

For investigating whether and how attention-dependent signal transfer is affected by V4's gamma phase and amplitude, we analyzed local field potentials (LFP) and multi-unit spiking activity (measured as entire spiking activity, ESA) recorded from the superficial layers of area V4 in two macaque monkeys (*Macaca mulatta*). During recording, the animals were engaged in a demanding shape tracking task requiring the monkeys to attend to one of two concurrently presented dynamic stimuli within the recorded population's receptive field (RF) (see Fig. 3.2A and methods section for details). The two stimuli consisted of complex shapes, which, after an initial static period, morphed through a series of different shapes throughout the trial. At the beginning of each trial, one of the two stimuli was cued. The task for the monkey was to attend to the cued stimulus while maintaining fixation, and to respond when its initial shape reappeared in the morphing sequence. The other, non-attended stimulus had to be ignored. The number of morph-cycles that the stimuli went through before returning to the initial shape was randomized. The neural signals included in this analysis were taken from the start of the second morph cycle until 200 ms before a correct behavioral response. The first cycle was excluded since it never morphed into the target shape and thus would not require the animal to pay 'full' attention to the target shape in this particular time interval.

Crucially, the two stimuli were tagged by independent and behaviorally irrelevant random luminance fluctuations, with a luminance change every 10ms. This allows us to evaluate stimulus information content (SIC) in V4 activity by computing the spectral coherence between the neural activity and the luminance signals (see Fig. 3.2B). Spectral coherence provides a frequency- and time-delay-resolved correlation measure between two signals. By pooling across relevant lag and frequency bins, we acquired a single

value  $\overline{SC}$  as a measure for the average SIC of the shapes' luminance fluctuation within the recorded neural activity.

In order to probe whether a potential SIC modulation is aligned to excitability phase as predicted in figure 3.1, we employed ESA as a proxy for excitability. Specifically, we first identified which LFP gamma phase was associated with maximum ESA, and then shifted the LFP gamma phase by the appropriate amount for each recording site giving us the ESA-aligned gamma phase. Throughout the whole analysis, this is the gamma phase employed as a proxy for excitability's gamma phase (Fig. 3.3A).

To quantify SIC in dependence on gamma phase and amplitude, we extracted neural activity specific to each phase of the gamma cycle and separately for periods of high and low gamma-band amplitudes. We then computed  $\overline{SC}$  between these phase and amplitude-specific signals and the luminance fluctuations of the attended and non-attended stimuli (see Fig. 3.3 and methods section for details).

### 3.3.1 Information modulation by phase

We extracted components of the neural signals associated with a specific gamma phase by selecting the discrete time points that correspond to that particular phase, and sampled the neural signals at those points. In the example shown in figure 3.3B, we marked the time points corresponding to ESA-aligned gamma peaks (in purple) and troughs (in brown). The dots in figures 3.3D and E indicate which samples from the LFP and ESA signals, respectively, will be obtained when selecting at peaks (in purple) or troughs (in brown). The method is not limited to sampling just from the peak or from the trough, allowing to extract a signal specific to any desired phase. By computing  $\overline{SC}$  between the phase-specific neural activity signals and the input stimuli, we can assess the amount of attended or non-attended SIC in dependence on gamma phase.

For the attended stimulus (Fig. 3.4A, left two columns), SIC at peaks ( $\overline{SC}_{peak}$ ) was significantly larger than SIC at troughs ( $\overline{SC}_{trough}$ ), consistently across monkeys and signals ( $p < 0.00005$  for both animal's LFP signals,  $p = 0.0002$  for monkey F ESA,  $p = 0.003$  for monkey B ESA, non-parametric permutation test). In contrast, for the non-attended stimulus, there was no significant difference between SIC at peaks and troughs for ESA. The LFP showed a significantly higher SIC at peak vs trough for monkey B ( $p = 0.0021$  for monkey B LFP). The absolute modulation strength, calculated via  $\overline{SC}_{peak} - \overline{SC}_{trough}$ , is significantly higher for the attended stimulus than for the non-attended stimulus for both animals and neural signal types ( $p < 0.00005$  for both animal's LFP,  $p = 0.0045$  for monkey F ESA,  $p = 0.0094$  for monkey B ESA). Aside for a few values near the ESA-aligned gamma trough for monkey B's non-attended ESA results, all observed  $\overline{SC}$ -values were significantly greater than chance level, indicating that information might be transferred during all gamma phases, even though to different extents. For monkey B, the  $\overline{SC}$ -values for the attended signal are significantly higher than their non-attended counterpart across all phases ( $p < 0.00005$ ). For monkey F, the difference between attended and non-attended conditions is significant at the peaks ( $p < 0.00005$ ). At the falling phase for monkey F LFP and at the trough phase of the monkey F ESA conditions, the non-attended  $\overline{SC}$ -values are slightly higher than the attended ones, but after correcting for multiple comparison across all the phases, this effect is not significant.

The effect of a higher SIC at peaks than at troughs for the attended stimulus was consistent across individual recording trial sets. The scatter plots in the two leftmost columns of Fig. 3.4B display  $\overline{SC}_{peak}$  vs  $\overline{SC}_{trough}$  for each individual trial set for the attended stimulus. The majority of data points show significantly higher SIC at peaks

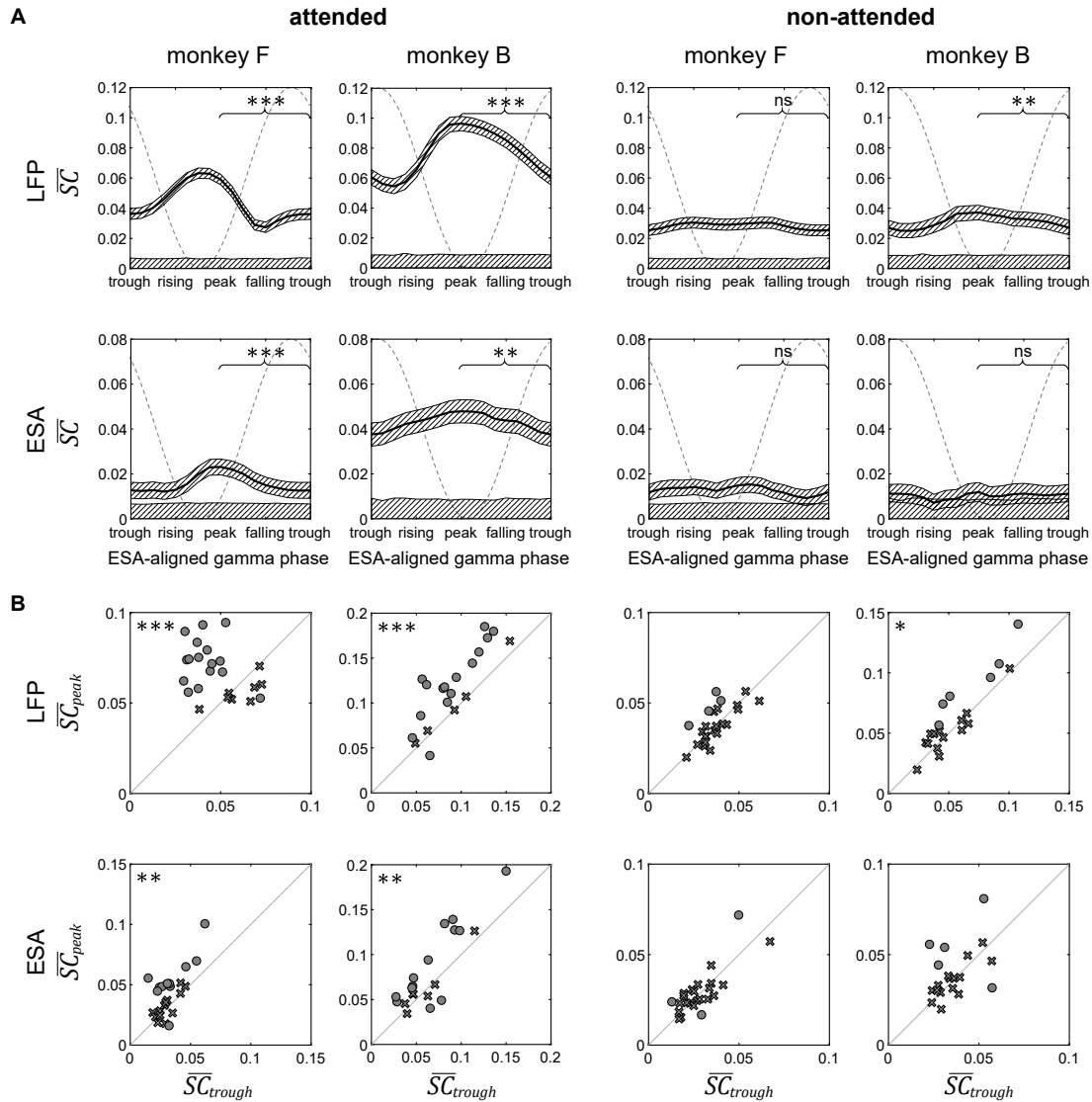


**Figure 3.4: Stimulus information content is modulated by V4's gamma phase.**

**A.** SIC dependence on phase for data pooled across all sessions. In each plot, we display how  $\overline{SC}$  depends on the ESA-aligned gamma phase (horizontal axis) from which the neural signal is extracted. The shading around each line corresponds to the 95% confidence interval. Significance of the difference between  $\overline{SC}_{peak}$  vs  $\overline{SC}_{trough}$  is indicated in each plot (\* $p < 0.05$ , \*\* $p < 0.01$ , \*\*\* $p < 0.001$ ). The gray shading at the bottom of each plot corresponds to the 95% chance level (values below this level indicate no significant SIC). The grey dashed sinusoid line indicates the corresponding average LFP phase.

**B.** SIC at peaks versus troughs of the ESA-aligned gamma phase for individual sets. For each condition, we display a scatter plot of  $\overline{SC}_{peak}$  vs  $\overline{SC}_{trough}$  pairs. In the scatter plots, individual sets that exhibit a significant difference ( $p < 0.05$ ) are marked with a circle, and with a cross otherwise. The significance of the group distribution, i.e. whether it lies significantly below or above the diagonal, is marked with black asterisks on the side that contains significantly more trial sets (\* $p < 0.05$ , \*\* $p < 0.01$ , \*\*\* $p < 0.001$ ).

rather than troughs ( $p < 0.05$ , marked with circles; 15 of 24 for monkey F LFP, 14 of 20 for monkey B LFP, 10 of 24 for monkey F ESA, and 11 of 20 for monkey B ESA). Note that only a few trial sets exhibit significantly lower SIC at gamma peaks (1 of 24 for monkey F LFP, 1 of 20 for monkey B LFP, 1 of 24 for monkey F ESA, 2 of 20 for monkey B ESA).

We assessed the individual set's group statistics by determining whether the distribution of log-ratios,  $\log(\overline{SC}_{peak}/\overline{SC}_{trough})$ , is significantly higher or lower than 0, indicated by the black asterisks in the scatter plots of Fig. 3.4B (Wilcoxon signed rank test). For the attended stimulus, the peak SIC was significantly higher than the trough SIC across both monkeys and both neural signals ( $p = 0.0006$  for monkey F LFP,  $p = 0.0007$  for monkey B LFP,  $p = 0.0062$  for monkey F ESA, and  $p = 0.0089$  for monkey B ESA). For the non-attended stimulus, the scatter plots show a tendency to exhibit higher  $\overline{SC}_{peak}$  than  $\overline{SC}_{trough}$  with more significant results above the diagonal, however, the group statistic was only significant for monkey B's LFP ( $p = 0.0145$ , top right scatter plot in figure 3.4B).

In order to confirm that the phase modulation effects are specific to the gamma-band, SIC modulation by phase was analyzed across multiple frequency bands for both LFP and ESA signals (Fig. 3.5). This was done using the very same procedure as for the main analysis, but using phase computed from LFP bandpassed with different center frequencies. This control analysis revealed that the phase-modulation effect is indeed strongest for the gamma band.

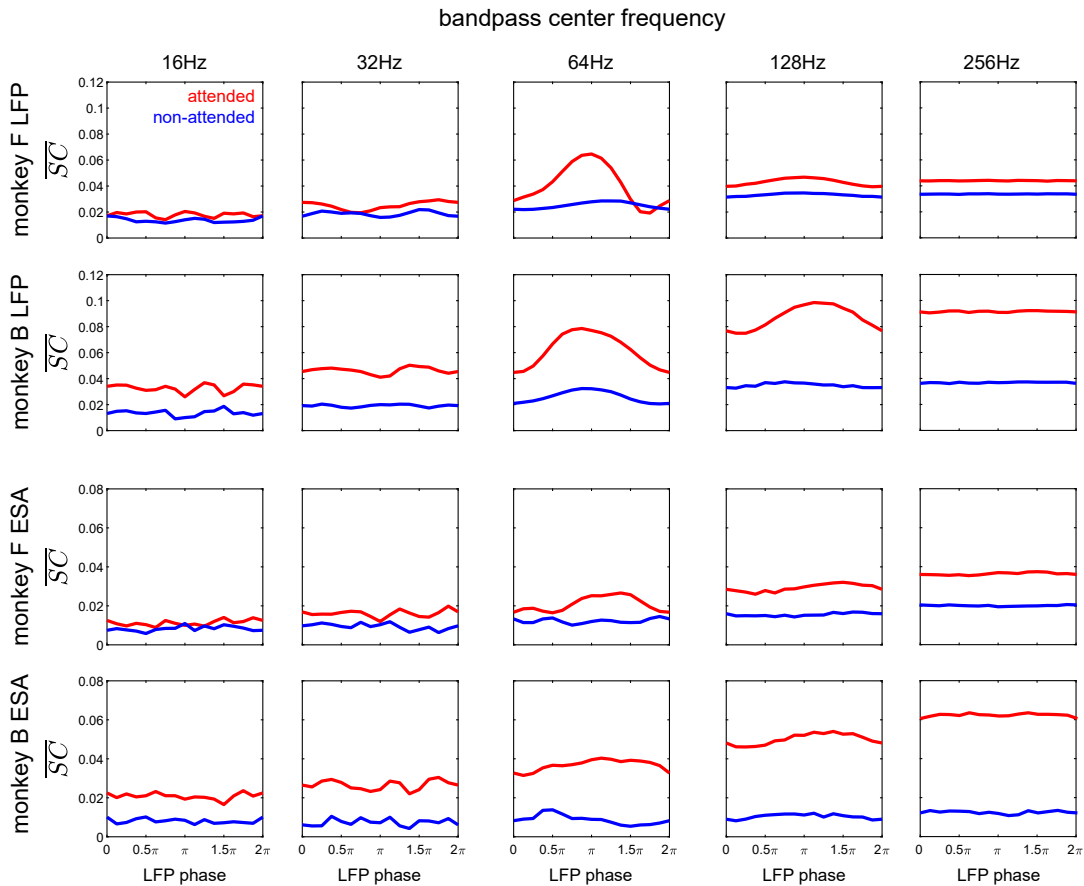


**Figure 3.5: SIC modulation by phase for multiple frequency bands.**

SIC dependence on phase for data pooled across all sessions, with the phase-specific neural activity extracted in the same manner as before, but using phase computed from LFP bandpassed across multiple frequency bands. The horizontal axis denotes LFP phase with  $\pi$  corresponding to signal troughs, which, in the case of the gamma band (center column), should roughly correspond to excitability peaks.

### 3.3.2 Information modulation by amplitude

For the amplitude dissection, we first gathered the distribution of gamma amplitudes throughout each individual trial set. From this distribution, we selected the 70th (and 30th) percentiles to use as high (and low) cutoff thresholds to select activity from high and low gamma amplitude periods. Using these thresholds, for each trial, we selected the time periods exhibiting high (or low) oscillation amplitudes. In the examples in figure 3.3C, the corresponding periods are indicated by orange and green shading, respectively. In figures 3D and E, the same shading indicates which periods of the LFP and ESA signals were selected by amplitude dissociation. Since the thresholds were computed across a set of trials, the total proportion of each individual trial included in the analysis varied slightly, with most trials' proportion falling within the 20-40% range. On average, the duration of each individual period was around 40ms with 90ms intervals in-between, corresponding to about 8 periods occurring every second. Using these amplitude-specific periods, we evaluated and compared the amount of SIC within high amplitude ( $\overline{SC}_{highAmp}$ ) versus low amplitude gamma oscillations ( $\overline{SC}_{lowAmp}$ ).

When we ran the analysis on a cumulative set of all the trials over all recording sites for the attended stimulus, we found a small increase of SIC in neural activity during high amplitude gamma oscillations in comparison to low amplitude gamma activity (Fig. 3.6A). Aside for monkey F's LFP, the difference between the amplitude conditions is significant ( $p=0.00005$  for monkey B LFP,  $p=0.0229$  for monkey F ESA,  $p=0.0034$  for monkey B ESA). This corresponds to the prediction derived from our hypothesis (cf. Fig. 3.1B). For the non-attended stimulus, the analysis did not reveal any significant differences between SIC within periods of high versus low gamma activity.

Results from analyzing individual sites corroborated the cumulative outcomes (Fig. 3.6B). There are few individual trial sets that showed a significant difference due to the smaller size of the effect. For the attended stimulus, the majority of the sites with a significant difference did indicate increased information present during periods of high amplitude oscillations as seen in the scatter plots in the left two columns of Fig. 3.6B. When we looked at the distribution of the ratios  $\log(\overline{SC}_{highAmp}/\overline{SC}_{lowAmp})$ , except for LFPs from monkey B, all conditions exhibited a significant shift towards a higher SIC for high amplitude gamma, as indicated by the black asterisks ( $p=0.0057$  for monkey F LFP,  $p=0.0032$  for monkey F ESA,  $p=0.0053$  for monkey B ESA).

For the non-attended stimulus (right two columns of Fig. 3.6B), SIC did not show any significant differences for the individual sets, except for monkey B's ESA signal. This was the only case for which we found that  $\overline{SC}_{highAmp}$  is significantly lower than  $\overline{SC}_{lowAmp}$  ( $p=0.0047$ ).

### 3.3.3 Information modulation by phase and amplitude

Selections of the neural activity with respect to phase and amplitude were combined to acquire LFP and ESA activity associated to the co-occurrence of a particular gamma phase and amplitude (Fig. 3.3).

In figure 3.7, the results for the SIC computed from the set of all trials collected from all the recording sites is displayed, with the high amplitude results in orange and low amplitude results in green. Corroborating the hypotheses in Fig. 3.1B, the data exhibited higher SIC modulation by gamma phase within high amplitude periods and lower SIC modulation by phase for the low amplitude periods.

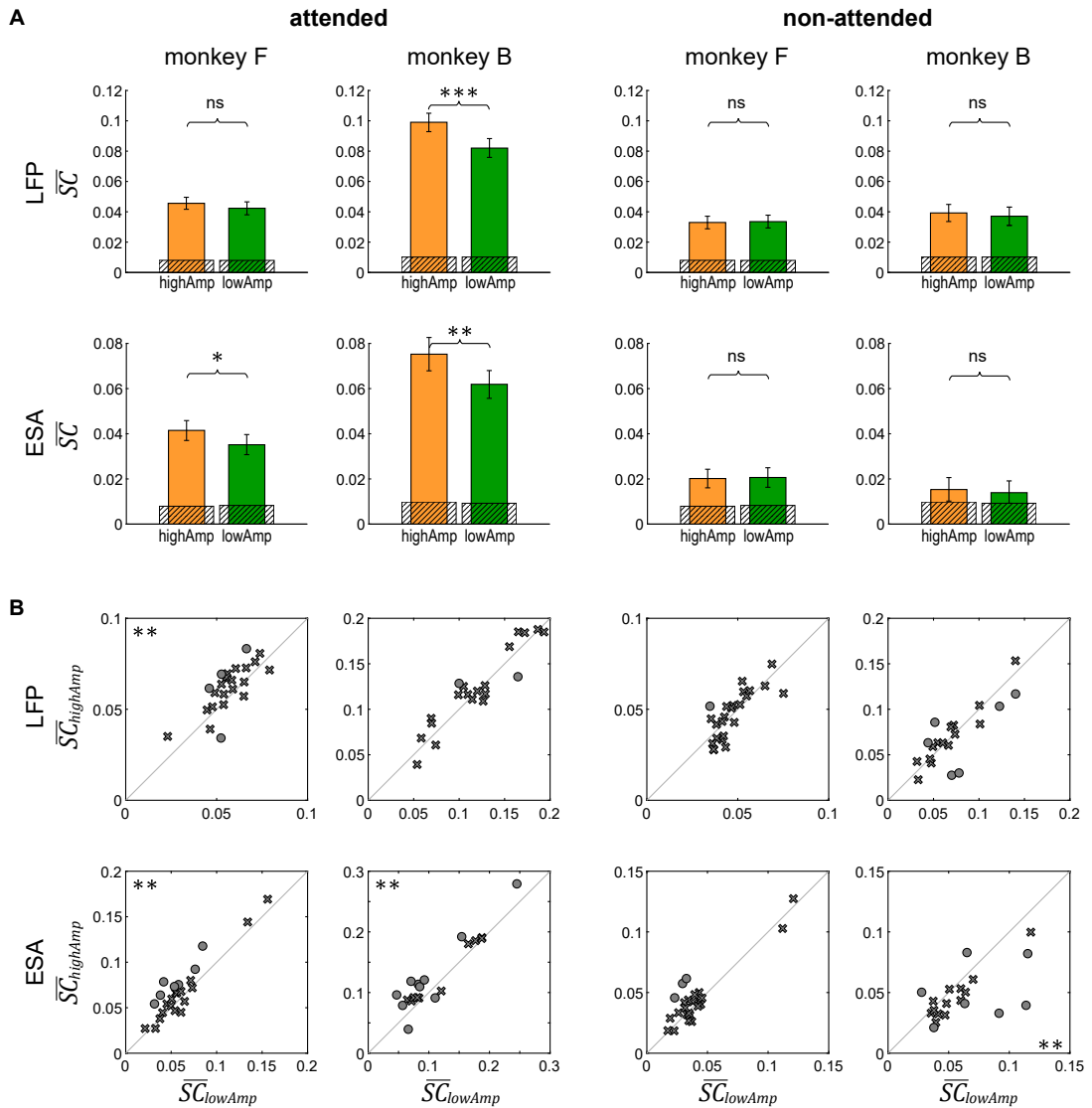


**Figure 3.6: Stimulus information content is modulated by V4's gamma amplitude.**

**A.** SIC extracted from periods with high- versus low-amplitude gamma oscillations for data pooled across all recording sessions. In each plot, for the specific condition as indicated by the row and column labels, we display pairs of  $\overline{SC}_{highAmp}$  (in orange) and  $\overline{SC}_{lowAmp}$  (in green), separately for each animal, neural data type, and attention condition. The error bars indicate the 95% confidence interval. The gray shading at the bottom of each bar indicates the 95% chance level for that value. Significance level of the differences is indicated above each pair of bars, computed via permutation testing across the trials (\* $p < 0.05$ , \*\* $p < 0.01$ , \*\*\* $p < 0.001$ ).

**B.** SIC extracted from periods of high versus low gamma neural activity for individual sets. For each condition, we display a scatter plot of  $\overline{SC}_{highAmp}$  vs  $\overline{SC}_{lowAmp}$  pairs. In the scatter plots, sets that exhibit a significant difference ( $p < 0.05$ ) are marked with a circle, and with a cross otherwise. The significance of the group distribution, whether it lies significantly below or above the diagonal, is marked with black asterisks on the side that contains significantly more sets (\* $p < 0.05$ , \*\* $p < 0.01$ , \*\*\* $p < 0.001$ ).

The outcome lends itself to multiple tests: comparing SIC at high versus low amplitudes at peak and trough (significance indicated at the bottom of each plot at peak and trough phases in black) and comparing SIC at peak versus trough phases in either high or low amplitude conditions (significance indicated at the top of the plot with colors corresponding to the amplitude conditions).

The difference between high and low amplitudes for the attended stimulus was strongly phase-specific: while SIC near peaks within high gamma amplitude activity was significantly larger than SIC within low gamma amplitude activity ( $p < 0.00005$  for monkey F and monkey B LFP,  $p = 0.0314$  for monkey F ESA,  $p = 0.0020$  for monkey B ESA), there were no significant differences near troughs. Consequently, SIC modulation by gamma phase was higher in the high amplitude condition ( $\overline{SC}_{peak}$  is greater than  $\overline{SC}_{trough}$  with  $p < 0.00005$  for all data sets), and lower (but still significant in three out of four cases) in the low amplitude condition ( $p < 0.00005$  for monkey F and monkey B LFP,  $p = 0.009$  for monkey F ESA and not significantly different for monkey B LFP). The absolute modulation strength,  $\overline{SC}_{peak} - \overline{SC}_{trough}$ , is significantly larger for the attended signal versus the non-attended signal in the high amplitude condition ( $p < 0.00005$  for both animals' LFP,  $p < 0.00005$  for monkey F ESA,  $p = 0.0025$  for monkey B ESA) and decreases for the low-amplitude condition (still significant with  $p < 0.00005$  for both animals' LFP, not significant for ESA). Overall, this corroborates the prediction from the corresponding

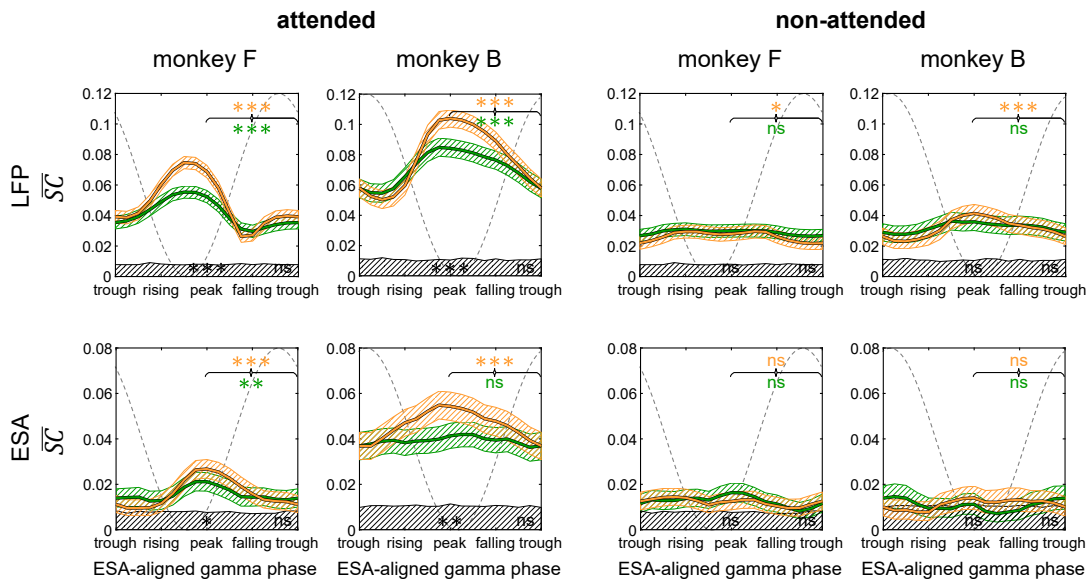


**Figure 3.7: Stimulus information content is modulated by V4's gamma amplitude.**

**A.** SIC extracted from periods with high- versus low-amplitude gamma oscillations for data pooled across all recording sessions. In each plot, for the specific condition as indicated by the row and column labels, we display pairs of  $\overline{SC}_{highAmp}$  (in orange) and  $\overline{SC}_{lowAmp}$  (in green), separately for each animal, neural data type, and attention condition. The error bars indicate the 95% confidence interval. The gray shading at the bottom of each bar indicates the 95% chance level for that value. Significance level of the differences is indicated above each pair of bars, computed via permutation testing across the trials (\* $p < 0.05$ , \*\* $p < 0.01$ , \*\*\* $p < 0.001$ ).

**B.** SIC extracted from periods of high versus low gamma neural activity for individual sets. For each condition, we display a scatter plot of  $\overline{SC}_{highAmp}$  vs  $\overline{SC}_{lowAmp}$  pairs. In the scatter plots, sets that exhibit a significant difference ( $p < 0.05$ ) are marked with a circle, and with a cross otherwise. The significance of the group distribution, whether it lies significantly below or above the diagonal, is marked with black asterisks on the side that contains significantly more sets (\* $p < 0.05$ , \*\* $p < 0.01$ , \*\*\* $p < 0.001$ ).

curves in figure 3.1B: for the attended signal, SIC modulation by phase is increased during high amplitude gamma activity and decreased during low amplitude gamma activity.

Similar to the previous phase-only analysis (cf. Fig. 3.4), SIC modulation by phase was reduced dramatically for the non-attended stimulus when compared to the attended stimulus (Fig. 3.7 right two columns). However, in the high amplitude condition, we observed more cases with a significantly higher SIC at the peak versus the trough ( $p=0.0274$  for monkey F LFP,  $p=0.0003$  for monkey B LFP). In the low amplitude condition, the differences between peaks and troughs became insignificant. There were no significant differences between the high and low amplitude conditions at any phase.

### 3.3.4 *Controlling for eye-movements.*

Throughout the recording sessions, if the animal moved its eyes away from the fixation point, the trial was immediately terminated and subsequently excluded from the analyses. However, there were still microsaccades within the close vicinity of the fixation point occurring at a rate of 0.82Hz for monkey F and 0.77Hz for monkey B (on average across the recording sessions). Microsaccades have been previously reported to modulate firing rate [136] and gamma-band activity in V4 within a 400ms period following each microsaccade [30]. In order to account for any possible effects of microsaccades, we ran a control analysis, repeating the entire procedure on the data set excluding 400ms periods following every microsaccade.

Furthermore, we detected small but significant differences in the overall distribution of eye-positions within the fixation window, between attended vs non-attended conditions as well as between the periods corresponding to high vs low gamma amplitudes. These differences could potentially lead to a different coverage of the stimuli by the V4 RFs, possibly affecting SIC of the population's activity. To address this issue, we ran a second control, repeating the analysis on a subset of data by removing periods of data until a Kolmogorov-Smirnoff test was unable to detect a difference in the corresponding distributions of eye position ( $p > 0.1$ ).

The results from both control analyses revealed almost identical SIC measurements and significance test results (not shown) compared to the ones presented in figures 3.4, 3.6 and 3.7. Throughout all the test results, the only notable change happened for the small difference between SIC at peak versus SIC at trough for the non-attended signal in monkey F's LFP activity: the significance of the difference in figure 3.4A (top plot in third column) changes from  $p=0.0587$  to  $p=0.0245$  becoming significant in the eye-position control analysis, and changes from  $p=0.0274$  to  $p=0.158$  becoming not significant for the high amplitude condition in figure 3.7 when performing the microsaccade-control analysis. These findings indicate that the results of our analyses are not confounded by eye movements.

## 3.4 DISCUSSION

In the present work we tested the prediction of the RBS mechanism that attention-dependent visual stimulus information is not continuously dispersed over time but instead occurs selectively in pulsed information packages, modulated by phase and amplitude of V4's gamma-rhythmic activity.

Our analysis reveals that the luminance fluctuations tagging the attended stimulus are expressed most strongly within neural activity close to the phase in the gamma oscillation cycle where local spiking peaks (i.e. close to the LFP troughs), showcasing a pattern of modulation significantly different from the non-attended signal. During periods with high amplitude gamma oscillations the overall SIC for attended stimuli is higher in the V4 activity than during low amplitude oscillations, whereas for non-attended stimuli there is no significant difference. SIC's increase with amplitude is particularly strong at the peak of spiking activity and absent at the trough. Since the peaks of spiking activity should roughly correspond to the peaks of excitability, these results corroborate central predictions derived from the RBS mechanism.

Certain details of the results seem to deviate from the predictions illustrated in figure 3.1B (bottom plot). For instance, when comparing attended and non-attended SIC, our expectation was that the non-attended SIC should be at least as large as the attended SIC in the vicinity of excitability troughs. However, for monkey B, we find that the attended signal is consistently better expressed across all phases. This may be explained by a temporal dispersion of information across phase, which occurs due to multiple factors. First, the precision of phase estimation itself is limited by noise in the recorded neural activity. Additionally, we also smoothed the neural activity prior to the phase-specific signal extraction, such that the value of the signal at each time point represents a temporal window of activity around it. Finally, computing SIC based on spectral coherence involves comparing the neural recording and luminance fluctuation signals with wavelets that are centered at the time of interest but also extend in temporal space. Taken together, these methodological limitations all lead to the luminance flicker signal being partially mapped to phase ranges at which it does not actually occur, thereby increasing SIC in low-SIC ranges and decreasing SIC in the high-SIC ranges of the oscillatory cycle. In consequence, our analysis is likely to underestimate the magnitude of SIC modulation by phase.

Dissociating signal content with respect to gamma amplitude could be subject to a similar reduction in SIC modulation amplitude. If we assume constant contributions of noise throughout the recordings, precision of phase estimation will decrease during periods of low gamma amplitude activity. Such an effect may contribute to the differences between high and low amplitude SIC results observed in figure 3.7 where we perform a simultaneous phase and amplitude-specific signal extraction.

The results for the non-attended signal provide further insight into the details of the RBS mechanism. Here, we observe only weak, or no phase-dependent modulation of SIC. The absence of a strong modulation implies a certain coherence for the non-attended signal with the receiving population in an anti-phasic relationship in order to counteract V4's gain modulation. This is compatible with a weak level of coherence between non-attended V1 and V4 as observed in Grothe et al., 2012 [98]. On the other hand, a weak modulation of non-attended SIC in V4 could emerge if there is no coherence between non-attended V1 and V4 as observed in Bosman et al., 2012 [29]. In principle, our results are also compatible with a strong anti-phasic coherence between sender and receiver, however, such a strong coherence has never been observed experimentally, even though it would be functionally optimal for selective information routing. This may be due to how the phase-locked states between the sending and receiving populations are established. Previous studies have shown evidence that gamma activity acts in a feedforward manner, with the upstream populations' gamma rhythm entraining the gamma in downstream areas [15, 29, 158, 187, 188, 225]. With this in mind, it is up to the sending population processing the attended stimulus to entrain V4 with its own gamma

rhythm, whereas the population processing the non-attended stimulus fails to entrain V4, remaining primarily uncoupled. Essentially, the presynaptic populations compete to entrain their postsynaptic targets. Even though the effect of attention on rates in V1 has been reported to be relatively weak in numerous studies [142, 149, 153, 163, 165, 194], modeling studies suggest that even a moderate advantage for the attended signal can be sufficient to entrain the receiving V4 population [102]. It has also been reported that the gamma peak frequency increases slightly with attention in V1 [29], which further promotes its ability to entrain the receiving population [43].

Our predictions for how SIC is encoded within V4's neural activity relied upon the assumption that the information from the sending populations arrives in pulsed packages at V4. In its simplest form, such an encoding can be realized by synergistically combining synchronous dynamics with a rate coding scheme [4]. Womelsdorf et al., 2012 [249] demonstrated such a scheme in V1, showing that the firing-rate at the peaks of gamma-oscillatory activity is more informative for stimulus orientation. A complementary scheme for encoding information relative to gamma activity is phase-coding. Using the same orientation-selectivity data set, Vinck et al., 2010 [231] showed support for such a phase-coding scheme with the observation that stronger activation by a stimulus leads to spikes emitted earlier in the gamma cycle. Cumulatively, regardless of precisely how stimulus information is encoded within each gamma-cycle of the sending populations' neural activity, the crucial component of RBS is that the gamma-rhythmic coordination of said activity increases its postsynaptic impact in a periodic manner, effectively delivering information to the receiving population in the form of gamma-rhythmic packages [10, 76, 209, 213, 254].

In our results, the higher level of attended information content at excitability peaks in the receiver population in V4 cannot be explained solely by its oscillatory activity. Indeed, having more spikes in the vicinity of V4 excitability peaks has the potential to encode more information at these phases, regardless of any inter-areal phase coherence between the sending and the receiving population. However, if spikes from sending populations arrived unaligned to V4's gamma oscillation, we would expect a similar level of SIC phase-modulation for both the attended and the non-attended signals. Further, attention-dependent differences of mean rate in the sender populations do not suggest the big difference observed between the phase-dependent modulation of SIC of attended and of non-attended stimuli, because the mean firing rates in the sending populations are not strongly modulated by attention [142, 149, 153, 163, 165]. Therefore, we expect that selective phase coherence ensures that information packages for predominantly the attended signal arrive close to the optimal phase at V4 explaining the qualitative difference of the phase modulation between attended and non-attended stimuli.

While selective routing of signals and information based on the synchronization in the gamma band is a consistent mechanism [77, 79, 122, 123], it is conceptually difficult to draw valid conclusions on information transmission from measuring gamma coherence within or between cortical areas alone [40]. Developing complementary approaches to better link the observed dynamics of neuronal activity to the proposed function in information processing is thus necessary. A significant advance was made by showing that the power of gamma-band activities at two recording sites maximally correlate when these gamma oscillations are in a favorable phase relationship [250]. Consistent with this finding, it was demonstrated that Granger causal influence from upstream to downstream visual areas in the gamma band is enhanced by attention [15], going along with increased gamma phase synchronization. However, since gamma activity is an internal rhythm, the relation to the transmission of stimulus information remained unclear. In

our approach, as opposed to investigating internal gamma rhythms alone, we directly estimate the stimulus information that is contained within V4's lower frequency (5 to 15 Hz) activity by computing the spectral correlation between the luminance flicker of the visual stimuli with V4's neural activity. In consequence, the results establish a causal link between V4 gamma dynamics and stimulus content, demonstrating a qualitative difference between how attended and non-attended signals are conveyed through V4.

An impact of the pulsed information transmission scheme of RBS on behavior might occur if the animals need to respond quickly to sudden stimulus changes, which result in neural responses with fast initial transients lasting only a few gamma cycles [218]. If the relevant information for detecting such changes is predominantly contained in these rapid neural responses, it will be crucial whether it arrives at a favorable or unfavorable phase. Arriving at an unfavorable phase would naturally lead to a larger neural response latency, which could delay successful change detection. Indeed, it has been found that larger response latencies are strongly correlated with longer reaction times, possibly caused by such an effect [85]. Further evidence was given by Ni et al., 2016 [172] who demonstrated that both neural responses and reaction times were modulated by the gamma phase in V4 at which a sudden stimulus change occurred and also depended on the V1-V4 interareal coherence [191].

Taken together, our findings directly demonstrate that signals carrying information of attended stimuli occur in short packages, tightly locked to the phase of the gamma-band oscillation, in the vicinity of the excitation maximum of the local target population. The results strongly support previous evidence for differential phase synchronization as a mechanism for attention-dependent selective signal routing. In particular, we established the methods to infer and quantify the properties of pulsed transfer schemes in neural data. Since evidence in support for CTC and RBS have also been reported across other visual areas [22, 115, 250] and different brain regions [37, 46, 201], our techniques will allow future studies to pinpoint similar processes in other areas, and to investigate whether the dynamical features exhibited by our data point towards a general principle for flexible information processing throughout the brain.

In the previous chapter, a dedicated effort was made to limit the performed analyses exclusively to recordings made within the *superficial layers* of V4. In this section, we explore the reasoning behind this selection criteria, discussing the laminar organization and accompanying functional effects in the visual system. Further, we run the same analysis from the previous chapter on recording sites that were classified as not coming from the superficial layers of V4.

#### 4.1 INTRODUCTION

Laminar structure is present throughout the entire cerebral cortex, showcasing a columnar organization with a canonical arrangement of six layers [166]. In fact, a common name for the visual area V1 is – the striate cortex, with the name given to the area to describe its stripy, layered properties that were evident when scientists were looking at it for the very first time, all the way back in 1700’s [88, 93]. Accordingly, in reference to the striate cortex, area V2 is often called the prestriate cortex, whereas V4 belongs to the extra-striate cortex (which also contains V3, and V5/MT).

The ubiquitous nature of the layered structure is accompanied by a consistent circuit motif connecting different areas throughout the sensory cortex [103]. Anatomically, the visual system is characterized by a very specific laminar connectivity [70, 145]. Briefly, feedforward projections from hierarchically lower areas tend to originate in the superficial (also called supragranular) layers and target the middle layer 4 (the granular layer) of the hierarchically higher areas. The input layer 4 sends projections to the rest of the column, up into the supragranular layers and down into the deep (also called infragranular) layers. Meanwhile, feedback projections tend to originate in the deep layers and target the supra- and infra-granular layers in the upstream areas.

Multiple studies have elucidated the functional processes that parallel the anatomical structure described above. Specifically, the feedforward interactions transmitting bottom-up sensory information are mediated by gamma oscillations, while the feedback interactions are mediated by oscillations in the alpha-beta range (5-20Hz) [15, 34, 158, 225]. In other words, the findings suggests that the supragranular layers relay bottom-up signals containing sensory information through the gamma rhythm, whereas the infragranular layers employ top-down control via the beta-rhythm [52, 72, 187, 227].

Altogether, the existing research indicates that the neural computation processes in the superficial layers are substantially different from the computations performed in the deep layers. In the previous chapter, the goal was to focus on the feedforward gamma-band activity conveying the sensory signals of the visual stimuli. With this in mind, only the available recording sites from the superficial layers were utilized. In this chapter, we take a closer look at the selection criteria (see Fig. 4.1). Further, we also apply the analysis of how stimulus information content (SIC) is modulated by gamma phase and amplitude for the deep layer sites.

## 4.2 RESULTS AND DISCUSSION

### 4.2.1 Identifying the layer of the recording site

The recordings in the experiment were performed using Tungsten intracortical electrodes. Although the intent was to record primarily in the superficial layers of V4, the electrode insertion procedure does not allow for such accuracy, resulting in a mix of recordings across various layers of V4.

In order to identify whether a recording site was within the superficial or deep layers, we utilized two metrics. The first metric involves the shape of the visual evoked potential (VEP) caused by the stimulus onset. The characteristic time course of the VEP for the superficial layers typically shows a negative deflection shortly after the stimulus onset. Conversely, for the deep layers, the VEP shows a positive deflection shortly after stimulus onset [92, 168]. The VEP was computed for each recorded site, by averaging the LFP across all trials for each trial set (see the insets along the horizontal axis in Fig. 4.1). Then, the time point with the highest level of variability between the different trial sets was determined – 125ms after the stimulus onset. The value of the VEP at this time point can then be used to classify the layer of the recording.

The second metric involved measuring the level of spike-field coupling in the gamma frequency range. Spike-field coupling in the gamma frequency range is known to be high in the superficial layers and primarily absent in the deep layers [34, 168]. Spike-

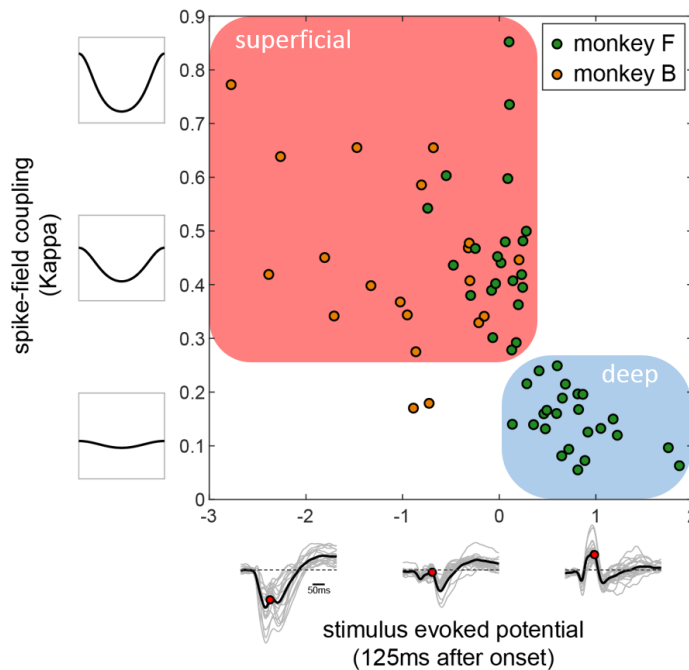


**Figure 4.1: V4 recording site layer classification.**

For each trial set, the visual evoked potential (VEP) and the spike-field coupling were computed. For the VEP, the point in time 125ms following the onset of the visual stimulus was used to determine the magnitude of the positive/negative deviation, as indicated on the horizontal axis insets. For the spike-field coupling, the spread of the circular distribution was assessed by computing Kappa, shown on the vertical axis insets. In order to separate recordings from the superficial and deep layers, a threshold was applied to each metric. Trial sets with VEP deflection less than 0.35 (z-score normalized LFP), and with a Kappa value larger than 0.26 indicate a superficial recording. This classification leaves 24 trial sets for monkey F that we classify as recorded in the deep layers of V4.

field coupling was computed by tabulating mean spiking activity for each LFP gamma phase, resulting in a von Mises distribution indicating the level of coupling between the two signals. Then, for each trial set, we computed Kappa,  $K$ , which corresponds to the spread of a circular von Mises distribution ( $1/K$  is analogous to the variance of a Gaussian distribution). Large values of Kappa indicate a high level of gamma-phase specificity, whereas  $K = 0$  indicates a flat distribution with no phase-coupling present between the spiking activity and the LFP (see the insets along the vertical axis in Fig. 4.1).

The VEP polarity and the gamma-band spike-field coupling metrics reveal a correlation. Higher values of Kappa correspond to a larger negative deflection of the VEP, indicating a superficial layer recording. Conversely, low levels of Kappa correspond to a positive deflection of the VEP, indicating a deep layer recording. The correlation between the VEP polarity and spike-field coupling Kappa provides some confidence that these two measurements are appropriate to identify whether the recording site is in the deep or superficial layer.

For monkey F, 24 of 46 trial sets were classified as being recorded in the deep layer of V4. Having this substantial amount of data allows us to perform a pilot study analysis, with just one monkey, to see how the stimulus information content is modulated by the gamma rhythm in the deep layers of V4.

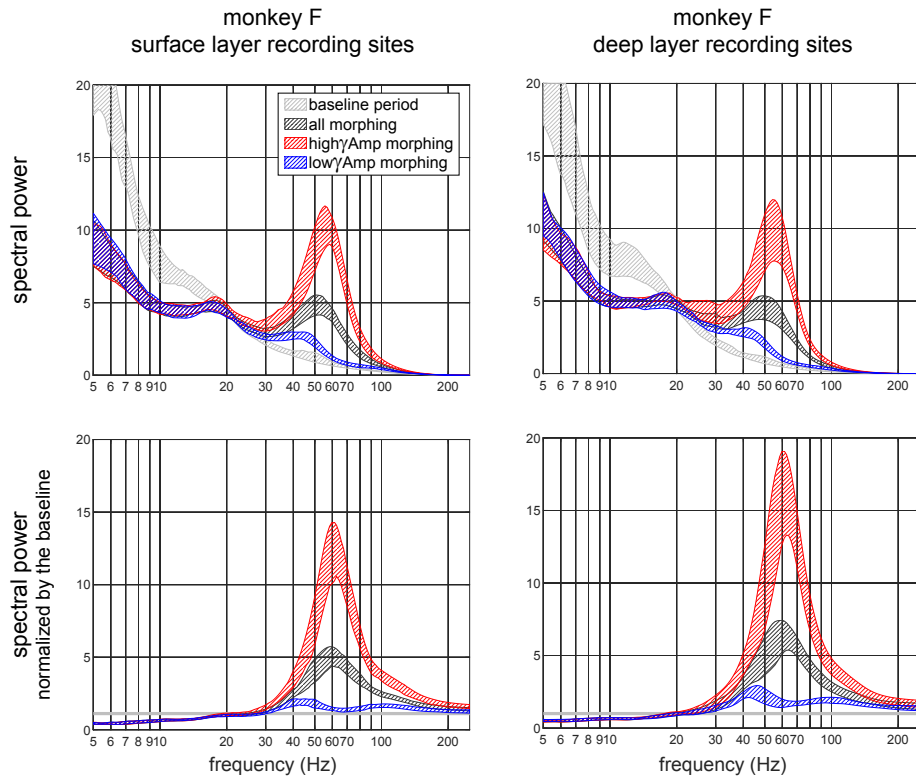


**Figure 4.2: V4 superficial/deep layer spectral power.**

In each plot, the top and bottom of each colored region correspond to the 25th and 75th percentile of spectral power of all the sessions. The plots in the top row show the raw spectral power, for the baseline (in light gray) and the morphing periods (dark gray) of stimulus presentation. For the morphing period, there are additional plots for the high (in red) and the low (in blue) gamma amplitude periods. The two plots in the bottom row show the spectral power normalized by the baseline.

Curiously, the amount of energy in the beta and gamma bands does not appear to be very different between the superficial and deep recordings (see figure 4.2). Further, since the recordings in the deep layers either have very weak or entirely lack spike-phase coupling in the gamma range, it is not possible to reliably assess a proxy for excitability, as we did in the previous chapter. Thus, for the following analyses, we evaluate the phase modulation relative to LFP gamma phase, as opposed to the ESA-aligned phase in the previous chapter. Aside for this, and also aside for the laminar location of the recording sites, all the methodology and analyses are identical to ones utilized in the previous chapter (see figures 3.2 and 3.3).

#### 4.2.2 Deep layer: information modulation by phase

In this section, we evaluate how much of the luminance flicker is present with the phase-specific components of V4's deep layer neural activity. Since we are using LFP phase instead of the ESA-aligned gamma phase, it is important to remind the reader that in the superficial layers, the highest level of spiking activity corresponded roughly to LFP's trough. Thus, for the deep layer results presented here, we keep the LFP's trough phase in the center of the plots, to make the results comparable (see the dotted lines representing the LFP phase in figures 3.4A and 4.3A).

As figure 4.3 shows, LFP neural activity does show significant levels of modulation by phase. Specifically, for the cumulative analysis, where we combine all the available data into one computation, there is substantially more information at the peak as opposed to the trough of the LFP neural activity (Fig. 4.3A,  $p < 0.00005$ ). The individual trial sets corroborate this result, with significantly more sets below the diagonal in the scatter plots of figure 4.3B ( $p = 0.0017$ ).

This result is the *opposite* of the one in the superficial layers (see figure 3.4), where a similarly large modulation was present, but in the opposite direction. A possible explanation for this effect would be that the LFP's gamma rhythm flips polarity between the superficial and deep layers, as shown in the laminar profile of V4's gamma oscillations presented by Kerkoerle et al., 2014 [225].

For the non-attended signal, the cumulative analysis reveals that the SIC is significantly higher at LFP trough than at the peak. As with all the previous non-attended condition results, this effect is rather low in amplitude, however it is still highly significant ( $p = 0.0028$ ). Thus, the attended and non-attended SIC are modulated into *opposite* directions, which was not the case for the superficial layer results. While it is important to keep in mind that the non-attended effect magnitude is low, trusting its validity leads to some interesting functional interpretations. First, this result supports the idea that the upstream V1 populations processing the attended and non-attended signals establish coherence with opposite phase-locking with the recorded V4 population as we originally hypothesized. If we modify V4's gain of its inputs to be lower than presented in the toy model shown in figure 3.1, it would be possible for the modulation of the non-attended signal to go through unimpeded, which would give the result of having opposite polarities of phase-modulation between the attended and non-attended signals. In other words, this result provides support that the deep layers of V4 do not exhibit gamma-rhythmic gain modulation as strongly as the superficial layers.

Crucially, none of the ESA results show a significant difference between the peaks and the troughs. In fact, the SIC values are very low, to the point of not showing any significant information content for many phases. Further, if we pay specific attention to the modulation across the entire phase axis, we do observe slightly higher SIC specifically

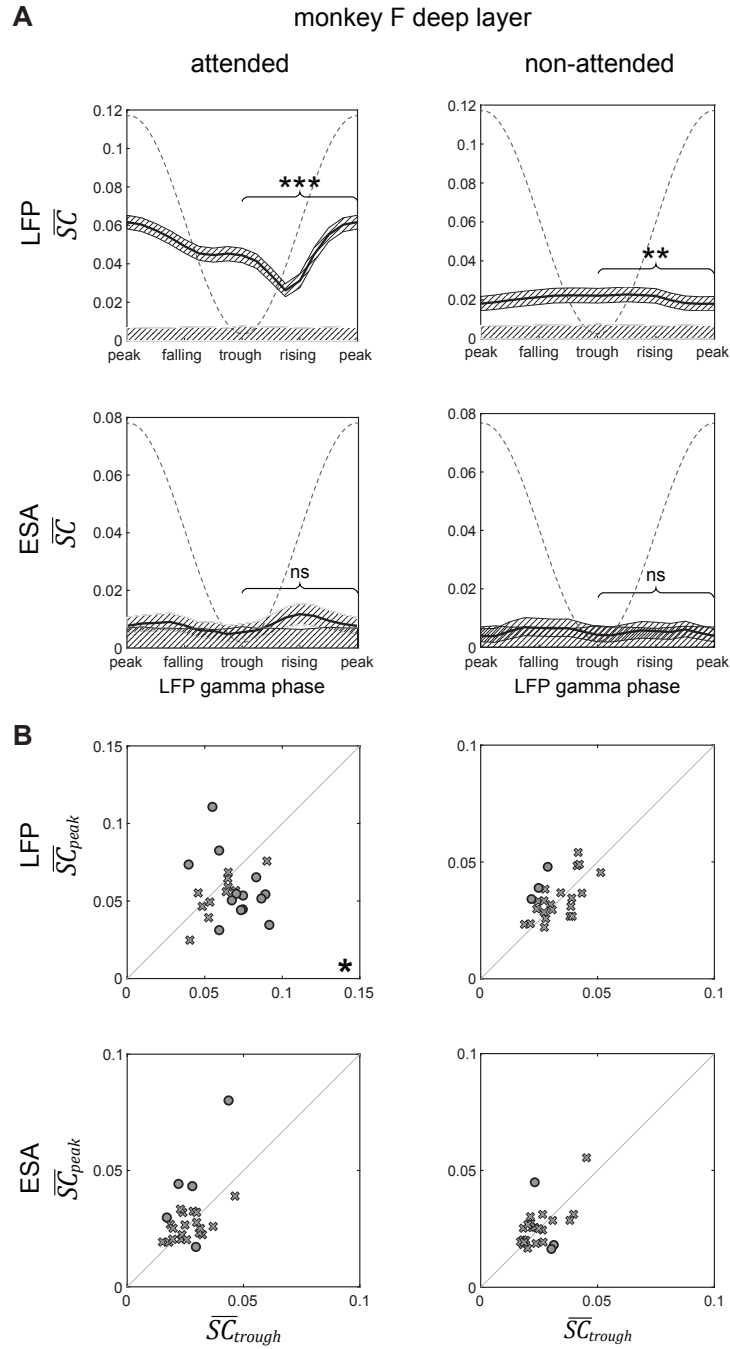


**Figure 4.3: Signal information content modulation by gamma phase, V4 deep layer recording sites.**

**A.** SIC modulation by phase for data pooled across all sessions. In each plot, we display how  $\overline{SC}$  is modulated by the LFP gamma phase (horizontal axis with LFP's trough in the middle) from which the neural signal is extracted. The shading around each line corresponds to the 95% confidence interval. Significance of the difference between  $\overline{SC}_{peak}$  vs  $\overline{SC}_{trough}$  is indicated in each plot (\* $p < 0.05$ , \*\* $p < 0.01$ , \*\*\* $p < 0.001$ , see methods for details). The gray shading at the bottom of each plot corresponds to the 95% chance level (values below this level indicate no significant SIC). The grey dashed sinusoid line indicates the corresponding average LFP phase.

**B.** SIC at peaks versus troughs for individual sessions. For each condition, we display a scatter plot of  $\overline{SC}_{peak}$  vs  $\overline{SC}_{trough}$  pairs. In the scatter plots, individual sets that exhibit a significant difference ( $p < 0.05$ ) are marked with a circle, and with a cross otherwise. The significance of the group distribution, i.e. whether it lies significantly below or above the diagonal, is marked with black asterisks on the side that contains significantly more sessions (\* $p < 0.05$ , \*\* $p < 0.01$ , \*\*\* $p < 0.001$ , see methods for details).

at LFP's rising phase. Curiously, this specific phase location corresponds to the lowest level of SIC for LFP activity (compare the two plots on the left of figure 4.3).

The analysis on the deep layer recordings reveals a difference between the LFP and ESA neural signals. In contrast, for the superficial layer recordings, the results from the ESA and the LFP neural signals consistently corroborated each other, showing qualitatively similar modulations. This provides for the opportunity to compare the nature of the two different neural signals. With ESA, the spiking signal is supposed to represent the output activity of a small amount of neurons in the vicinity of the electrode. In contrast, the LFP reflects the sum of the synaptic currents in a larger area around the electrode. Theoretical studies have typically supported that the LFP signal is actually dominated by the afferent input currents to the local neurons as opposed to their output spiking activity [94, 173, 178, 252]. However, due to several factors, such as recurrent connectivity, assessing the precise nature of the pre and post-synaptic components of the LFP signal becomes convoluted [38, 147].

Before we make any further inferences, we should first scrutinize the effects of gamma amplitude, followed up with how the phase modulation changes between periods of high versus periods of low levels of gamma activity.

#### 4.2.3 *Deep layer: information modulation by amplitude*

In this subsection, we evaluate how much of the luminance flicker is present within periods of low versus periods of high levels of gamma activity in V4 deep layer recordings.

As figure 4.4A shows, when performing the cumulative analysis, combining the trials from all the recordings sites into one computation, there are *no* significant differences between SIC within periods of low versus high levels of gamma activity.

The scatter plots in figure 4.4B display the results for the individual trials sets. Here, we do find a significant difference between SIC in high and low-amplitude periods for two of the conditions, however, the level of significance is low ( $p = 0.032$  for attended LFP and  $p = 0.042$  for the non-attended ESA).

Altogether, the analysis suggests that the SIC does not seem to depend too strongly on the level of local gamma activity. This deviates from superficial site results presented in the previous chapter. The superficial recordings revealed that the amount of attended SIC consistently decreased at lower amplitude levels.

Since the level of information coding does not seem to strongly depend on the amplitude of the local gamma activity, one can speculate that in the deep layers V4's gamma cycle does not modulate the gain of its inputs. If this is the case, SIC modulation by phase that we observed in the previous section may explicitly reflect the phase specificity of the input to the recorded population of neurons.

On the other hand, the magnitude of the effect was already quite small in the superficial recordings, which could mean that in the deep layer recordings the effect could be simply too small to be detected.

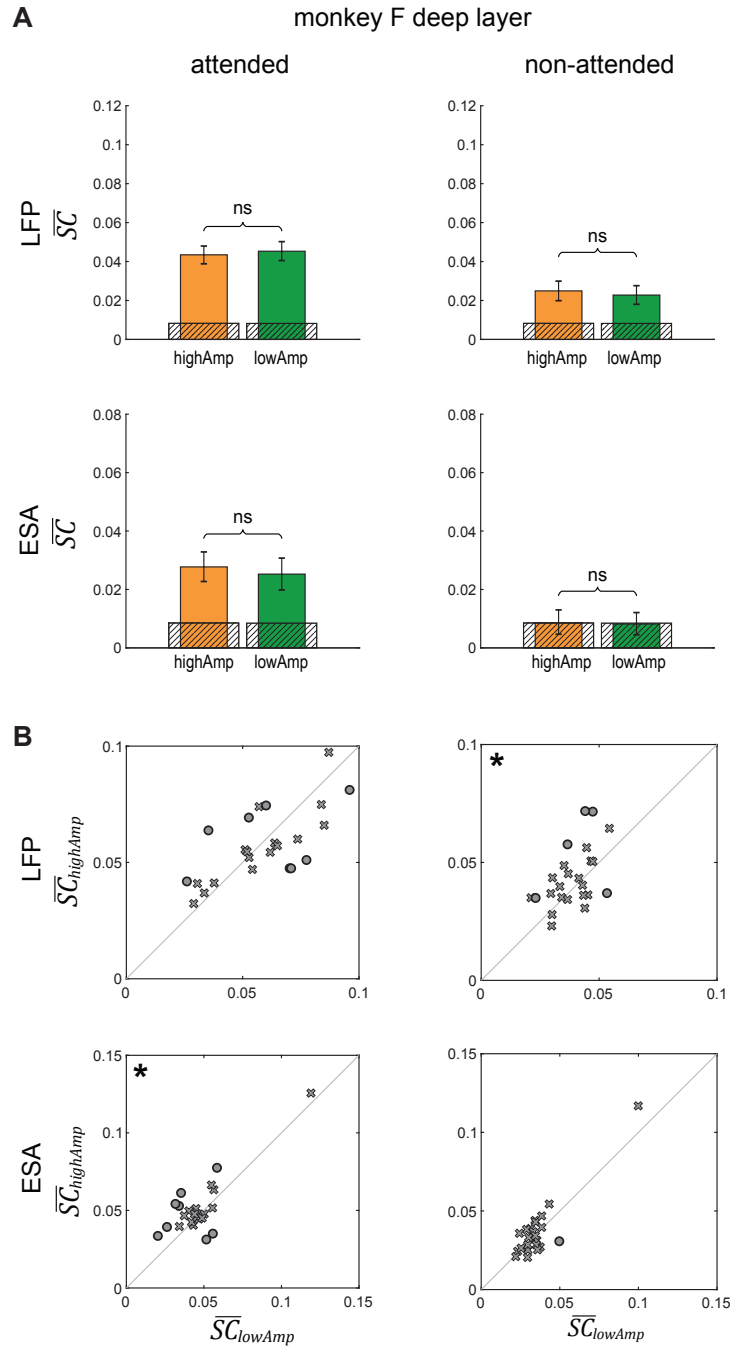


**Figure 4.4: Signal information content modulation by gamma amplitude for deep layer recording sites.**

**A.** SIC extracted from periods with high- versus low-amplitude gamma oscillations for data pooled across all sessions. In each plot, for the specific condition as indicated by the row and column labels, we display pairs of  $\overline{SC}_{highAmp}$  (in orange) and  $\overline{SC}_{lowAmp}$  (in green), separately for each animal, neural data type, and attention condition. The error bars indicate the 95% confidence interval. The gray shading at the bottom of each bar indicates the 95% chance level for that value. Significance level of the differences is indicated above each pair of bars, acquired by permutation testing across the trials ( $*p < 0.05$ ,  $**p < 0.01$ ,  $***p < 0.001$ , see methods for details).

**B.** SIC extracted from periods of high versus low gamma neural activity for individual sessions. For each condition, we display a scatter plot of  $\overline{SC}_{highAmp}$  vs  $\overline{SC}_{lowAmp}$  pairs. In the scatter plots, sessions that exhibit a significant difference ( $p < 0.05$ ) are marked with a circle, and with a cross otherwise. The significance of the group distribution, whether it lies significantly below or above the diagonal, is marked with black asterisks on the side that contains significantly more sessions ( $*p < 0.05$ ,  $**p < 0.01$ ,  $***p < 0.001$ , see methods for details).

#### 4.2.4 Deep layer: information modulation by phase and amplitude

In this section, we combine the neural activity dissociation by gamma phase together with the dissociation by gamma amplitude, allowing to assess how the modulation by phase changes with the level of gamma activity.

The results of the cumulative analysis are displayed in figure 4.5. Here, for the high-amplitude condition, we find that the attended-stimulus information content within the LFP signal shows a significant increase at both the peak and trough gamma phases, but not during the rising or the falling phases of the neural activity. The effect magnitude is particularly high for LFP's trough, producing a bimodal shape for modulation by phase.

In the previous chapter, the effects observed for the analysis combining gamma phase and amplitude neural signal dissection (figure 3.7) were under critique, due to the diminished phase-modulation in the low amplitude condition potentially being explained away by simply having less reliable phase estimates when the gamma activity was low. In the deep layer, rather than observing a similar increase (or decrease) in phase-specific modulation during periods of high (or low) gamma activity, the modulation shows a substantial qualitative difference, going from a mono-polar distribution with highest values for the LFP-peak towards a bi-polar distribution with highest values at both the peak and the trough.

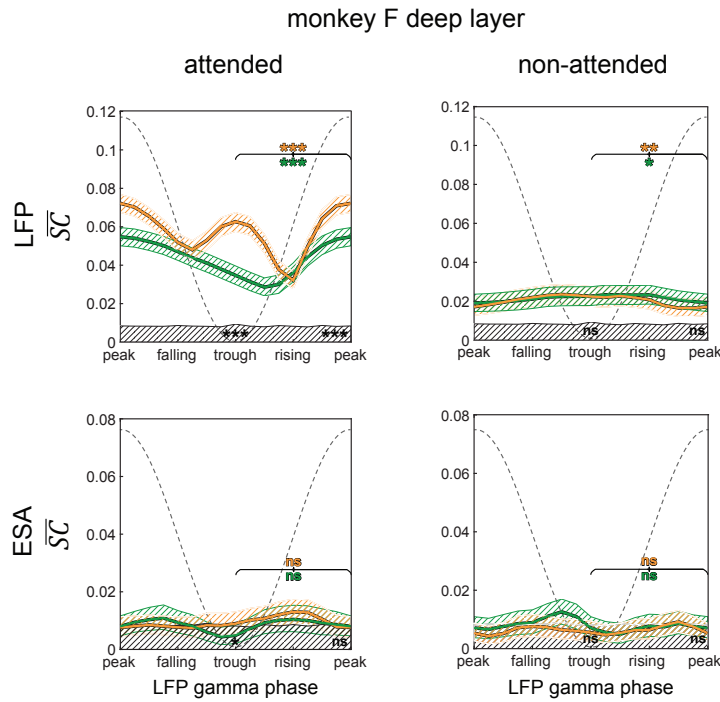


**Figure 4.5: Signal information content during high gamma amplitude and low gamma amplitude periods in dependence on V4's gamma phase for the deep layer recording sites.**

For each condition, as indicated by the row and column labels, each plot displays how SIC is modulated by phase of signal extraction (horizontal axis), separately for high gamma amplitudes (in orange) and low gamma amplitudes (in green) conditions. The shading around each line corresponds to the 95% confidence interval. The grey shading at the bottom of each plot shows the corresponding 95% chance level. The grey dashed sinusoid line indicates the corresponding average LFP phase. The asterisks towards the bottom of each plot indicate whether there is a significant difference between  $\overline{SC}_{highAmp}$  and  $\overline{SC}_{lowAmp}$  for the corresponding phase. The colored asterisks at the top right of each plot indicated whether there is a significant difference between  $\overline{SC}_{peak}$  and  $\overline{SC}_{trough}$  for the corresponding amplitude condition.

One possible explanation for this effect could be attributed to the method utilized in order to extract the phase-specific neural activity components. There is an inherent level of noise within the signal, which leads to a margin of error when we compute the gamma phase. Since the neural activity experiences fast changes during the rising and falling phases, the inaccuracy in determining the gamma phase may result in highly inaccurate samples of the neural activity at the phase-specific time-points. This would result in a particularly noisy phase-specific signal when extracting the phase-specific components for the phases corresponding to the rising and falling of the neural activity, diminishing the amount of measured SIC within it. Conversely, the samples extracted from the peaks and the troughs of the gamma-rhythmic neural activity are much more stable against time shifts, leading to a cleaner peak and trough phase-specific signal components. Cumulatively, when performing the analysis, SIC estimation is most accurate at peaks and troughs. Due to this effect, all the phase-specific analyses throughout the research project focused on comparing SIC values for the two phase values. The effect of SIC getting biased towards the peaks and troughs of the neural signal could potentially result in a bipolar phase modulation, as seen the top left plot of figure 4.5.

However, if the above effect is substantial, why don't we observe similar bipolar shape of modulation in the other conditions? It is quite possible that there is indeed an additional mechanism at play that could explain the modulation shape. One possible explanation is that we are observing a mixture of two phase-modulation effects, one with the highest SIC at the peak and one with the highest SIC at the trough. With such a mixture, the phase-modulation component with highest SIC at the trough of LFP appears to be more susceptible to strength of the local gamma oscillation than the phase-modulation component with highest SIC at the peak of LFP. One possible way to have to a mixture of two effects could arise through recurrent connectivity within the deep layer population. In this scenario, the original gamma-rhythmic bursts of input might arrive at the LFP peaks. This input would evoke output activity within the local neurons, that would in turn feed back into the same population with a delay such that the recurrent input arrives at the LFP troughs. This recurrent delayed connectivity mechanism can essentially replicate the input neural signal across other phases.

It is important to note that the above explanation is speculative. The presented results are just from one animal, which makes it dubious to draw inferences towards what the effects would be like on a population level. Nonetheless, the clear qualitative difference between the superficial and deep layer recordings still provides strong support that these layers are participating in different roles. The pilot study results invite further investigation. Having more animals and more recording sessions would further elucidate the difference and the functional roles of the computations performed within the different layers of V4's cortical columns.



## 5.1 INTRODUCTION

In the previous two chapters, we performed analyses on how stimulus information content (SIC) encoded within V4 neural activity is dependent on V4's gamma phase and amplitude. Prior to the analyses we were able to put forth a set of predictions, based on the routing-by-synchronization (RBS) mechanism. Cumulatively, our results were able to confirm the predictions, essentially recreating the bottom subplot of figure 3.1B and thus providing strong support for the RBS framework. However, the prediction of how SIC is contained within V4's activity is only a part of the whole picture. In the proposed hypothesis, V4 plays the role of the receiver population, getting inputs from two sender population in V1, one sending information of the attended stimulus and one sending information of the non-attended stimulus. Crucially, the hypothesis relies on a set of assumptions with strong support from existing literature about the SIC phase-coding within V1 output activity and the coherence in the gamma-rhythms between V1 and V4, providing us with the top subplot of figure 3.1B, expanded here in figure 5.1.

One of the prerequisites for the RBS mechanism is that each V1 population exhibits its own gamma-rhythmic activity with stimulus information content modulated by its gamma phase. The assumption is that SIC within V1's output activity should depend on V1's gamma-phase, with higher amount of information at the excitability peaks of the rhythmic activity, i.e. when the population releases its gamma-rhythmic bursts of spikes. In support of this, *Womelsdorf et al. 2012* [249] found that V1 spikes occurring at the excitability peak do exhibit higher stimulus orientation selectivity. In our hypothesis about how RBS is implemented in the early visual system, the amplitude of the gamma oscillations in V1, as well as the phase-dependent coding of the stimulus information is not dependent on whether or not the stimulus with V1's receptive field is attended — we assume equal strength of SIC modulation by phase within V1's activity (Fig.5.1).

The other component of RBS is that the gamma-rhythmic activity of V1 processing the attended stimulus establishes a strong coherence with V4's gamma-rhythmic activity with proper phase-locking such that V1's bursts of activity arrive to V4 when it's most excitable. V1 processing the non-attended stimulus either does not establish coherence with V4 at all, or establishes much weaker coherence with phase-locking that would have the non-attended stimulus arrive in bursts to V4 when it's not excitable. This should result in having the attended stimulus information enter V4 consistently at its peaks, while having the non-attended stimulus information get spread across the different phases of V4's activity. The coherence between V1 and V4 populations is the primary component of RBS, with strong support from existing studies [29, 98]. Curiously, *Bosman et al. 2012* [29] found that the non-attended V1 established no coherence at all with V4, whereas *Grothe et al. 2012* [98] found that non-attended V1 did establish weak coherence with V4. Notably, the phase-relationship of the coherence has not been directly reported on.

Cumulatively, the phase-dependence of stimulus information in V1 together with the V1-V4 coherence results in having the attended signal consistently enter V4 at its excitability peaks, whereas the non-attended stimulus information enters V4 spread across

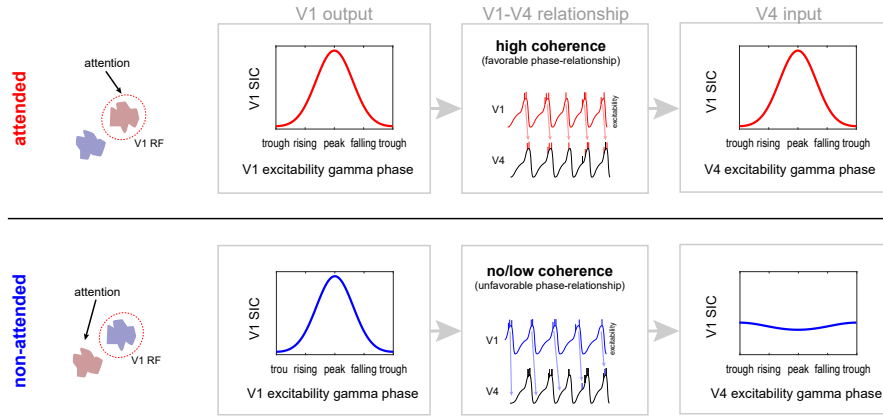


**Figure 5.1: Phase-dependent V1 SIC at the V1 output stage and at the V4 input stage.**

Regardless whether the location of V1's RF is attended or not, SIC within V1's output is highest at the V1 excitability peak. When attended, V1 establishes a strong coherence with V4 at a favorable phase-locking, such that its output arrives to V4 during its excitability peaks. When not attended, V1 establishes no or low level of coherence with V4 at an unfavorable phase locking, such that non-attended information is spread across the different phases of V4 excitability.

the different phases. This phase-dependent input information content is represented in the last column of plots in figure 5.1. In the present chapter, we utilize a limited data set of V1 activity collected together with the V4 data that was the focus of analyses in the previous two chapters. As such, the experimental setup, involving an attention task with two morphing shapes (see figure 3.2) as well as the methods, involving extraction of phase-specific neural activity (see figure 3.3) are presented in detail in part 3.2 of this dissertation. The aim of the following analyses is to essentially recreate the pieces in figure 5.1, revisiting previous findings and existing assumptions about attended and non-attended stimulus information coding in V1 as well as the phase-relationship between V1 and V4.

## 5.2 RESULTS AND DISCUSSION

### 5.2.1 V1 data, laminar location of recordings

When the data for the experiment was collected, the previously-existing V1 array of monkey B had degraded to the extent that no useful recordings in this visual area could be performed. A chronic electrode array implanted in monkey F's V1 was still delivering reasonable data across 8 recording sessions. From a grid of 96 tungsten electrodes with 2mm spacing, the RFs of 15 sites contained one of the two shape stimuli. However, the electrode array was inserted relatively deeply into the cortical tissue to prevent accidental removal during sudden head movements of the animal. The location of electrodes in the deep layers is a problem when the goal is to characterize information transmission from V1 to downstream areas, due to existing evidence that feedforward information transfer occurs from the superficial layers of the cortex [15, 34, 145, 158, 225].

In order to attempt to characterize the laminar location of the V1 recording sites, we assessed the average visually evoked potential (VEP) of the recordings — the average of the LFP signals across all the trials following the initial appearance of the shape stimulus with the V1's RF (Fig. 5.2). For each session, we separated the trials by the attended condition, whether the shape within the V1's RF was attended or non-attended.

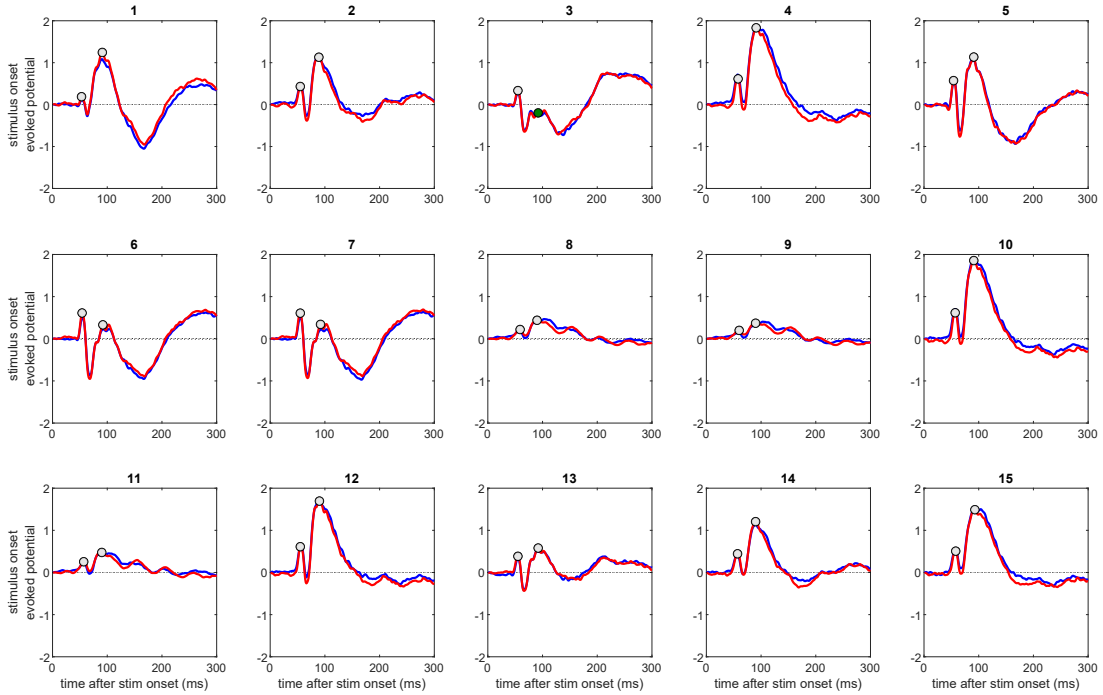


**Figure 5.2: V1 visually evoked potentials.**

The average LFP following stimulus onset. VEP collected from trials with V1’s RF attended are in red, non-attended in blue. Points of interest at 50ms and 100ms are marked in each plot. Recording site 3 is the only one with a prolonged negative deflection following 50ms.

The results show that the shape of the VEPs does not reveal a difference depending on whether the location of the V1’s RF was attended or not. The shape of the VEP is known to depend on laminar location of the recording. Specifically for V1, *Shroeder et al. 1998* [197] found that for the superficial layers, the VEP begins with a negative deviation around 50ms, and a positive fluctuation for the deep layers. However, the 1998 experiment utilized bright flashes covering the entire visual space, which is quite different from presenting a small stimulus specifically within the RF of the recorded V1 population. The V1 VEPs we find in our experimental setup are quite similar in shape to the VEPs for the V4 population. A similar shape for V4 VEPs has been reported in *Nandy et al. 2017* [168], who also utilized a high contrast stimulus placed within the RF.

Cumulatively, without additional evidence (such as the level spike-LFP coherence in the gamma range utilized in the previous chapter) we are unable to confidently identify the laminar location of our V1 recordings. We observe a number of shapes among the V1 VEPs for our dataset. In particular, recording site 3 is notable for being the only one whose VEP goes and stays negative after 50ms. Following the same procedure as the one utilized for V4 data, this would be the only electrode to qualify as potentially being in the superficial layers. Although we are uncertain about the laminar nature of the recordings, and only limited to recordings from one animal, we still perform the analyses as a pilot study on how stimulus information coding depends on V1’s local rhythm, and how this changes after accounting for V1-V4 coherence.

### 5.2.2 V1 information modulation by phase

Here, we follow a similar procedure as we did when assessing phase-modulation of SIC within V4’s activity in section 3.3.1. We extract the gamma phase from the V1 LFP signal

for each trial. Then we select a subset of points from the LFP activity corresponding to a specific gamma phase, where the LFP trough should roughly correspond to excitability peak and LFP peak should roughly correspond to excitability trough (note that we cannot confirm this since there is no corresponding spiking signal). This allows us to compute spectral coherence between the phase-specific neural signal and the stimulus flicker signal. The spectral coherence is then pooled across the relevant time and 5-15Hz frequency bins in order to obtain the final measure of stimulus information content specific to each phase:  $\overline{SC}_\phi$ .

Since we have 15 recording sites with chronically implanted electrodes, staying in the same location across the 8 recording sessions, the results are pooled across the sessions, while keeping the recording locations separate. The results reveal that there is indeed SIC modulation by phase within V1. Foremost, we observe that attention does not play a major role in the overall levels of SIC. We do observe slightly higher levels for the non-attended signal which confirms the corresponding finding from Grothe et al. 2018 [99] where 7 of 15 sites showed significantly higher SC in the non-attended case. Cumulatively, this indicates that attentional gating of information does not appear to occur at the level of V1.

For each recording site, attended and non-attended SIC follow a similar phase modulation. Some recording sites exhibit substantially higher signal information at LFP troughs, as expected, however, the opposite pattern with highest signal information content at LFP peaks is also present. Recording sites 1, 6 and 7 exhibit a particularly strong SIC modulation by phase, but the highest values of  $\overline{SC}$  are found at LFP peaks, which should correspond to excitability troughs. This reversal could be due to the reversal of LFP polarity in the deeper layers. The plot for recording site 3, which is the only one we could identify as potentially located in superficial layer, shows the expected curves: attended and non-attended SIC curves are nearly identical and both showcase higher  $\overline{SC}$  values at LFP trough.

### 5.2.3 Attentional modulation of V1-V4 coherence

In order to assess the level of phase-coupling between V1 and V4, we compute frequency-resolved spectrograms of the neural signals  $W(f, t)_{V1}$  and  $W(f, t)_{V4}$  via a Morlet wavelet transform (for details see section 3.2). These values are used to compute the coherence between V1 and V4, utilizing the same spectral coherence formula that was previously used to assess the amount of flicker information within a neural signal:

$$C_{V1V4}(f, \tau) = \frac{\left| \sum_{p,t} \tilde{W}_{V4}(f, t) \cdot W_{V1}(f, t + \tau) \right|^2}{\left( \sum_{p,t} |W_{V4}(f, t)|^2 \right) \left( \sum_{p,t} |W_{V1}(f, t + \tau)|^2 \right)}$$

where  $\tilde{W}_{V4}$  is the complex conjugate of  $W_{V4}$ ,  $\tau$  is the lag between the two signals, and the sums are performed over all the timepoints  $t$  from the morphing period of the trials, combining all valid pairings  $p$  of V1 and V4 recordings from the same session.

This measure essentially tells us the strength of coherence at each frequency for different lags between V1 and V4. Figure 5.4A and B show coherence for electrode 3. Instead of focusing on the low frequency component, as we do in order to assess SIC within the neural signal, now we focus on the high levels of coherence present in the gamma range. The plots reveal that the attended condition  $C_{V1_{attn}V4}$  exhibits substantially higher levels of coherence than the non-attended  $C_{V1_{non}V4}$ , showing maximum coherence at a

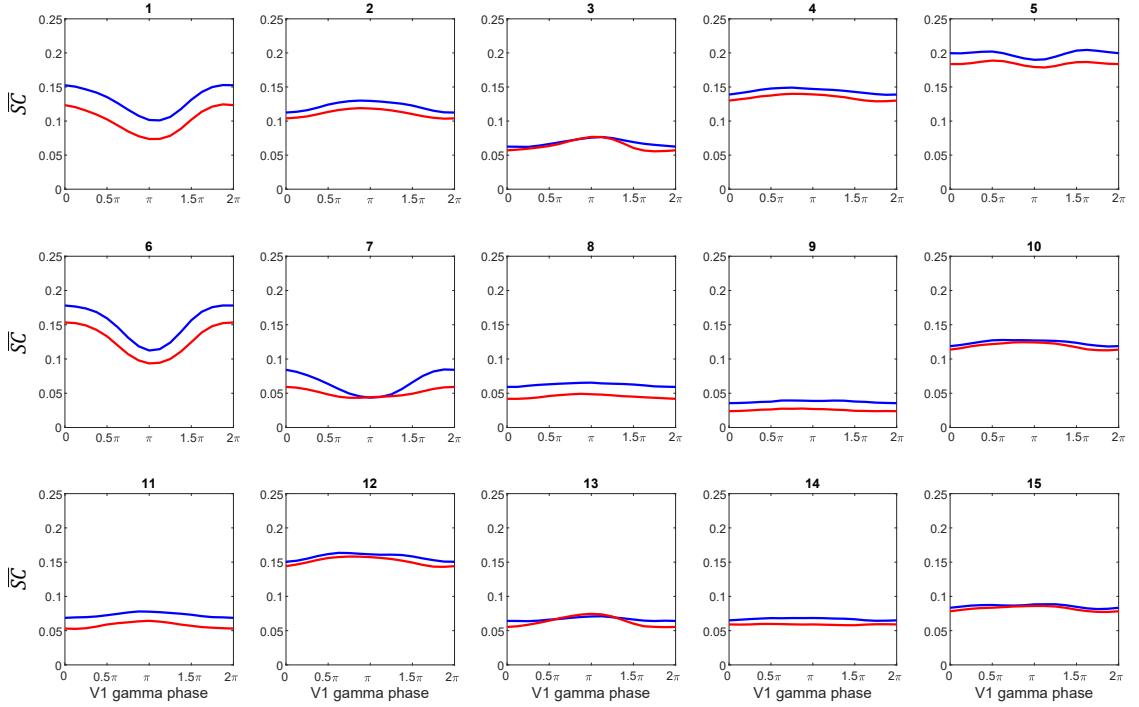


**Figure 5.3: Phase-specific stimulus information content within V1 LFP activity.**

SIC dependence on phase for V1 data pooled across all recording sessions, separately for each recording site. The horizontal axis is labeled in terms of V1’s LFP phase, where phase 0 should roughly correspond to excitability trough, and phase  $\pi$  should correspond to excitability peak. In each plot, we display how  $\overline{SIC}$  depends on the LFP gamma phase (horizontal axis) from which the neural signal is extracted, in red for when the stimulus within V1’s RF was attended, in blue for non-attended.

8ms temporal shift between the signals. We use this maximum coherence value  $\overline{C}$  in order to summarize the coherence levels between V1 and V4 for each recording site in figure 5.4D. V1 recording site 3, in particular, showcased highest levels of coherence with V4. Ultimately, the results reproduce the findings from *Grothe et al 2012* [98]: V1 populations processing the attended stimulus establish strong coherence with V4 in the gamma range, meanwhile V1 populations processing non-attended stimulus establish much lower levels of coherence, roughly a fifth when compared to the attended. The delay at which we observe maximum coherence  $\delta\tau = 8\text{ms}$  serves as a very rough estimate of synaptic delay between V1 and V4.

We can also assess the phase of coherence between the signals  $\Theta_{V1V4}$  by taking the angle of the complex valued spectral density in the numerator of the previous equation:

$$\Theta_{V1V4}(f, \tau) = \angle \left( \sum_{p,t} \tilde{W}_{V4}(f, t) \cdot W_{V1}(f, t + \tau) \right)$$

The values of  $\Theta_{V1V4}(f, \tau)$  give us the phase relationship between the signals at which they achieve maximum coherence.  $\overline{\Theta}$  is the phase value corresponding to the location of the maximum coherence  $\overline{C}$  from plot A. This value gives us a very rough estimate of the phase difference between V1 and V4 signals, shown in figure 5.4E. For the attended condition  $\overline{\Theta}_{V1_{attn}V4}$ , these values mostly fall slightly below 0, indicating that V1 activity peaks are synchronized with the pre-peak rising phase of V4 activity. For the non-attended condition, these values primarily fall above 0, indicating that the small

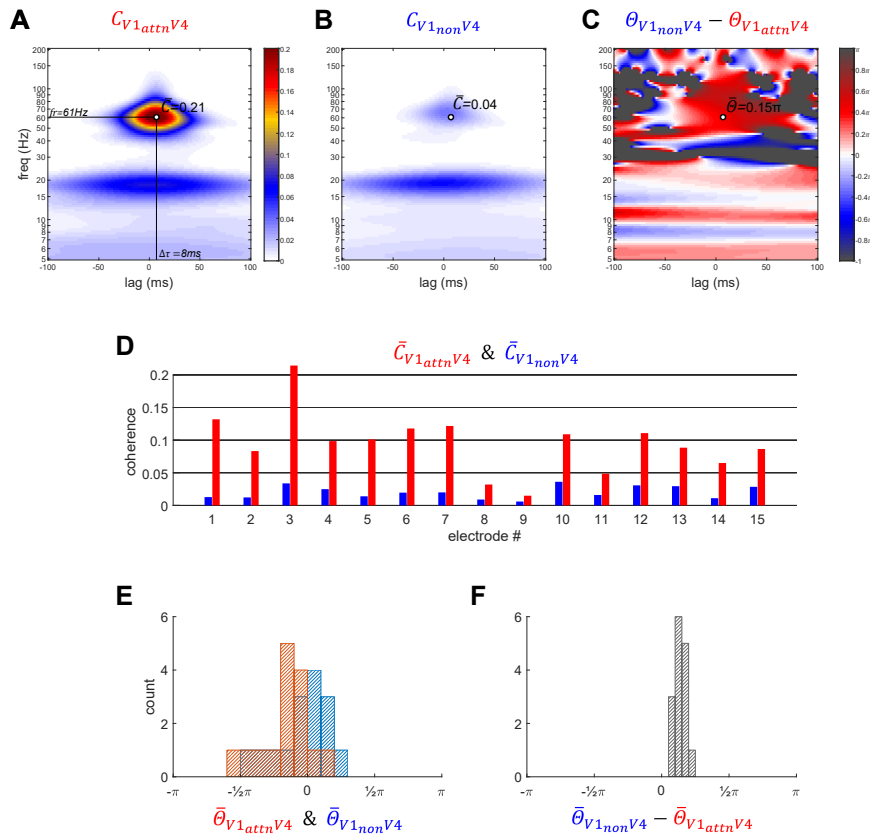


**Figure 5.4: V1-V4 coherence magnitude and angle.**

**A** and **B**. Coherence between V1 and V4 activity for V1 electrode 3. Data is separated by attention and pooled across all the available pairings of LFP signals between V1 and corresponding superficial V4 electrodes for each session, across all the sessions (a total of 12 sets of paired trials). For the attended condition in **A**, the maximum coherence value,  $\bar{C}_{V1attnV4}$  is marked, along with its corresponding frequency and a rough estimate of the delay  $\tau$  of 8ms between V1 and V4. The same position is labeled for the non-attended condition in **B**.

**C**. Each value in the coherence magnitude plots has a corresponding phase-locking value  $\Theta_{V1V4}$ . The difference between the attended  $\Theta_{V1attnV4}$  and non-attended  $\Theta_{V1nonV4}$  conditions reveals that there is a consistent difference between the two conditions in the area of high gamma coherence. The value at the point of maximal coherence is marked,  $\bar{\Theta}_{V1attnV4}$ .

**D**. The maximum coherence,  $\bar{C}_{V1V4}$  marked in **A** and **B**, for each electrode. Attended condition corresponds to consistently higher values of  $\bar{C}_{V1V4}$  than non-attended; non-attended coherence value is not zero.

**E**. The distribution of phase-locking values,  $\bar{\Theta}_{V1attnV4}$  and  $\bar{\Theta}_{V1nonV4}$  at the corresponding delay  $\tau$  across the recording sites. When attended (in red), on average V1 gamma is slightly behind V4, with V1's peaks corresponding to the rising phase of V4. When non-attended (in blue), V1 gamma is slightly ahead of V4, with V1's peaks of activity corresponding to the falling phase of V4.

**F**. The difference between the attended and non-attended phase-locking value,  $\bar{\Theta}_{V1attnV4} - \bar{\Theta}_{V1nonV4}$  for each electrode. The non-attended phase-locking to V4 is consistently delayed by around  $0.2\pi$  compared to the corresponding attended condition.

amount of coherence that does occur between non-attended V1 and V4 has the peaks of V1 align with the post-peak falling phase of V4 activity, with the value shifting drastically across the lag axis.

The difference between the non-attended and attended phase-locking values (figure 5.4C) reveals a region around the proper lag and frequency with a consistent value. Across all the recording sites (figure 5.4E), this value is always positive, indicating that when the V1 population is processing the attended signal, it's bursts of activity arrive to V4 slightly earlier than when it is non-attended. Cumulatively, the phase-locking results nicely corroborate the idea that the gamma-rhythmic activity of the V1 population pro-

cessing an attended signal entrains V4, the non-attended rhythmic bursts of V1 activity enter V4 shortly afterwards, when the window of high excitability in V4 has passed, natural frequency of attended V1 is higher than natural frequency of receiving V4 [29]. When coupled, the two rhythms become phase-locked, with V1 attended entraining the V4 rhythm [79].

#### 5.2.4 V1 information modulation relative to V4 gamma

In this section we assess how SIC within V1 is distributed in relation to V4's gamma activity. This should correlate to how input information to V4 is distributed across the phases of its gamma rhythm, whereas the previous analyses with phase-specific signals in relation to V1's gamma activity indicate phase-modulation as it exits V1.

First, we extract phase-specific signals from V1, utilizing the same procedure from the previous two chapters (see figure 3.3), except instead of using a V1 population's own gamma phase to select the phase-specific time points within its neural activity, we substitute the gamma information from a concurrent recording from a superficial V4 electrode. The analysis is performed separately for each V1 site, separated by the attended condition and pooled across the possible V4 match-ups across the 8 recording sessions. In order to properly align V1 and V4 signals for the phase-specific signal extraction, we need to account for the synaptic delay between the two populations. For this we use the  $\delta\tau$  value, acquired from the coherence analysis between the V1 and V4 activities in the previous section. This value stayed mostly consistent for all the electrodes, 7-9ms. Thus, prior to extracting the V4-phase-specific V1 signals, we shift V1 activity forward by  $\delta\tau$ .

By combining V1 and V4 data, taking V4's gamma phase values and using them to assess the phase-specific information within V1, the results reflect the gamma-phase coupling between V1 and V4. In figure 5.3, we observed that information is indeed concentrated around particular phases of V1's activity, in relation to its own gamma phase. In relation to V4's gamma phase, low levels of coherence between V1 and V4 should "smear" V1 information across different phases of V4's activity, decreasing the level of phase-modulation (bottom row of figure 5.1). High levels of coherence should result in keeping existing levels of information phase-modulation (top row of figure 5.1).

Figure 5.5A-D shows the multiple steps involved in the processing of stimulus information for two sample recording sites. The top row, A, shows how information of attended and non-attended signals is modulated by phase within V1's activity, with both sites exhibiting SIC modulation by phase, but at opposite polarities. Row B shows the corresponding levels of coherence in the gamma range between V1 and V4 populations, when V1 is attended the coherence is substantially higher. Finally, row C below that shows how much SIC is present within V1 activity relative to V4's gamma phase. Here, we can immediately observe that any SIC phase-modulation of non-attended signals is removed, resulting in flat curves. Meanwhile, for the attended condition, SIC phase-modulation is retained. Finally, we also include SIC modulation by phase of V4's LFP signal, from chapter 3.3.1. Together, these plots allow us to track how stimulus information is coded by phase as it goes through the steps of the RBS mechanism: row A shows SIC within V1's output, row B describes the level of coherence between V1 and V4, row C shows SIC within V4's input, and finally row D shows SIC within V4's output activity.

Figure 5.5E and F summarize how stimulus information coding changes between V1 output and V4 input stages across the 15 available V1 recording sites. The starting point of each vector shows peak versus trough  $\overline{SC}$  values relative to V1's gamma phase and

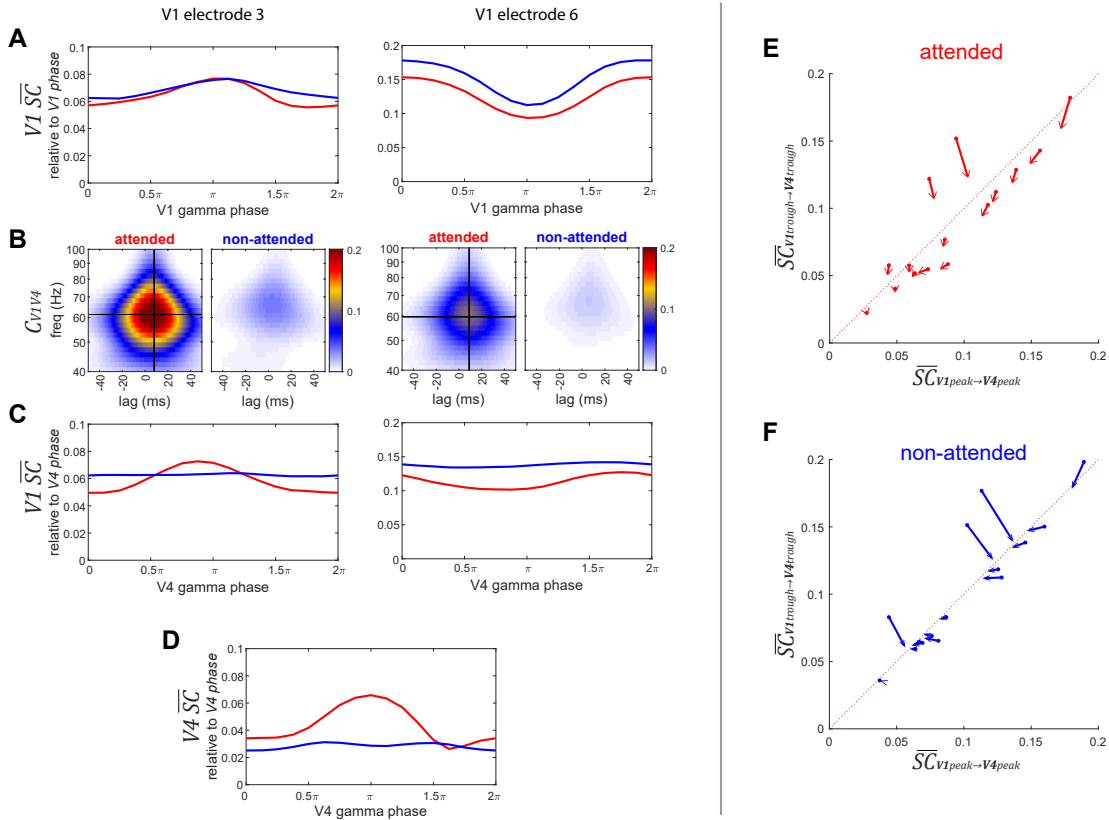


**Figure 5: Stimulus information content phase-modulation, going from V1 output to V4 input.**

**A.** SIC within V1 activity, showing modulation relative to V1's gamma phase for two V1 recording sites. Red curve indicates SIC modulation for attended signal, blue for non-attended. These curves correspond to the amount of stimulus information present within V1 output activity.

**B.** Corresponding V1-V4 coherence plots.

**C.** SIC within V1 activity, showing modulation relative to concurrent V4 gamma phase. These curves correspond to the amount of stimulus information as it enters V4 relative to V4's gamma rhythm.

**D.** SIC within V4 activity, relative to its own gamma phase. This is the same data as shown in figure 3.4C. These curves correspond to amount of stimulus information in the output of V4.

**E.** Change in phase-modulation of information content within neural activity between the V1 output stage and the V4 input stage for the attended condition. The x-axis indicates the amount of information at excitability peak and the y-axis corresponds to excitability trough (going from V1 output to V4 input).

**F.** Same as E, for the non-attended condition.

the arrowhead of each vector corresponds to peak versus trough  $\overline{SC}$  in relation to V4's gamma phase. Data below the diagonal corresponds to recordings with more information present around the excitability peaks and data above the diagonal corresponds to neural activity with more information around excitability troughs. Data points on the diagonal itself indicate that there is no SIC modulation by phase. Across the 15 recording sites, the non-attended condition data shows that information is modulated by phase as it exits V1, and then the phase-modulation vanishes as it enters V4, with all arrows pointing at the diagonal. This is not at all the case for the attended condition, with the data showing that if there was SIC modulation-by-phase at the V1 output stage, it remains there as it entered V4.

It is important to remember that we only had the opportunity to analyze V1 data from just one animal, only the LFP signal, and without much confidence about the laminar locations of the recording sites. In theory, deep layers are predominantly responsible for feedback processing, where V4 would play the role of the sender population and V1

the receiver. However, the layers within a cortical column are interconnected, thus our analyses might merely reflect an "echo" of feedforward gamma-rhythmic information processing from the superficial layers, convoluted within the deeper layers. If there had been more V1 data, with spikes, from multiple animals, confidently from the superficial layers of V1, it is quite likely that the one would observe much stronger effects, higher levels of SIC phase-modulation with considerably more information content at V1's excitability peaks.

Altogether, the pilot study shows additional support for the RBS mechanism. We have found that level of stimulus information present within neural activity is indeed modulated by the gamma rhythm of V1 populations, sending out rhythmic bursts of information packages for both attended and non-attended signals. V1 populations processing attended stimuli exhibit strong coherence with V4, consistently delivering stimulus information to the same phase of V4's rhythmic activity. V1 populations processing non-attended stimuli exhibit much weaker coherence with V4, delivering stimulus information across all phases of V4's rhythmic activity, diminishing the existing phase-modulation of information content present within V1. The small amounts of coherence between the non-attended V1 and attended V4 seems to occur at a slightly delayed phase when compared to the attended condition, delivering gamma-rhythmic packages to V4 after it has passed its excitability peak. Finally, V4's gamma-rhythmic gain of its inputs further enhances the difference in the gamma-dependent SIC modulation between attended and non-attended inputs to V4, allowing for its output activity to contain predominately the attended stimulus information.



Part III

STIMULATION SIMULATION



## CONTROLLING GAMMA-RHYTHMIC COHERENCE WITH MICROSTIMULATION

---

Electrical stimulation is a promising tool for interacting with neuronal dynamics to identify neural mechanisms that underlie cognitive function. Since effects of a single short stimulation pulse typically vary greatly and depend on the current network state, many experimental paradigms have rather resorted to continuous or periodic stimulation in order to establish and maintain a desired effect. However, such an approach explicitly leads to forced and ‘unnatural’ brain activity. Further, continuous stimulation can make it hard to parse the recorded activity and separate neural signal from stimulation artifacts. In this study we propose an alternate strategy: by monitoring a system in realtime, we use the existing preferred states or attractors of the network and to apply short and precise pulses in order to switch between its preferred states. When pushed into one of its attractors, one can use the natural tendency of the system to remain in such a state to prolong the effect of a stimulation pulse, opening a larger window of opportunity to observe the consequences on cognitive processing. To elaborate on this idea, we consider flexible information routing in the visual cortex as a prototypical example. When processing a stimulus, neural populations in the visual cortex have been found to engage in synchronized gamma activity. In this context, selective signal routing is achieved by changing the relative phase between oscillatory activity in sending and receiving populations (communication through coherence, CTC). In order to explore how perturbations interact with CTC, we investigate a network of interneuronal gamma (ING) oscillators composed of integrate-and-fire neurons exhibiting similar synchronization and signal routing phenomena. We develop a closed-loop stimulation paradigm based on the phase-response characteristics of the network and demonstrate its ability to establish desired synchronization states. By measuring information content throughout the model, we evaluate the effect of signal contamination caused by the stimulation in relation to the magnitude of the injected pulses and intrinsic noise in the system. Finally, we demonstrate that, up to a critical noise level, precisely timed perturbations can be used to artificially induce the effect of attention by selectively routing visual signals to higher cortical areas.

### 6.1 INTRODUCTION

With evolving technology, new and promising techniques to interfere with the brain’s natural activity have played a crucial role in moving from correlational to causal links between neuronal activity and behavior [71, 138, 214]. Crucially, the same techniques are used clinically to treat pathological injuries and disorders [19, 21, 73, 146]. The development of perturbation technology, among many others, includes ablations of cortical and subcortical targets, chemical lesions, reversible inactivations, transcranial direction current stimulation (tDCS), transcranial magnetic stimulation (TMS), intracortical microstimulation (ICMS), and finally the fairly recent and exciting optogenetic techniques [253]. This advancement of tools has provided increasingly higher temporal and spatial perturbation precision, allowing for more intricate control over neural activity, which in

turn has supported progressively stronger conclusions about the neuronal mechanisms underlying cognition.

While non-invasive techniques such as tDCS and TMS ease clinical applicability, the effects of their stimulation unfortunately lack spatial precision. Invasive techniques, in particular, ICMS and optogenetics allow for precise temporal and spatial resolution, providing the ability to deliver a single short and temporally precise perturbation at a precise location in the brain, which in turn, should greatly increase the ability to accurately affect and control neural circuits. However, the effect of such a single short perturbation can be very short-lived and, crucially, it can vary greatly in dependence on the state of the neural system at the pulse onset. Because of this, many perturbation paradigms have opted to either use a very strong pulse, essentially resetting and disrupting the activity of the target network, or to use a continuous or repetitive-pulse stimulation in order to establish and maintain a desired effect. For instance, a series of seminal studies [46, 201] entrained a local population in the barrel cortex of mice with a rhythmic optogenetic train of pulses at 40 Hz. By delivering a vibrissa stimulation at different phases of the entrained population's cyclic activity, the researchers showed that the neural population's response as well as the rodent's behavioral performance depends on the phase at which the whisker stimulation stimulus arrives to the population. In a more recent study, [172] used a similar technique to show how an optogenetically induced neural rhythm modulates the gain of spike responses and behavioral reaction times in response to visual stimuli in cats.

Using continuous stimulation serves its role as a powerful research tool, however it also brings up a number of concerns. First, in some cases, stimulation can effectively destroy and suppress any ongoing local processing [138]. Even if it does not lead to full suppression, in addition to achieving a desired effect, continuous stimulation may interfere and contaminate the relevant neural signals. Further, in many cases, when analyzing the activity recorded during the stimulation, it becomes hard, if not unfeasible, to separate the stimulation artifacts from the relevant neural data. Finally, such an approach explicitly forces the neural system to remain in some desired network state, resulting in artificial dynamics and making it questionable what we learn about processing during natural activity.

In this study, we propose to use an alternate strategy. Rather than using continuous stimulation in order to sustain a desired state of the neural network, we wish to utilize a single precise pulse in order to push the system into one of its (potentially) existing preferred states [221]. If the network is pushed into one of its attractors, the natural tendency of the system to remain in such a state extends the duration of the effect of the pulse, which opens up a larger window of opportunity to observe the consequences on cognitive processing. Crucially, it becomes necessary to monitor the system in real time in order to be aware of the system's state and to deliver just the right stimulation at just the right time, resulting in a closed-loop paradigm.

Approaching the brain's rhythmic activity and synchronization phenomena from a perspective of non-linear dynamics provides useful inferences on neural oscillator activity [100]. First, oscillatory synchronization collapses the normally high dimensional dynamics of neural dynamics into a low dimensional set of attractor states. Further, if a neural system can be modeled using self-sustained, oscillators, a perturbation inserted at a specific phase of a cycle would evoke a consistent phase-shift in the oscillator's activity – an effect that is captured by a phase-response-curve (PRC) [42, 198]. Numerous experimental studies have found evidence for PRCs in vitro [5] and as well as in vivo [229, 230, 237].

In the present study, through a modeling approach, we develop a method to explore the feasibility of utilizing PRCs in order to shift the synchronization of a system into a desired state. First, we choose to model selective information routing in the visual cortex, between V1 and V4 cortical areas. A prominent mechanism explaining how information routing occurs, communication through coherence (CTC), relies on the inherent oscillatory dynamics of neural activity and postulates that neural populations establish favorable and unfavorable information routing states through frequency-specific phase-locking [77, 79]. In support of this hypothesis, experimental studies have shown strong evidence for gamma-band synchronization between sending V1 and receiving V4 neural populations during a visual attention task [29, 98]. Once a favorable synchronization state is established, rhythmic bursts of V1 spikes arrive to V4 during its excitability peaks, increasing the likelihood that further spikes are evoked leading to effective signal routing. On the other hand, if the V1 and V4 populations establish an unfavorable phase state relationship, the V1 spikes arrive to V4 during the excitability troughs and hence should fail or at least be less effective in evoking further activity.

We begin with a model of an isolated neural oscillator and then expand to more realistic system of multiple coupled populations, constructed to exhibit the synchronization and information routing phenomena observed in the visual cortex. We explicitly measure the information content in the model to evaluate the effect of signal contamination caused by the stimulation in relation to the magnitude of the injected pulses and intrinsic noise level of the system. Further, we vary the background noise level to investigate how increased stochasticity affects the phase-response properties the system and hence our ability to control it. We demonstrate that up to a critical noise level, precisely timed perturbations can be used to ‘simulate’ the effect of attention by selectively routing a visual signal to higher cortical areas and identify optimal pulse strengths required to achieve this goal.

## 6.2 RESULTS

In the first part of this section, we present the model of a local cortical population as the basic building block of our framework. Further, we introduce the techniques needed to monitor oscillatory dynamics, and demonstrate how to use them to control single oscillators to maintain a desired system state. Taken together, these considerations pave the way for interacting with a more realistic, hierarchical cortical network in Part 2 of this section.

### 6.2.1 Part 1: Stimulating a single population

#### 6.2.1.1 Network model

*Model structure and dynamics.*

For representing a local population of neurons, we construct a recurrent network with 800 excitatory and 200 inhibitory, conduction-based quadratic integrate-and-fire neurons. Their membrane potentials  $V$  evolve according to the differential equation

$$C_m \dot{V} = p_2 V^2 + p_1 V + p_0 + g_e(V - V_e) + g_i(V - V_i) + \sigma_n \eta(t). \quad (6.1)$$

Here,  $C_m$  is the membrane capacitance,  $V_e$  and  $V_i$  are the reversal potentials and  $g_e$  and  $g_i$  the corresponding conductances for excitatory and inhibitory input currents, and  $\eta(t)$  is  $1/f$  (pink) noise with magnitude  $\sigma_n$ . If the membrane potential  $V$  crosses the threshold

$V_{thresh}$ , a spike is generated and delivered to all connected neurons, and  $V$  is reset to  $V_{rest}$ .

Synaptic term equations and all the relevant parameter values are presented in table 6.1 in the Methods section. Connections exist from the inhibitory population to itself, with projection probability  $p_{ii}^{loc} = 0.5$  and corresponding delay  $\tau_{ii}^{loc} = 5$  ms, and from the inhibitory to the excitatory populations, with projection probability  $p_{ie}^{loc} = 0.5$  and corresponding delay  $\tau_{ie}^{loc} = 5$  ms (Fig. 6.1A). The high probability of connectivity from the inhibitory neurons reflects the dense connectivity of the inhibitory interneurons found in the cortex [175]. The neuron and coupling parameters are set to emulate realistic neurons, in accordance with [12] (for details on the implementation and parameters see Methods section). In our case, having 5ms delays allows the network to generate gamma frequency oscillations (Fig. 6.1C) by means of an ING-mechanism [217].

Both populations are driven by afferent connections delivering excitatory input with time-varying rates  $S_e(t)$  and  $S_i(t)$ , realized by inhomogeneous Poisson processes. We scaled the mean rate and driving magnitude of the afferent input such that we achieve a relatively high firing rate of 60 Hz for the inhibitory units, and significantly lower for the excitatory units at 15 Hz, reflecting the typical differences found between the firing rates of the neuron types in the cortex [232].

#### *Quantifying stimulus representation.*

When interacting with a cortical network by external electric stimulation, we pursue two goals: Assessing the implied changes in dynamical network states, and quantifying the impact on function, i.e. the representation and processing of visual information. For the latter goal, we adopt a method which was used successfully to quantify selective signal transmission ('gating') in dependence on the attentional state [99, 102]. The main idea of this method is to modulate the visual (input) signal by a random change in its amplitude ('flicker'), and to compare the output of a neural population with the input flicker signal by computing a frequency-resolved correlation using spectral coherence (SC). In our case, we modulated the external drive with mean rate  $S_x^0$ ,  $x \in \{e, i\}$  by a flicker signal  $F_x$  via

$$S_x(t) = S_x^0(1 + \sigma_F F_x(t)). \quad (6.2)$$

$F_x$  was sampled from a uniform distribution between  $[-1, 1]$ , changing every 10ms, corresponding to the experimental flicker signals used in [99] where a luminance of a stimulus changed every frame at 100 frames per second. The strength of flicker modulation was set to  $\sigma_F = 0.10$ . This modulation is passed onto the spiking rates of the driven neural populations (Fig. 6.1A). Note that even though the background  $1/f$  noise  $\eta(t)$  and the flicker modulation  $F_x(t)$  appear to have similar effects on the model, the flicker changes at a much lower rate and its magnitude is kept consistent throughout all the simulations, whereas the magnitude of background noise  $\eta(t)$  is used to change the noise level of the system. By design, the flicker is the signal we track throughout the network, and  $\eta(t)$  constitutes intrinsic, interfering noise that affects the cleanliness of oscillations and overall stability of network states.

To assess the input flicker modulation contribution to the neural activity, we utilize spectral coherence (SC). This method allows the investigate the linear contribution of the input to network's activity and was successfully used experimentally to study similar selective processing in [99]. In our study, it provides a simple proxy to evaluate how well we can control the system and the level of signal degradation due to perturbations. This does not exclude that stimuli information is also encoded in other ways such as popu-

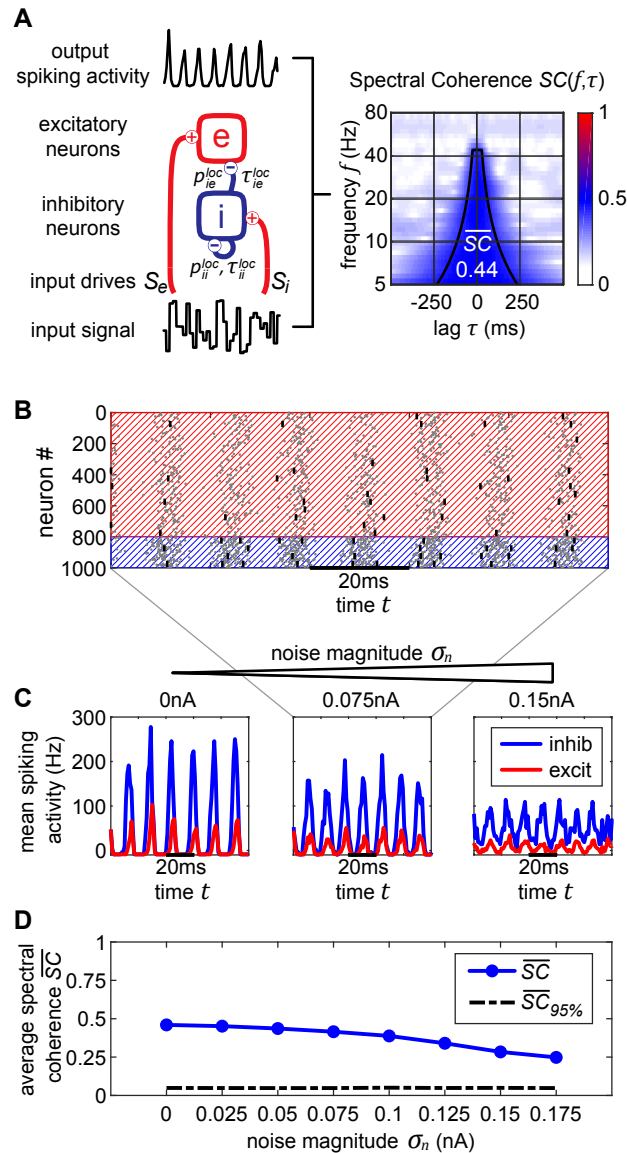


**Figure 6.1: Single oscillator model and activity**

**A.** A local population consists of an excitatory and an inhibitory neuron subpopulations. It is driven by an input signal containing a time-varying amplitude modulation. The inhibitory population projects onto itself and onto the excitatory neurons, resulting in an ING mechanism which produces cyclic population activity in the gamma frequency range (60-75Hz). To evaluate the signal routing ability of the network, we assess the spectral coherence  $SC(f, \tau)$  between the input signal modulation and the excitatory output activity for different frequencies  $f$  and signal time lags  $\tau$ . A cumulative input signal information measure  $\overline{SC}$  (white text) is computed by pooling across the relevant time-frequency range within the cone of interest (solid black lines).

**B.** A raster plot of the all spiking activity withing the system for the medium amount of background noise  $\sigma_n = 0.075\text{nA}$ . Neurons 1-800 are excitatory (red shading) and 801-1000 are inhibitory. 1 in 50 neurons is marked by a small black bar, in order to highlight the spiking activity of a few individual neurons.

**C.** Samples of excitatory and inhibitory population activity for increasing internal noise levels are displayed for multiple background noise conditions. At zero noise, oscillatory spiking activity is very regular - large population bursts are followed by periods of silence. With increasing noise, activity gets more irregular and less phase specific.

**D.** We show how input signal modulation contribution to the neural activity  $\overline{SC}$  decreases with increasing internal noise  $\sigma_n$ . The dashed line at the bottom indicates the 95% chance level, calculated by pairing up the network activity with surrogate input signals.

lation or temporal coding, but suffices to compare the effects of ‘simulated’ attention by ICMS to ‘physiological’ attention.

First, we compute the spectrograms of the input signal and the spike output using a wavelet transform with Morlet kernels. The transform yields complex valued coefficients  $W_z(f, t)$  representing the amplitude and phase of a signal  $z(t)$  around the frequency band  $f$  at time  $t$ . By evaluating the normalized cross-correlation between the spectrograms of  $x(t)$  and  $y(t)$  we obtain the spectral coherence measure  $C_{xy}(f, \tau)$ , where  $f$  is the frequency and  $\tau$  is the delay between the two signals:

$$C_{xy}(f, \tau) = \frac{\sum_i W_x^*(f, t_i) \cdot W_y(f, t_i + \tau)}{\sum_i |W_x(f, t_i)| \cdot \sum_i |W_y(f, t_i + \tau)|}, \quad (6.3)$$

Due to the normalization terms in the denominator, the values of  $C_{xy}$  lie between zero and one.

If neurons are driven well by the external stimulus, experimental data [99] and model simulations (Fig.6.1A) reveal that the input signal can be tracked in the population activity of a local population in V1 (or V4) up to frequencies of about 45 Hz (or 25 Hz). Hence, in order to obtain a cumulative measure of input signal contribution to the neural activity, we defined a cone-of-interest whose upper frequency limit was selected to be at 45 Hz, and whose temporal range was defined as  $\pm 7/6f$  around  $\tau = \tau_{xy}$ , where  $\tau_{xy}$  is the delay between input signal  $x$  and neural output  $y$ . We pooled across the relevant frequencies  $f$  and time lags  $\tau$  within the cone of interest, to compute a single spectral coherence score  $\overline{SC}_{xy}$ .

#### *Gamma oscillations and noise.*

In a typical experimental situation, it is impossible to assess the output signal of a specific neural population directly. Instead, the measurement is confounded by both, measurement noise and noise induced by background activity or by contributions from neighboring circuits. For interacting with the brain, it is therefore essential to quantify the impact of noise on the assessment of the current system state and to determine limits up to which successful control is still possible. We therefore introduced internal noise via the additional term  $\sigma_n \eta(t)$  in equation 6.1 [75].  $\eta(t)$  is  $1/f$  noise with standard deviation equal to 1, making  $\sigma_n$  represent the magnitude of the noise. Every single neuron unit receives its own unique noise input. By changing the magnitude  $\sigma_n$ , we control the overall level of noise in the entire system.

In Fig. 6.1C in the top three plots, we display model activity at different noise levels. With zero noise level we clearly see oscillations within the Gamma frequency range, with low jitter and high regularity and phase specificity – inhibitory and excitatory populations of neurons both evoke concentrated bursts of spikes followed by periods of silence. Increasing the noise renders oscillations more irregular and less phase-specific, and decreases peak amplitudes. Also, oscillation frequency increases from 60 Hz for the zero noise condition to 75 Hz for 0.15 nA. In order to maintain a stable cyclic activity with a constant frequency, the ratio of inhibitory and excitatory post-synaptic currents needs to stay consistent within each population of neurons [41]. Increasing the magnitude of noise inherently raises the firing rate of neurons. Since our units are recurrently coupled, a change in average firing rate upsets the inhibition-excitation ratio of the system, which results in a dramatic change in activity. To counteract this effect, for each noise level, we update the magnitude of driving rates  $S_e$  and  $S_i$  to provide just the right amount of input drive to excitatory and inhibitory units to maintain firing rates consistent with

physiological evidence, i.e. an average of 15 Hz for excitatory and 60 Hz for inhibitory units (parameters see Methods section).

For noise levels of about 0.1 nA, we observe signals similar to physiological findings [99]. To cover a realistic range, we investigated noise levels from  $\sigma_n = 0$  nA up to  $\sigma_n = 0.175$  nA. Crucially, as can be expected, the input signal representation as quantified by  $\overline{SC}$  becomes worse with increasing noise, although it stays well above the significance level (Fig. 6.1D).

### 6.2.1.2 Tracking oscillations and stimulation effects

#### *Real-time phase tracking.*

For a targeted interaction with a neural system, we have to assess its internal state in real-time. In our case, the internal state is characterized by the current phase of an ongoing oscillation (in the Gamma frequency range). Consequently, we will have to determine this phase as precisely and timely as possible.

Tracking the phase of a signal in real-time imposes the constraint that only data from the past can be used for phase measurement, whereas the typical offline phase measurement algorithms rely on utilizing past and future data for an accurate estimate of the instantaneous phase at that time point. Hence, we utilize use a phase-extraction scheme motivated by [48] that relies on using autoregression (AR) in order to forecast the signal forwards (Fig. 6.2 top row). The AR model has been found to perform well in forecasting noisy signals with power spectrum limited to certain frequencies [24], making it adequate for our data.

In order to use the AR model, it must first be trained on data without any perturbations. Once the model is acquired, it is used to extend the signal into the future, allows us to use any of the typical offline methods for phase extraction. In our case, we utilize the Hilbert transform. We apply a zero-phase bandpass filter with bandstops at the halfway points found in the power spectrum to obtain the gamma component of the signal without distorting its phase. Then, the data is passed through a Hilbert transform

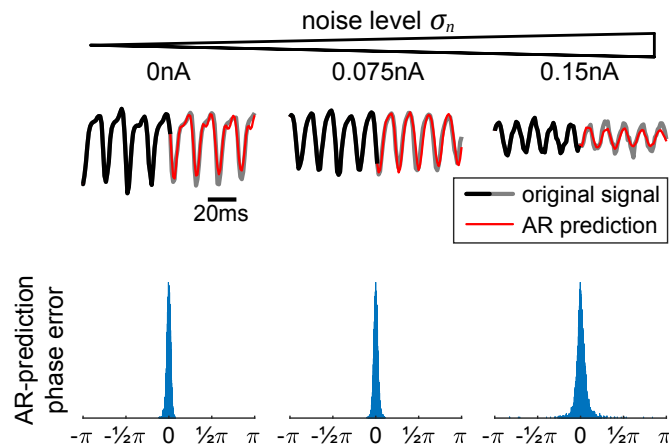


**Figure 6.2: Autoregression (AR) signal prediction and phase error.**

In order to extract real-time phase or the phase of a signal prior to a perturbation, we utilize AR in order to forecast signals into the future before using typical offline methods (Hilbert transform). In the top row, we show a few current signals generated by our model for increasing levels of noise. The black-to-grey line shows the original signal and the red line shows the AR prediction. In the bottom row, we show the corresponding distributions of difference between offline vs real-time phase for multiple predictions, showing the efficacy of the method.

[25], providing us with the complex analytical signal. The argument of the analytical signal reveals the instantaneous gamma phase. The narrow range of the bandpass filter is necessary, since the instantaneous phase only becomes accurate and meaningful if the filter bandwidth is sufficiently narrow [171]. The difference between the realtime and offline phase extraction shows to be sufficiently small, demonstrating the efficacy of the method (Fig. 6.2 bottom row), and obviating the need to revert to more elaborate phase estimation schemes such as using multiple band-pass filters with slightly different filter parameters [164].

In addition to allowing us to extract realtime phase, the same method is also applied to neural signals just prior to an input pulse to determine the phase of the ongoing oscillation before it is affected by the systems response to the perturbation. A similar method relying on AR was utilized specifically for this reason in [172].

#### *Phase-response curves.*

Using stimulation pulses, our goal is ‘push’ a neural system towards particular states and quantify the impact of such a ‘configuration change’ on information processing. For an oscillatory system, when a perturbation occurs at a specific phase of its cyclic activity, the following oscillatory activity is shifted by a consistent amount. This can be quantified by a phase-response-curve (PRC) [42, 198, 205] by tabulating the phase shift  $\Delta\varphi$  induced by a perturbation in dependence on the phase  $\varphi$  at pulse onset (Fig. 6.3A). Conversely, a PRC can be used to determine the ‘right’ time for a stimulation in order to shift the system’s phase by a desired amount.

We simulate electric stimulation by injecting a square pulse of current of 1 ms duration into all the neurons within the oscillator. The pulse was intended to emulate intracortical microstimulation (ICMS), affecting the population of local neurons indiscriminately. We tested depolarizing (positive pulses, exciting the neurons) and hyperpolarizing (negative pulses, inhibiting the neurons) pulse polarities at multiple pulse strengths  $\delta I$ , from 0.25 nA up to 4 nA. To collect the PRC curve data, first, we run the model for a total time  $T$  without any stimulation pulses (Fig. 6.3A, left panel, black curves). Using real-time phase measurement, this data allows us to tabulate normal, unpulsed phase progression  $\varphi(t)$ . For assessing the impact of perturbation on phase, we again run the model for time  $T$ , now pulsing at random points in time, and obtain the pulsed phase progression  $\varphi_{\delta I}(t)$  (Fig. 6.3A, left panel, red curves). The resulting phase shift observed after a delay time  $\tau$  is then given by  $\Delta\varphi(\tau) = \varphi_{\delta I}(t_{onset} + \tau) - \varphi(t_{onset} + \tau)$ . Except for very simple or idealized systems,  $\Delta\varphi$  is typically not independent of  $\tau$ . In particular, one distinguishes between the *immediate* PRC for  $\tau = 0^+$ , and the *permanent* PRC for large  $\tau$  [180].

Since we consider a stochastic dynamical system, one cannot directly obtain a PRC from network simulations. Instead, we repeated the described procedure for sufficiently many  $t_{onset}$ ’s to first obtain a phase-response probability density function  $\rho_{\tau}(\Delta\varphi|\varphi)$  (Fig. 6.3A, right panel, blue shading). By taking the circular mean across  $\Delta\varphi$ , one can condense  $\rho_{\tau}$  into a mean PRC  $\overline{\Delta\varphi}_{\tau}(\varphi)$  (Fig. 6.3A, right panel, red line), whose inverse gives the appropriate onset phase(s)  $\varphi$  which achieve(s) on average a phase shift  $\Delta\varphi$  at time  $\tau$  after giving the pulse.

Note that this inverse mapping does not have to be unique, nor does it have to exist for any desired phase shift, especially for low pulse strengths. In theory, one can realize any desired phase shift by using a sequence of (small) shifts into the right direction, but since we have to cope with a noisy dynamics inducing frequency jitter, we typically aim at achieving a desired shift with as few pulses as possible.

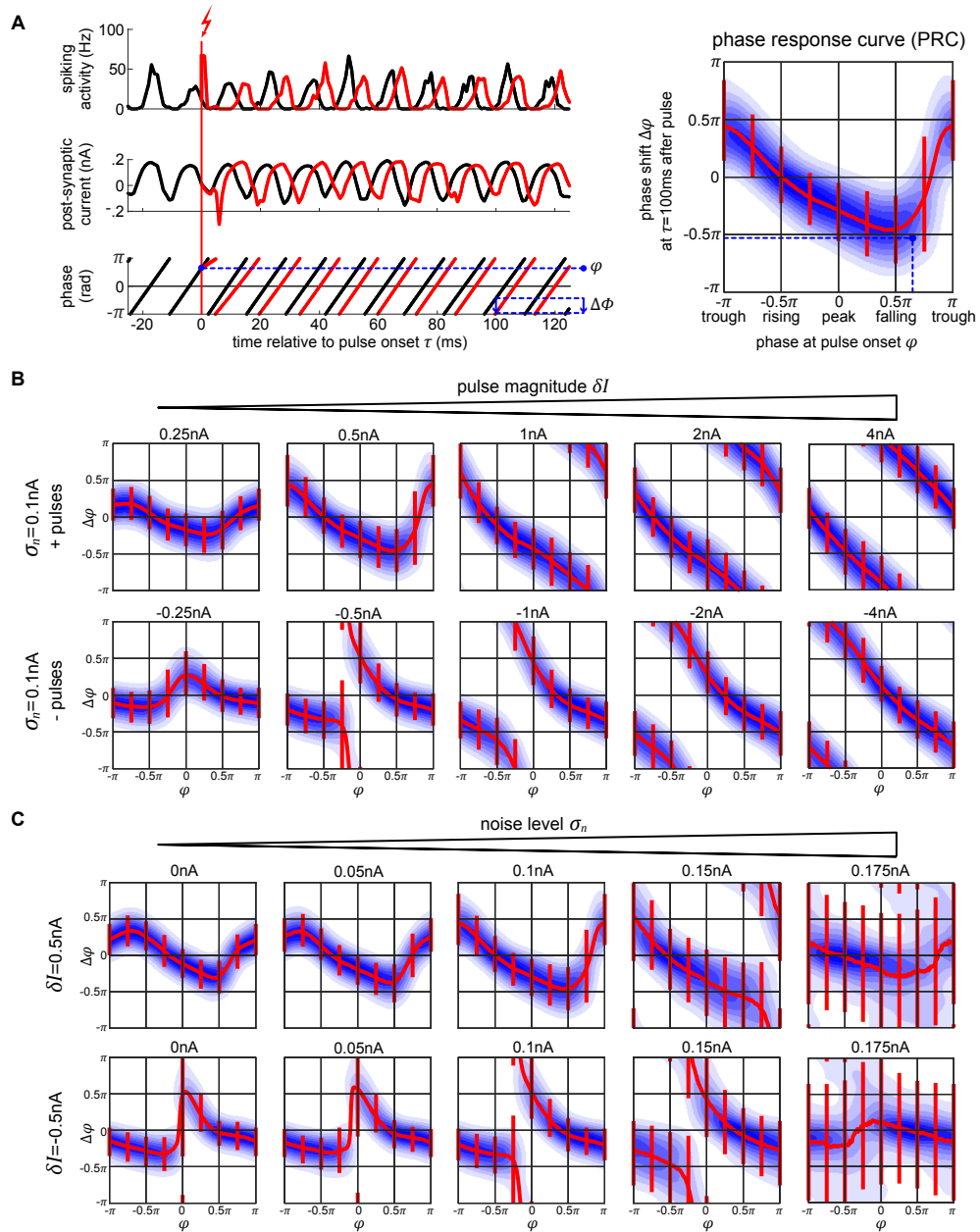


**Figure 6.3: Phase response curves.**

**A.** The plots on the left (top and middle row) show the activity of the excitatory population (in black) and how a single perturbation applied to the oscillator changes both activity and post-synaptic current (in red). From the corresponding phase dynamics (bottom row), we capture the phase  $\phi$  at the pulse onset, and the resulting phase shift  $\delta\phi$  100ms later (blue arrow). This gives us a single data point (marked in black) in the PRC space on the right. By repeating this procedure, we obtain the distribution of pulse responses indicating the PRC and its variability due to internal and external noise sources. The blue shading in the plot corresponds to the probability density of many runs, with darker blue corresponding to higher probability.

**B,C.** We show multiple PRCs across different conditions - varying pulse magnitude (**B**) and internal noise level (**C**). In each plot, the thick red line represents circular mean of the phase shift across the pulse onsets, while the thin red lines indicate the corresponding 25th and 75th percentiles. At low pulse strengths, the resulting PRC shows a smooth biphasic relationship - pulsing at the peak ( $0 < \phi(t_{onset}) < 0.5\pi$ ) results in a negative phase shift (delay) and pulsing at the trough ( $-\pi < \phi(t_{onset}) < -0.5\pi$ ) gives a positive phase shift. As we increase the strength of the perturbation the magnitude of the phase shift increases. At sufficiently high pulse magnitude of either polarity, a perturbation leads to a complete phase reset.

Note that the phase shift  $\Delta\varphi$  does not occur immediately. Rather, following the stimulation, the network takes time to stabilize and settle back into its normal cyclic activity, similar to what has been described as ‘permanent resetting’ in the case of PRCs for individual neurons [180]. In the single oscillator model, it takes around 2-3 cycles (around  $\tau = 30$  ms) for the network to settle into its new stable phase state. Following this time point, the mean phase shift stays consistent, however, the variability goes up, due to the activities’ intrinsic fluctuations in frequency.

For weak perturbations ( $\delta I = 0.25 - 1.0$  nA pulse magnitude), the resulting phase offsets are small, resulting in a smooth biphasic PRC. The negative and positive pulses cause shifts into opposite directions (Fig. 6.3B, compare top and bottom rows of first plots on the left). However, as the strength of the pulse increases, the phase-shifts increase as well, until they look the same and a complete phase reset occurs resulting in a PRC that approaches the shape of a straight line (Fig. 6.3B, plots on the right). With a strong negative/hyperpolarizing pulse, both the excitatory and inhibitory neurons are reset to their steady state and the whole system is silenced, leading to a predictable amount of time that it takes for the network to recover and start oscillating. When a strong positive/depolarizing pulse is delivered, both populations of the network discharge a large volley of spikes, which is then followed by a strong hyperpolarization  $\tau_{ii} = \tau_{ie} = 5$ ms later due to the connections from the inhibitory neurons, which essentially acts as a strong negative pulse onto the system. In each case, the neurons are reset to the steady state, taking the network a predictable amount of time to recover back to its oscillatory activity, regardless of onset phase of the perturbation.

As we increase the internal noise of the model, the variability of the PRC goes up with it. At a sufficiently high noise level,  $\sigma_n \geq 0.175$  nA, we no longer achieve stable or predictable phase shifts (Fig. 6.3C), which means that the oscillator has become too unstable to exhibit phase-response properties [100]. Additionally, when applying a specific magnitude of a pulse, its effect seems to increase (getting closer to a full phase-reset) with noise as well. In part, this is due to the fact that the amplitude of the oscillations in the noisy conditions are lower, meaning that the relative magnitude of the pulse to the oscillations gets higher with increasing noise.

### 6.2.1.3 Controlling oscillations

#### *Phase control procedure.*

To test the ability to use the phase-response characteristics of our model, we employ the following task: we run two independent oscillators, X and Y, simultaneously. If we let them run without interfering, the phase difference between their activities  $\Phi_{XY} = \varphi_X - \varphi_Y$  performs a random walk, as their frequencies fluctuate independently from each other<sup>1</sup>. We want to pulse X to keep it synchronized with Y. To achieve this, first, we track their phases  $\varphi_X$  and  $\varphi_Y$  in realtime, using the AR model to forecast signal at each time point (see Fig. 6.4A). Once  $\Phi_{XY}$  surpasses the allowed threshold level (more than an eighth of a cycle difference,  $|\Phi_{XY}| > \pi/4$ ), we apply a stimulation pulse at just the right phase in order to enact a shift in X’s phase  $\Delta\varphi_X$  that is as close as possible to the required correction  $-\Delta\Phi_{XY}$ . As soon as  $\varphi_X$  matches the desired onset phase, the stimulation current is given. After the pulse, we enforce a refractory period of  $\tau_{\text{ref}} = 100$  ms when

<sup>1</sup> In our mathematical notation, we consistently designate *phases* with  $\varphi$ , *phases shifts* (induced by the perturbation) with a prefix  $\Delta$ , and *phase differences* (between oscillators  $i$  and  $j$ ) with a Greek uppercase  $\Phi_{ij}$ . Consequently,  $\Delta\Phi_{XY}$  will describe the phase shift induced by a pulse on the phase difference between oscillators X and Y.

no pulses are allowed in order to let the network settle and maintain its new phase relationship.

#### *Synchronizing two independent oscillators.*

In Fig. 6.4B we show the resulting phase difference between X and Y, with the desired state shaded in grey. In the unpulsed control condition, due to the inherent variability in the oscillator's frequency, their phase difference constitutes a random walk, resulting in a uniform distribution. Once the closed-loop procedure is applied, the difference of phases between the oscillators shows the desired distribution centered around the target phase state ( $-\pi/4$  to  $+\pi/4$ ). Notably, the strength of the pulse does not affect the distribution (hence, just one distribution shown for all pulse strengths in Fig. 6.4B). Once the first few pulses bring the oscillators into the desired phase relationship, only small phase shifts are required in order to maintain the phase difference. Since any of the utilized pulse magnitudes are capable of achieving the required shifts, the final phase difference distribution is unaffected.

On the other hand, the model's inherent noise level plays a major role. As the noise increases, the ability of the pulsing procedure to maintain the desired state decreases. At the highest noise level, even though there PRC curve shows no reliable shifts, we still achieve a distribution centered around the desired phase difference. Note, that this is not due to any phase-response properties but is merely the effect of applying pulses to the network whenever it is not in the desired state, thus pushing it away from the 'forbidden' state, and then letting it run passively whenever the desired state is achieved - the phase onset of the pulse does not matter.

Next, we use spectral coherence to assess the amount of input signal information that is present in the networks' output activity (Fig. 6.4C). By pulsing the population, we degrade the signal content. With perturbations of higher magnitude, the amount of degradation increases appropriately. Notably, negative perturbation pulses (in blue) result in significantly less information degradation than the positive pulses (in red). The excitatory pulses evoke large bursts of spiking activity, which strongly diminishes the stimulus content measure, whereas the inhibitory pulses, at most, suppress the spiking activity to zero which results in less stimulus interference. At high noise levels and at a sufficiently high pulse magnitude (4 nA), the amount of signal information is no longer significant and falls below the 95% chance level at the bottom of the plot. Thus, if we want to use electrical stimulation for assessing information processing in the brain, we have to take care to use an appropriate pulse strength to not completely overpower the signals whose representations we desire to enhance.

#### 6.2.2 Part 2: Stimulation bistable multi-population model

Here the techniques developed in the first part of our study will be applied to an established, prototypical network implementing selective signal routing under attention. After briefly describing the model itself and its dynamics, we will first quantify how the model reacts to perturbation pulses applied to different parts of the system. Using this knowledge, we can finally interact with the model 'cortex' in a meaningful way, simulating the effects of 'natural', physiological attention by using 'artificial' pulses to selectively route external signals to neural target populations. Conversely, our results provide predictions which can be used in physiological experiments to specifically test

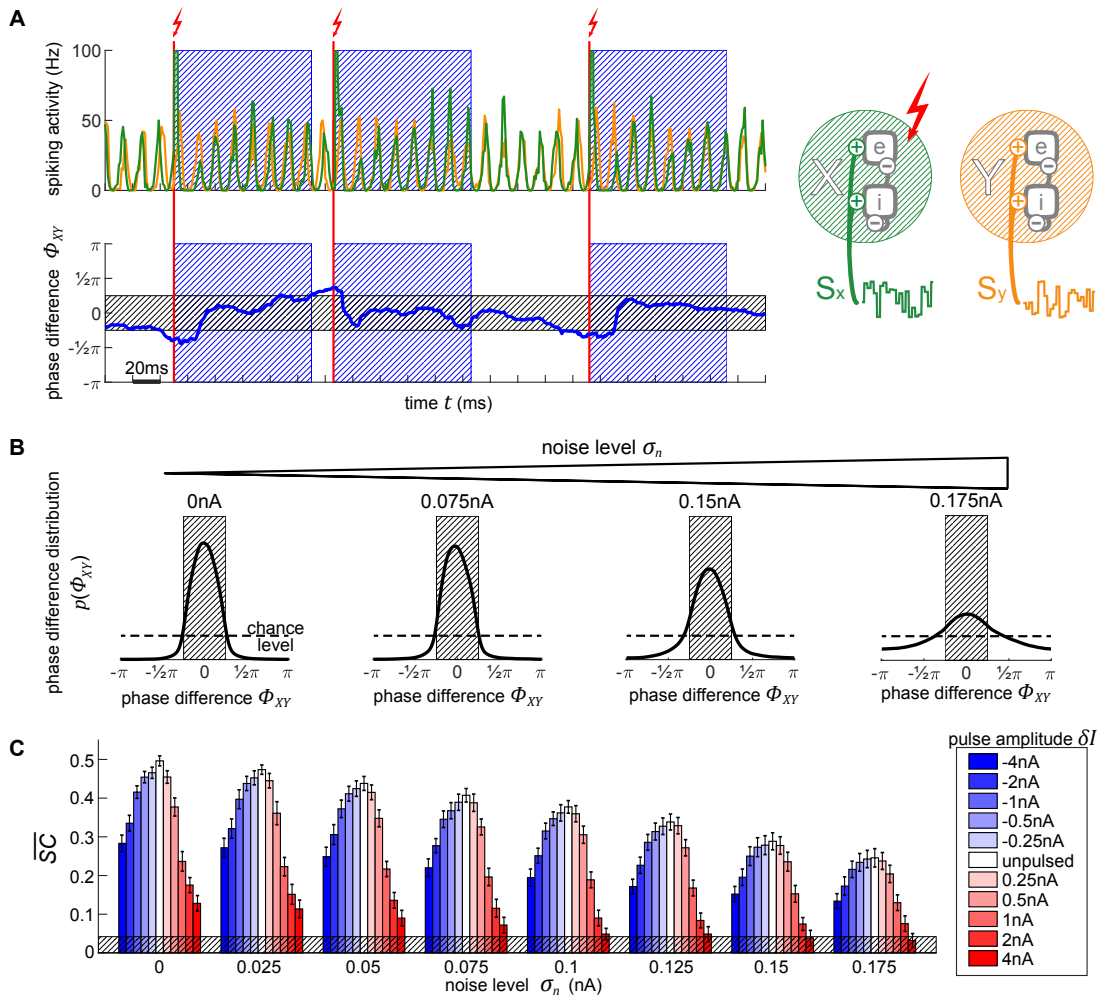


**Figure 6.4: Using PRCs to synchronize two independent oscillators.**

**A.** The top plot shows the diagram of the two oscillators next to their output activity traces, X (orange) and Y (green). As soon as the phase difference between the two oscillators (lower plot, blue line) exceeds  $0.25\pi$  in either direction (region shaded in gray), the appropriate phase for pulse onset onto X in order to achieve the required shift to bring it back into synchronization with Y is determined. Once X is at this right phase, a pulse is applied (vertical red line). Following the stimulation pulse, a refractory period is induced for 100ms during which no pulses are allowed (blue-shaded regions).

**B.** Evolution of X-Y phase difference distribution with increasing noise. With higher noise, the amount of time that the model spends in the desired state diminishes, as visible by the broadening distribution. The magnitude of the pulse does not affect the distributions, since any of the pulses are equally capable of causing the appropriate shift to maintain the desired phase relationship between the oscillators.

**C.** Signal content  $\overline{SC}$  for different pulse strengths (blue-red scale) across different background noise conditions. Stronger pulses cause larger and longer-lasting artifacts in activity which greatly reduce the signal information content measure  $\overline{SC}$ . Negative pulses consistently lead to less signal degradation than positive pulses of the same magnitude. The errorbars correspond to the SE of 10-second simulation runs. The gray shading at the bottom indicated the 95% chance level.

the particular model setup and, on a more general level, hypotheses about the still debated neural mechanisms realizing communication-through-coherence.

### 6.2.2.1 Structure and dynamics of network

#### *Setup and connectivity.*

We use the single population network from part 1 to construct a model composed of several interconnected oscillator modules, representing interactions between neuron populations in areas V1 and V4, similar to the work of [102]. All the projections between the populations originate from their respective excitatory subpopulation, reflecting the finding that inhibitory neurons have been found to form primarily local connections, whereas the excitatory neurons project to up- and downstream visual areas [210], and laterally to neighboring populations [211].

A schematic of the model is presented in Fig. 6.5A. The input (upstream) layer of the model is composed of two oscillators, X and Y, representing two neighboring V1 populations. These are driven by afferent connections delivering independent Poisson spike trains, each modulated by its own input signal,  $S_X$  and  $S_Y$ . Furthermore, X and Y share a connection from the excitatory pool of neurons of one population to the inhibitory neurons of the other,  $X_e$  to  $Y_i$  and  $Y_e$  to  $X_i$  with connection probability  $p_{XY} = 0.02$  and delay  $\tau_{XY} = 5$  ms.

In the output (downstream) layer of the model, a third oscillator Z represents a single V4 cortical population that receives input from each of the V1 populations, emulating the convergence of receptive fields when going downstream in the visual system.  $X_e$  and  $Y_e$  project with equal strength onto  $Z_e$  with connection probability  $p_{Z_e}$ , and onto  $Z_i$  with connection probability  $p_{Z_i}$ . Each of the individual populations retains local parameters of the single cortical population from the previous section, resulting in cyclic activity within the same natural frequency.

Increasing levels of additional background noise significantly increase the firing rates of integrate-and-fire neurons [32]. Since our model contains all sorts of recurrent connections, these increased firing rates cause various runaway effects that drastically change the behaviour of the model. Thus, to make the comparison between different noise levels fair, we scale the driving magnitude of the afferent inputs into each population in order to maintain consistent firing rates across the conditions. First,  $S_e(t)$  and  $S_i(t)$  are scaled for the X and Y oscillators, similar to the case with a single cortical population. Once X and Y evoke the desired output spiking rate of 15 Hz,  $p_{Z_i}$  and  $p_{Z_e}$  are scaled such that Z is sufficiently driven to display the same spiking rates as well.

#### *Model dynamics.*

Due to the intra-population connectivity between X and Y and their associated synaptic delays, their oscillations are consistently in an anti-phase relationship. The outputs from X and Y drive compete to entrain Z, which results in bistable model dynamics as described in [102].

To demonstrate these dynamics, we display a snippet of activity in Fig. 6.5B-E, focusing on  $Z_e$ . When Z is entrained by X, the troughs of  $Z_i$ 's input to Z activity correspond to the peaks of X and to the troughs of Y, and vice versa when Z is entrained by Y (marked by the vertical lines throughout plots B-D). Thus, during the first half of the displayed activity,  $Z_e$ 's spikes are mostly driven by X's input, and the second half by Y. These sort of dynamics enact the CTC mechanism to route the input information  $S_X$

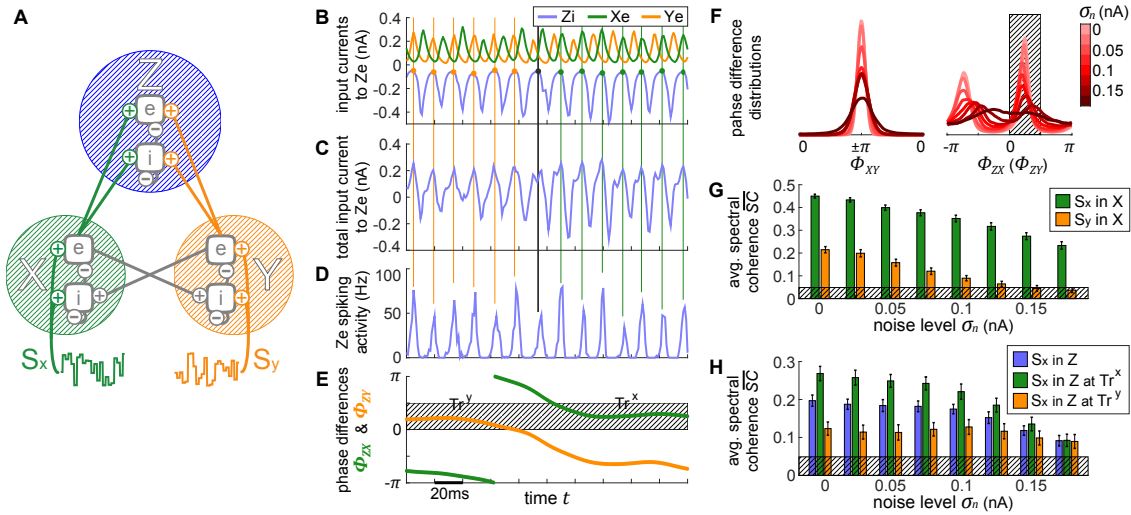


**Figure 6.5: Bistable XYZ model.**

**A.** The model consists of three cortical populations X, Y and Z. X and Y form the lower layer of the model, each subpopulation is driven by its own input signal  $S_X$  and  $S_Y$ . X and Y are connected laterally, from the excitatory subpopulation of one population to the inhibitory subpopulation of the other. The lateral connectivity is set up such that the two populations' activity oscillates in antiphase. The outputs of X and Y drive the activity of Z which forms the upper layer.

**B-E.** In row B, we display the postsynaptic currents in  $Z_e$  as a result of the inputs it receives from  $X_e$ ,  $Y_e$  and  $Z_i$ . X and Y's activity is consistently in antiphase. In row C, we show the sum of all these currents, which then leads to the spiking activity displayed in row D. The peaks of Z's own oscillatory (from  $Z_i$ ) activity are marked in B, with vertical lines extending across the plots in order to track their location. Towards the beginning, these peaks align with the peaks of  $X_e$  current, switching to  $Y_e$  partway through time, indicated by the color of the vertical lines. Thus, at first  $X_e$ 's input fails to evoke spikes in  $Z_e$  since it coincides with the highest inhibition from  $Z_i$  whereas towards the end the spiking activity is driven primarily by  $X_e$ , demonstrating the idea behind information routing via the CTC mechanism. In row E, we show the phase differences  $\phi_{X_e} - \phi_{Z_i} = \Phi_{ZX}$  and  $\phi_{Y_e} - \phi_{Z_i} = \Phi_{ZY}$ . They grey shaded region indicates the favorable phase difference, which corresponds to aligned peaks between  $Z_i$  and  $X_e$  or  $Y_e$  currents. At the beginning of the displayed data snippet, the networks state is favorable to transfer Y's information,  $Tr^Y$ , switching to be favorable for X,  $Tr^X$ , in the latter portion.

**F.** The distributions of phase differences for different levels of internal noise for the X-Y populations (left) and X-Z or Y-Z populations (right) are shown. The two peaks of the distributions in the right-hand plot indicate the bistable dynamics of the network. Phase differences between 0 and  $0.5\pi$  correspond to the preferred state when information routing should be optimal (shaded in grey).

**G.** The signal content  $\overline{SC}$  in the activity of X and Y as a function of internal noise level. X activity manifested mostly the input signal  $S_X$  and significantly less of input signal  $S_Y$ , which shows up due to the lateral connection between X and Y.

**H.** The stimulus content of  $S_X$  input in Z is shown, first without considering the state of the network and then separately for each state,  $Tr^X$  and  $Tr^Y$ . The errorbars in G and H correspond to the SE of 10 second simulation runs and the grey shading at the bottom indicates the 95% chance level.

or  $S_Y$  depending on which population  $X$  or  $Y$  is in a favorable (matching peaks) phase relationship with  $Z$ .

When the peaks of the currents in  $Z_e$  appear aligned, the stable state phase differences  $Z - X = \Phi_{ZX}$  and  $Z - Y = \Phi_{ZY}$  do not perfectly correspond to 0, but rather span the range between 0 to  $0.5\pi$ , derived empirically from the models behaviour (shaded in grey in Fig. 6.5E). This is merely an epiphenomenon of the phase extraction, due to the mismatch between the signals' waveforms which stray away from perfect sinusoids.

We designate the system's stable states by using the  $\Phi_{ZX}$  and  $\Phi_{ZY}$  phase differences: state  $\text{Tr}^X$  when  $Z$  is entrained by  $X$  ( $0 < \Phi_{ZX} < 0.5\pi$ , corresponding to 25% of available phases) and  $S_X$  information should be transferred over to  $Z$  while  $S_Y$  is suppressed by  $Z_i$ 's inhibition and state  $\text{Tr}^Y$  ( $0 < \Phi_{ZY} < 0.5\pi$ , corresponding to 25% of available phases) when the opposite is true. Considering that  $X$  and  $Y$  are always oscillating in anti-phase, this leaves half of the available phases as the unstable region, when the system is transitioning from one state to the other.

The bistable dynamics of the system are clearly visible in the bottom row of Fig. 6.5F where we plot a histogram of  $\Phi_{ZX}$  and  $\Phi_{ZY}$  phase differences, across multiple noise conditions. As can be expected, with increasing levels of noise, the system's affinity to maintain its stable states decreases.

#### *Signal transmission.*

The inherently bistable dynamics provides a perfect mechanism for implementing communication through coherence (CTC). The CTC hypothesis states that when a population receives multiple oscillatory inputs, it can selectively route one and suppress the others by establishing favorable and unfavorable phase relationships, respectively. For example, in the first half of the trial shown in Fig. 6.5B-E,  $X$  input to  $Z_e$  arrives when  $Z_e$  is least inhibited by the  $Z_i$  input, putting it into an excitable state and allowing the information content of the signal in  $X$  to propagate into (and through)  $Z$ . Simultaneously, the bursts of  $Y$ 's activity arrive concurrently with maximal inhibition from  $Z_i$ , hence suppressing  $Y$ 's information content. In sum, the output spikes of  $Z$  during this period primarily reflect the activity it receives from  $X$ . The same is true in the other direction – when  $Y$  wins the entrainment 'battle' over  $Z$ , its output propagates onwards, while  $X$ 's output is effectively suppressed. In the following, we will call these two stable states trans- $X$ -favorable (abbreviated  $\text{Tr}^X$ ) and trans- $Y$ -favorable (abbreviated  $\text{Tr}^Y$ ).

By using the spectral coherence, we assess the content of each input signal,  $S_X$  and  $S_Y$ , in all three populations  $X$ ,  $Y$  and  $Z$ . Due to the recurrent connections between  $X$  and  $Y$  that were not present in the independent case considered in part 1, there is a weak mixing of the input signals in the first layer, as seen in Fig. 6.5G.  $X$  represents primarily  $S_X$  (orange line), and to a small but significant extent  $S_Y$  (green line). For reasons of symmetry, the same lines also represent signal content in  $Y$  (orange for  $S_Y$  in  $Y$ , and green for  $S_X$  in  $Y$ ).

If we compute the representation of each input signal  $\overline{SC}$  in  $Z$  output without regard for the current state ( $\text{Tr}^X$  or  $\text{Tr}^Y$ ), we find that on average each signal is equally expressed, as indicated by the blue bars in Fig. 6.5H. However, when we assess signal content when the network is in the  $\text{Tr}^X$  state, we find that  $Z$  activity contains significantly more information from  $S_X$  (green bars) as opposed to when the system is in  $\text{Tr}^Y$  state (orange bars). Thus, the model does indeed perform signal routing, stochastically switching between the two equivalent input sources. As we increase the background  $1/f$  noise, qualitatively none of these relationships change – populations in a favorable phase relation always route more information. However, at a sufficiently high noise level ( $\sigma_n > 0.15$  nA), the

difference between stimulus content  $\overline{SC}$  during  $\text{Tr}^X$  and  $\text{Tr}^Y$  states is no longer significant (Student's t-test between two sets, composed of 100 simulations of 10 seconds each,  $p > 0.05$ ).

### 6.2.2.2 Pulse-response characteristics of the model

As introduced earlier, we will use  $\varphi_i$  to denote the phase of oscillator  $i$ , and  $\Delta\varphi_i$  to denote the change in phase of oscillator  $i$  induced by an external pulse. The probability  $\rho_\tau(\Delta\varphi_i|\varphi_i)$  to observe a phase shift  $\Delta\varphi_i$  a delay  $\tau$  after a pulse was given when the oscillator was at phase  $\varphi_i$  then constitutes a stochastic realization of the *phase response-curve* (PRC) of unit  $i$ .

However, in our extended model an oscillator is part of a network in which a single oscillator's phase is less important for network function than *phase differences* between *pairs* of oscillators. For example, in order to gate an input signal from population X to population Z, their phase difference must be close to 0 as was observed in the previous section. For this reason, we will also consider how the phase difference  $\Phi_{ij} = \varphi_i - \varphi_j$  between populations  $i$  and  $j$  is affected by a pulse, giving us a distribution  $\rho_\tau(\Delta\Phi_{ij}|\Phi_{ij})$  over induced phase difference shifts  $\Delta\Phi_{ij}$ . Since these shifts are indicative of changes in the network state, we will use the term 'state switch characteristics' for these distributions.

One can distinguish two conceptually different possibilities to interact with the network: Pulsing population X (or Y) from the input layer, or pulsing population Z in the output layer. In the following paragraphs, we will investigate these two possibilities in more detail, with Fig. 6.6 illustrating the corresponding effects at a delay of  $\tau = 100$  ms after the pulse, at an intermediate noise level of  $\sigma_n = 0.075$  nA. Furthermore, we assume the network to be in a  $\text{Tr}^Y$  state, and we will thus compute the state switch probabilities to the  $\text{Tr}^X$  state.

#### *Pulsing input layer population X or Y.*

If we apply the pulse to one of the lower level populations, the perturbation will propagate forth and back via recurrent connections and lead to a cascading effect of pulse echos. However, after more time passes ( $\tau = 100$  ms is more than sufficient), the X-Y populations settle back into their anti-phase relationship. Because of this, at a sufficient delay  $\tau$ , the PRC densities for X and Y are essentially identical and appear to resemble a diffused version of the PRC in the single oscillator case (compare the left graphs from Fig. 6.6A and B to the corresponding plot in the middle of Fig. 6.3B).

How do these perturbations act on the output population Z? A pulse given at a peak of X's activity arrives at a trough of Z's activity, giving rise to the phase shifts  $\Delta\varphi_Z(\varphi_X)$  shown in the middle graph of Fig. 6.6A. However, if a pulse is given at a peak of Y's activity, the propagated pulse arrives at Z at about the same phase as the initial perturbation was given to Y, resulting in the phase shifts  $\Delta\varphi_Z(\varphi_Y)$  shown in the middle graph in Fig. 6.6B.

How do these different effects of a pulse given to the input layer combine and affect the global state of the network? To obtain the corresponding measure  $\Delta\Phi_{ZX}$ , we can take the difference between the corresponding data points from the left and middle graphs in Figs. 6.6A and B, thus obtaining the state switch densities. The corresponding graphs displayed in the right column of Fig. 6.6A and B reveal a bimodal distribution with peaks at 0 and  $\pi$ . In order to best summarize the concentrations in the state switch

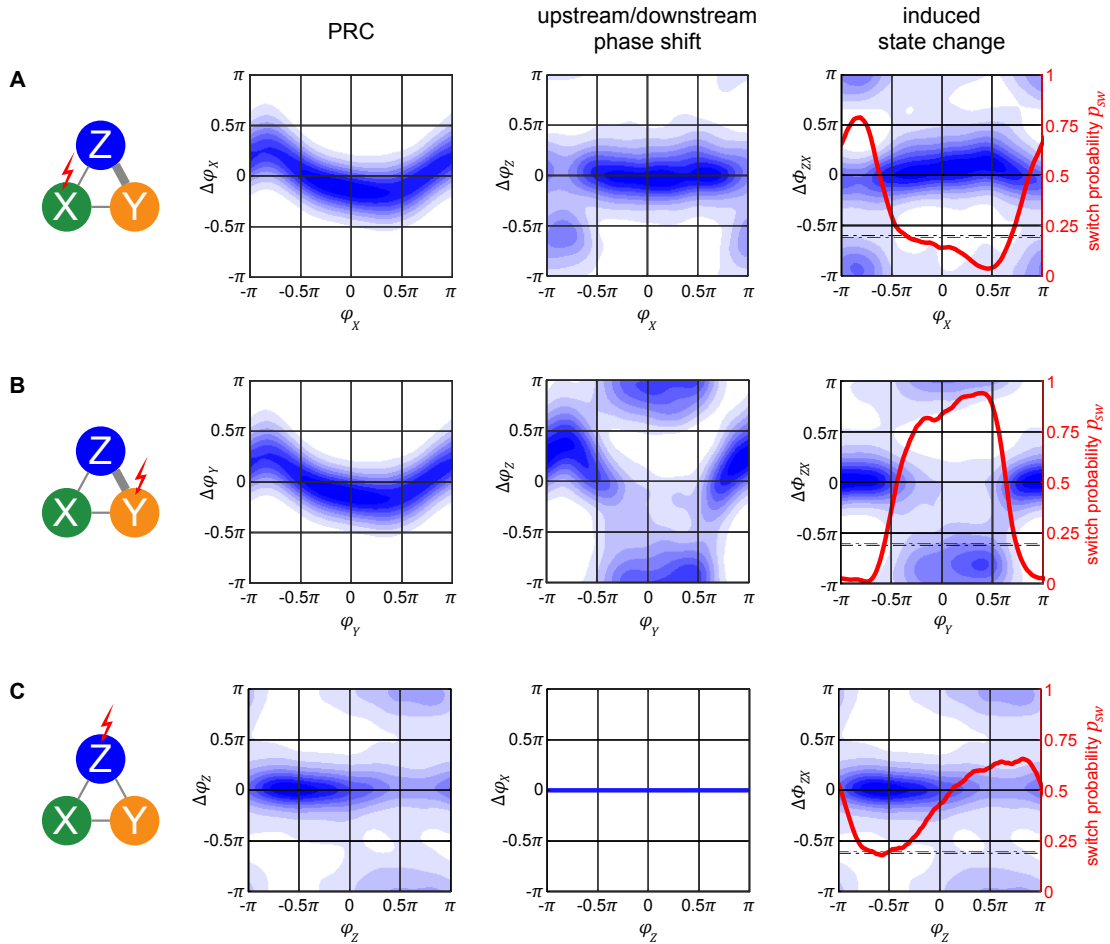


**Figure 6.6: Phase-response and state switch characteristics of the network**

Assuming the network being in a  $\text{Tr}^Y$ -state, response characteristics for stimulation of input layer populations X (panel A) and Y (panel B), as well as for stimulation of output layer population Z (panel C) are displayed. The first column of graphs shows the phase response curves (PRCs) for the stimulated oscillator. Note that these are different from the single oscillator PRCs since the oscillators are now embedded into a larger system. The second column of graphs shows the effect a pulse has on the respective output layer (panels A and B) or input layer (panel C) population. Blue shading in both columns quantifies the probability density of causing any specific phase shift with darker colors indicating higher probabilities. By taking the difference between the corresponding data points in the densities shown in the left and middle column, we can compute the probability to switch to a  $\text{Tr}^X$  state, which is exemplified in the third column. Since there is no feedback from output population Z to input populations X or Y, the response of X to a pulse onto Z is flat (lower middle graph). The horizontal dashed line in the third column represents the passive switch chance after 100ms of runtime. Noise level was  $\sigma_n = 0.075$  nA for all panels, and pulse strength  $\delta I = 1$  nA (4 nA) for panels A/B (panel C).

densities around 0 and  $\pi$ , we calculate the state switch probability  $p_{sw}$  across the onset phases  $\Phi$  via  $p_{sw} = 1 - \int_{-\pi/2}^{+\pi/2} \rho(\Delta\Phi) d\Delta\Phi$ .

#### *Pulsing output layer population Z.*

Since Z does not send feedback projections to the input layer, the effect of a pulse stays confined exclusively to Z's activity and is independent on the system being in state  $\text{Tr}^X$  or  $\text{Tr}^Y$ . Because of this, any phase shift  $\Delta\varphi_Z$  induced onto Z is equivalent to the shifts in phase difference  $\Delta\Phi_{ZX} = \Delta\Phi_{ZY} = \Delta\varphi_Z$  between X and Z, and between Z and Y. In Fig. 6.6C we can see that the resulting PRC and state switch distributions are bimodal and have peaks around 0 and  $\pi$ , unlike the effect of a pulse on the single cortical network studied in the previous section. This result is due to the bistable dynamics, which after the immediate effect of the pulse cause Z's phase to continue shifting until one of the stable states is reached. For this reason, the behavior is also independent on noise and pulse magnitude. Accordingly, the final phase shift can be either close to zero or close to  $\pi$ , corresponding to no system state change or to a switch between stable states  $\text{Tr}^X$  and  $\text{Tr}^Y$ , respectively.

When the pulse magnitude is sufficiently small, e.g.  $\delta I \leq 1$  nA, a state change is unlikely (not shown) since the corresponding average phase shift for a single oscillator is too small,  $\Delta\varphi_X \leq 0.5\pi$ . Once we increase the pulse strength the likelihood for a phase shift of  $\pi$  increases, with their respective phase onset locations roughly corresponding to the ones which led to  $\Delta\varphi \geq 0.5\pi$  phase shifts in the single oscillator (e.g. compare to Fig. 6.3B, bottom middle plot). Once the strength of the pulse is sufficiently high, a full state reset of the whole system is achieved. Even if the pulse strength is doubled, there are only small changes to the state switch probabilities (Fig. 6.6C).

Although an initial pulse magnitude of 1 nA was insufficient to obtain a high state switching probability when pulsing Z, when pulsing X with the same strength a much higher switching probability is observed, and for a large range of pulse onset phases (red curves in right column of Fig. 6.6A and B). There are two reasons why switching is easier when targeting an input population: first, the perturbation does not only affect one population but is propagated to all other 'players' in the network, and second, for a brief period of time after the pulse, the anti-phase relationship between X and Y is affected.

#### 6.2.2.3 *Optimizing stimulation pulses for state switching*

Our goal of using stimulation is to cause the network to be continuously in a desired state  $\text{Tr}^X$  or  $\text{Tr}^Y$  for either transmitting signal X or signal Y, respectively. By deriving state switching probabilities from phase-response curves as described in the previous subsection, we now have a tool for optimizing the stimulation pulse parameters towards this goal. Accounting for symmetry between X and Y, all the following results are presented with the aim of switching to a  $\text{Tr}^X$ -favorable state. By this design, whenever the network is already in a favorable  $\text{Tr}^X$  relationship, no perturbation is necessary. However, if at any point the network instead is in a  $\text{Tr}^Y$  favorable relationship, we can apply a pulse either to population X, Y, or Z to attempt to switch the state to  $\text{Tr}^X$ .

In Fig. 6.7, we display the network's state switch capabilities for  $\text{Tr}^Y \rightarrow \text{Tr}^X$  for negative and positive pulses, for each of the three possible pulse-target populations X, Y, and Z. In the plots, we show the *change* in switch probability  $\Delta p_{sw}$ , since the unpulsed system

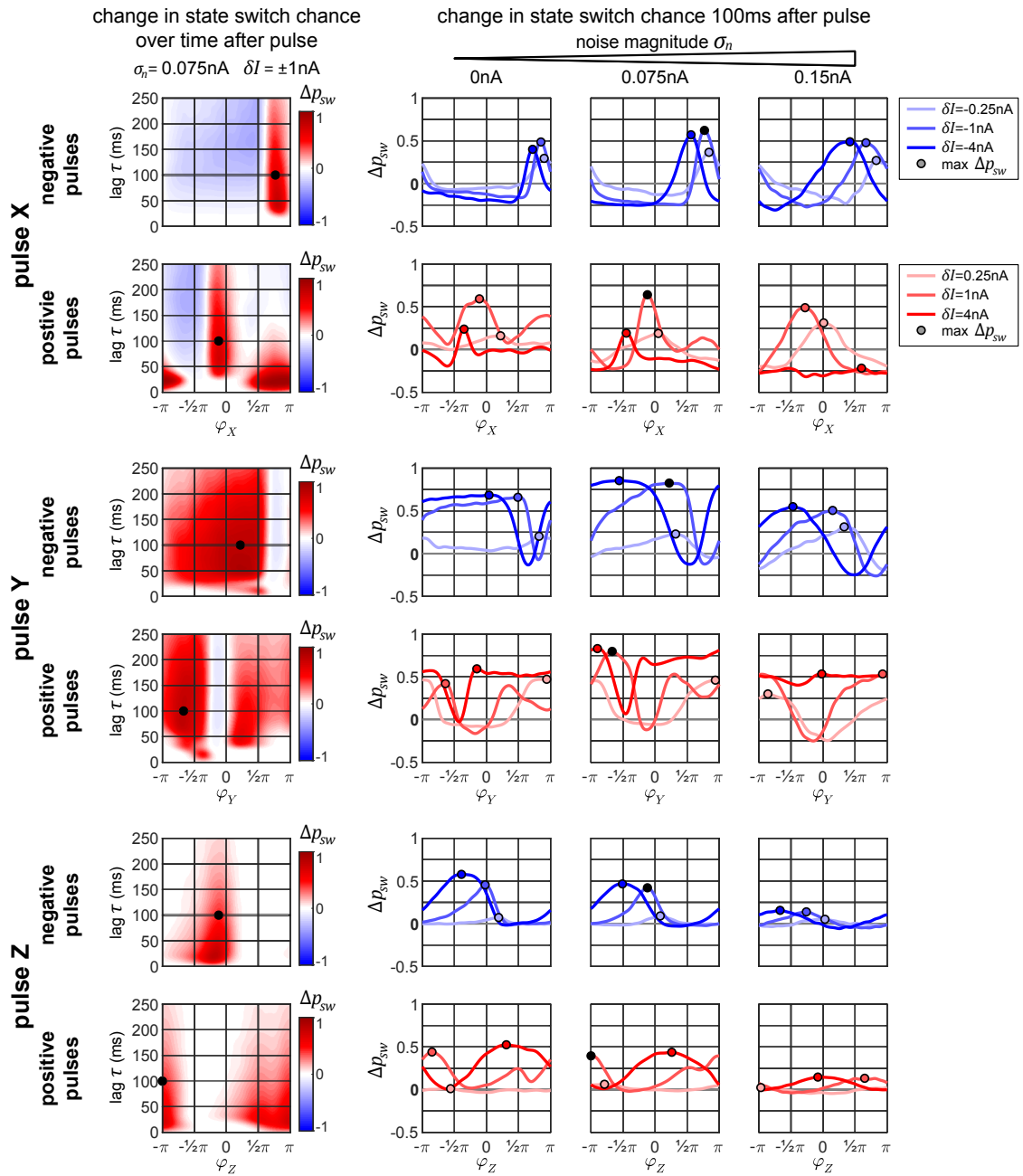


**Figure 6.7: Changes in state switching probability.**

State switch capabilities for a transition  $\text{Tr}^Y \rightarrow \text{Tr}^X$  for the three possible target populations X, Y, and Z of the pulse (upper, middle, and bottom sets of two rows each, respectively) for negative and positive pulses (top and bottom row in each set). The leftmost plot in each row shows how the change in state switch probability  $\Delta p_{sw}$  depends on the phase of the pulse onset (horizontal axis) and how it evolves over time (vertical axis going up). The remaining three plots in each row display the switch chance 100ms after pulse onset, for multiple magnitudes of the pulse (differently colored lines in each graph) for different background noise levels (separate plot for each noise condition). In each plot, the maximum switch probability is marked by a small circle. The leftmost plot in each row corresponds to one line from the middle plot of the three on the right.

already possesses a non-zero passive switch probability. In the column on the left, we show how this probability evolves over time (vertical axis) for a medium amount of noise  $\sigma_n = 0.075\text{nA}$  and medium pulse magnitude  $\delta I = \pm 1\text{nA}$  in dependence on onset phase  $\varphi$  of the pulse (horizontal axis) in order to show how the switch probability evolves over time. In the rightmost three plots in each row, we show the switch probability for multiple pulse magnitudes (different colored lines in each plot) for increasing levels of background noise (the three separate plots). The plots in the column on the left correspond to one line in the middle plot of the three on right. The maximum  $\Delta p_{sw}$  is marked in each plot to indicate the optimal onset phase, which can be used in order to switch the system states. Crucially, in some cases, a pulse leads to a negative  $\Delta p_{sw}$  indicating that, if delivered at the wrong moment, a perturbation can actively *hinder* a transition to  $\text{Tr}^X$  and instead stabilize the undesired  $\text{Tr}^Y$ -state. In the following paragraphs, we briefly discuss the effects of pulsing the different target populations.

#### *Pulse X.*

The graphs in Fig. 6.7, top two rows, reveal that in addition to having an optimal onset-phase, for each noise condition, there is also an optimal pulse magnitude that results in the largest increase in switching probability, indicated by a small circle. Interestingly, for the medium level of noise, we observe larger switch probabilities than the zero-noise condition.

When applying a negative pulse, there are always intervals of phase onsets that increase, and intervals that decrease the probability of the network switching its state. On the contrary, when applying a positive pulse, at a high noise level ( $\sigma_n = 0.15\text{ nA}$ ) and a high pulse magnitude ( $\delta I = 4\text{ nA}$ ) the onset phase does not appear to matter for the final outcome. In this particular case, all phase onsets lead to a decrease in the switch probability.

The amount of time it takes the network to settle down onto a new state tends to increase with pulse strength ( $\approx 30\text{ ms}$  for  $\delta I = 0.5\text{ nA}$  pulse vs.  $\approx 60\text{ ms}$  at  $\delta I = 2\text{ nA}$  and  $4\text{ nA}$ , not shown in figure). A stronger initial current causes a stronger reverberation of the perturbation, which then takes longer to decay within the system, increasing the time it takes the network to settle back to its normal activity. This effect is particularly strong for the positive pulses, where we get to observe the different phase-states the system goes through before settling down. A negative pulse briefly suppresses all the activity in the network, whereas a positive pulse evokes a volley of spikes in the target population, which then travels and acts as its own perturbation across the throughout the system.

#### *Pulse Y.*

When pulsing Y instead of X, the graphs in Fig. 6.7, rows 3 and 4, reveal that the switch probabilities appear complementary to the ones from pulsing X. When pulsing X, if a specific phase onset leads to an increase in switching probability, the same phase onset typically leads to a decrease in switching probability if pulsing Y instead. This makes sense, since by changing which population (X or Y) we are pulsing at one specific pulse onset phase, we are essentially changing the onset phase of the propagated pulse that arrives to Z by an amount of  $\pi$ , since X and Y maintain an anti-phase relationship.

Because of this, when applying a positive pulse of a large magnitude ( $\delta I = 4\text{ nA}$ ) in the noisy condition ( $\sigma_n = 0.15\text{ nA}$ ), the probability of a switch is now consistently high across all pulse onsets, whereas in the previous condition a pulse to X was always decreasing switch probability.

### Pulse Z.

As described previously for Fig. 6.6, when pulsing Z, a pulse of low magnitude is hardly sufficient for inducing a significant change in the switch probability. As the noise level of the system increases, the switch probability decreases substantially (Fig. 6.7, bottom two row).

#### 6.2.2.4 Controlling signal transfer

The paradigm to control the synchronization state of the network is similar to controlling the phase of an independent oscillator, with one crucial difference: In the independent oscillator case, a pulse is applied at various phase onsets, depending on what sort of a phase shift is currently necessary. In the network, however, the choice is binary: to switch or not to switch. If we desire to change the current system state, then there is just one specific optimal onset-phase for the pulse. So, for every pulsing condition (i.e., which population pulsed, pulse magnitude, pulse polarity, and network noise level), the state control procedure comes down to the following:

At a time point  $t$ , apply the stimulation pulse if the following conditions are met

1. Last pulse was more than  $\tau_{\text{ref}}$  ago.
2. The system is in the wrong state and a switch is necessary.
3. The current phase of the pulsed population corresponds to the one that leads to the highest switch probability.

In order to evaluate how well the pulsing procedure works, we first quantify the proportion of time that the system spends in the desired target state (Fig. 6.8). At the top of each plot, we display the proportion of time that the network spends in that state without pulsing. As defined previously, the desired state is set to the interval  $\Phi_{ZX} \in [0, 0.5\pi]$ , which corresponds to a quarter of the full interval of possible differences.

The goal of the perturbation pulses is to increase this value as much as possible. The results observed in this figure perfectly reflect the corresponding switch chance as predicted by the plots in Fig. 6.7. This is especially clear in the case when we pulse X with using a large positive perturbation ( $\delta I \approx 4$  nA) at a high noise level ( $\sigma_n \approx 0.15$  nA). In this condition, the effect of the pulse can only decrease the switch chance, indicated by the blue regions in the top right plot. In all other cases, the procedure succeeds at increasing the amount of time the network spends in the desired state.

Similar to our previous results from pulsing independent oscillators, the performance of the procedure decreases with increasing noise level. On the contrary, in the network the pulse magnitude and polarity plays a crucial role, whereas in the independent case, the strength of the pulse had no significant effect on the performance. In fact, we observe qualitatively different patterns for which pulse is optimal across the different pulse-polarity and pulsed-target conditions. For instance, when pulsing X, a pulse of  $\delta I = -1$  nA or 1 nA achieves the best performances. However, when pulsing Y, negative pulses get better results at higher magnitudes (saturating at sufficiently high levels), whereas positive pulses exhibit lower performance once the magnitudes are sufficiently high.

Generally, with our model's specific setup, the results seem to indicate that pulsing Y (i.e. the population whose information we wish to suppress) provides a much more robust and forgiving conditions, by having more admissible phases of the perturbation onset that result to a state switch.

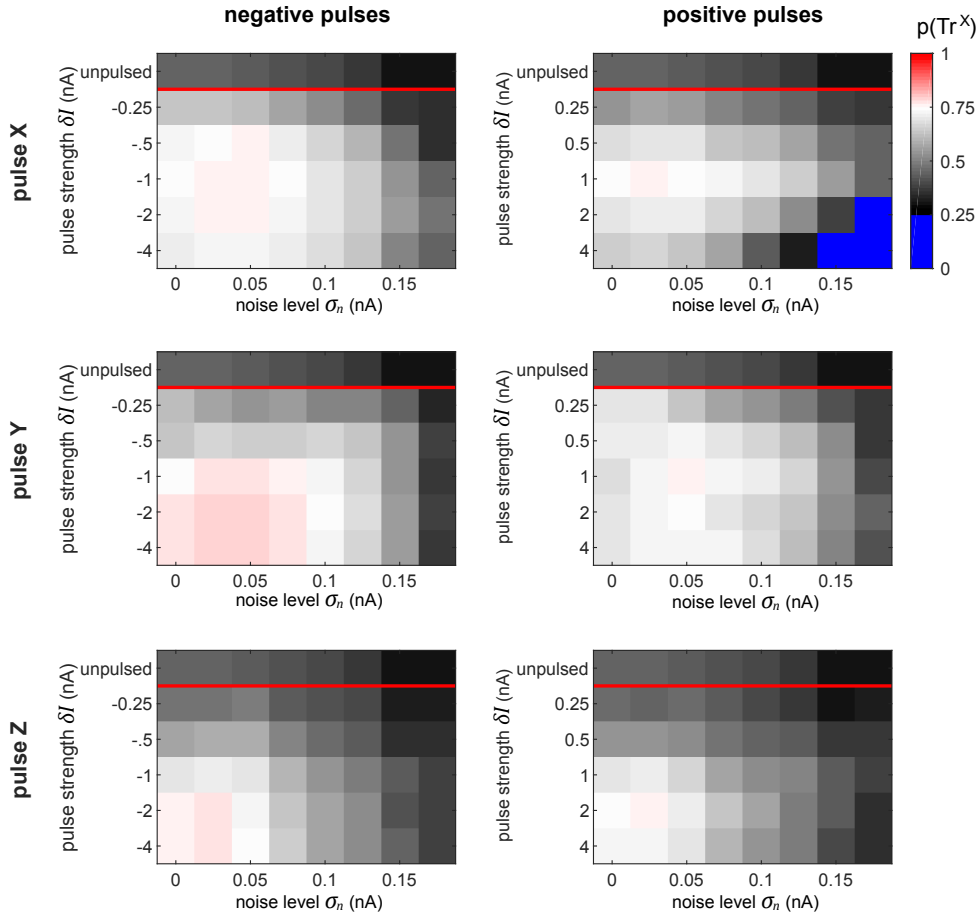


**Figure 6.8: Proportion of time spent in desired state.**

The plots display the proportion of time that the network spends in the desired state for all the conditions, as labeled. The top row in each subplot indicates the amount of time that the network spends in the desired phase state passively, without any perturbation pulses. Since our favorable state covers 0 to  $0.5\pi$ , the chance level of being in the favorable state is 0.25. To highlight this, the color map turns sharply blue below this value. Thus, the sessions (see Fig 6.7) whose pulses could only achieve decreasing the switch probability are colored blue.

Further, we evaluate the signal routing performance of the pulse procedure by evaluating the difference between  $S_X$  and  $S_Y$  signal contents in  $Z$ . These differences are displayed in Fig. 6.9. Insignificant differences are marked appropriately ( $p > 0.05$ , Student's t-test). At the top of each plot, the maximally achievable difference is displayed, as seen in Fig. 6.5C, by evaluating the signal content in  $Z$  without delivering any pulses, but for the time intervals in which the system is spontaneously in the preferred state for transmitting a specific signal.

As we observed in the independent oscillator case, increasing the pulse magnitude increases the amount of degradation of the external signal in the population's activity in all the conditions. In some cases, a pulse of a higher magnitude actually leads to a better performance in terms of keeping the network in the desired state, but simultaneously, it also increases the amount of signal degradation. Since we focus on signal routing differences, the results in Fig. 6.9 reveal the appropriate compromise to achieve the best gating performance.

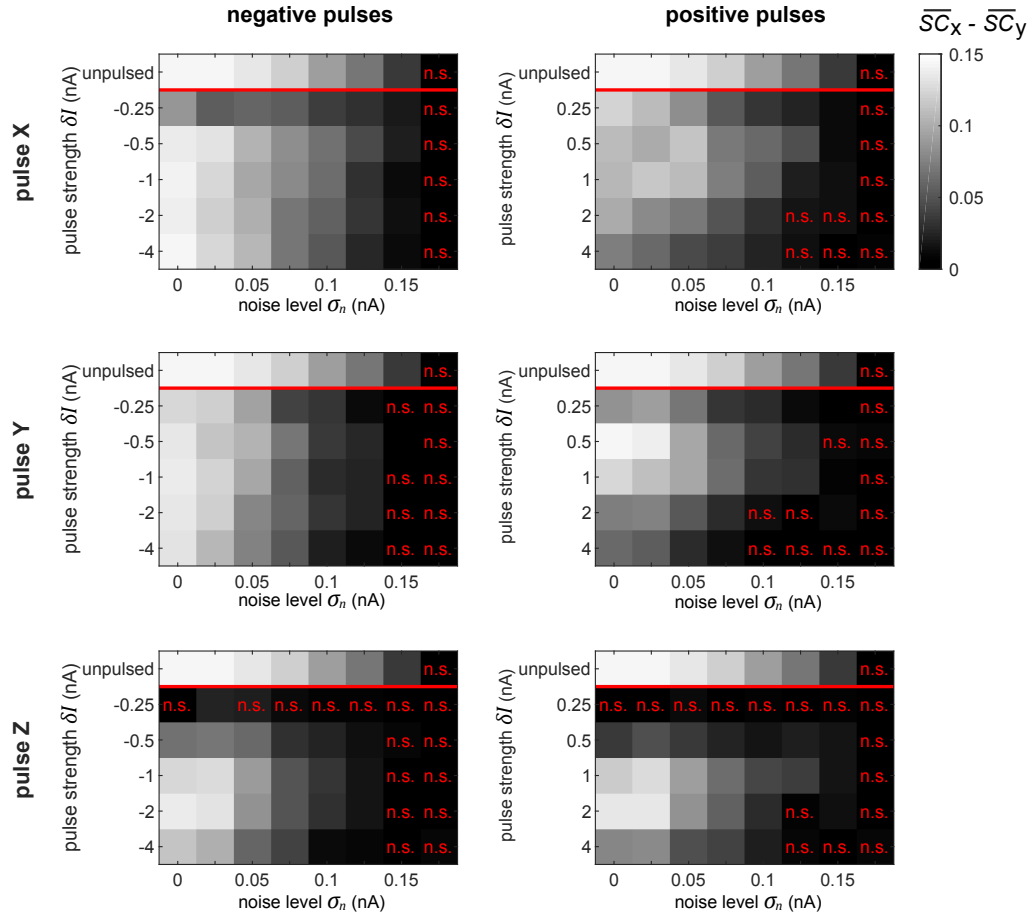


**Figure 6.9: Selective signal routing via precisely pulsing the network.**

Difference in transferred signal content between the two competing input stimuli  $S_X$  and  $S_Y$  for different stimulation paradigms (rows) and pulse polarities (columns), evaluated for different pulse magnitudes  $\delta I$  (vertical axes) and noise levels  $\sigma_n$  (horizontal axes). The top row in each graph shows the corresponding 'optimal' or maximally achievable signal routing performance extracted from time intervals when the network was in a particular preferred state (here, in  $\text{Tr}^X$ ). Parameter combinations marked by a red 'n.s.' indicate conditions where the difference in signal transfer was not significantly different from zero (Student's T-test,  $p < 0.05$ ).

In a recurrent network, the effect of the pulse on external signal representations is not straightforward and hard to predict. First, the signal represented by the pulsed population is degraded by the injected current. Subsequently, the pulse propagates throughout the rest of the system, causing further degradation of signal representations in *other* populations. Consequently, the signal routing performance crucially depends on which population is pulsed. For instance, if we compare the results in the zero noise condition when pulsing X or Y with a positive pulse of  $\delta I = 1$  nA, we find that pulsing Y provides much better routing results, even though pulsing X is actually better at establishing the desired network state (see Fig. 6.8). In this case, a significant part of the result is caused by signal  $S_Y$  getting degraded substantially more than signal  $S_X$ .

### 6.3 METHODS

#### 6.3.1 Neurons and synapses

Interactions between neurons are governed by synaptic weights  $\omega_e$  and  $\omega_i$  and conductances  $g_e$  and  $g_i$ , which reflect the magnitude and decay speed of EPSCs (excitatory postsynaptic currents) and IPSCs (negative postsynaptic currents) when receiving a spike from an excitatory or inhibitory cell, respectively.

$$g_e(t) = \omega_e \sum_{s=1}^{n_e} \Theta(t - t_{s,e} - d) \exp\left(\frac{-(t - t_{s,e} - d)}{\tau_e}\right)$$

$$g_i(t) = \omega_i \sum_{s=1}^{n_i} \Theta(t - t_{s,i} - d) \left[ \chi_1 \exp\left(\frac{-(t - t_{s,i} - d)}{\tau_i^1}\right) + \chi_2 \exp\left(\frac{-(t - t_{s,i} - d)}{\tau_i^2}\right) \right]$$

Here  $\Theta$  is the Heaviside function,  $d$  the synaptic delay, and  $t_{s,e}$  and  $t_{s,i}$  are the times of presynaptic excitatory and inhibitory spikes, respectively. The decay constants for EPSP and IPSP are given by  $\tau_e$  and  $\tau_i^{1,2}$ , with the inhibitory response containing a mixture of slow and fast components with the relative contributions controlled by  $\chi_{1,2}$ . These parameters are set to emulate realistic neurons, in accordance with Bartos et al. 2002 [12] (see table 1). The activity of the units is simulated in Matlab in discrete time using the forward Euler method with a timestep of  $dt = 0.1ms$ .

<b>Variable</b>	$A_e$	$A_i$	$p_0$	$p_1$
value	$2.88e - 4 \text{ cm}^2$	$1.2e - 4 \text{ cm}^2$	$3.89e - 9 \text{ A}$	$1.30e - 7 \text{ A/V}$
<b>Variable</b>	$p_2$	$V_e$	$V_i$	$V_{thresh}$
value	$1.08e - 6 \text{ A/V}^2$	$0 \text{ mV}$	$-75 \text{ mV}$	$-56.23 \text{ mV}$
<b>Variable</b>	$V_{reset}$	$\tau_e$	$\tau_i^1$	$\tau_i^2$
value	$-67 \text{ mV}$	$3 \text{ ms}$	$1.2 \text{ ms}$	$8 \text{ ms}$
<b>Variable</b>	$\chi_1$	$\chi_2$	$\omega_e$	$\omega_i$
value	$0.9$	$0.1$	$0.4 \text{ nA}$	$1.2 \text{ nA}$

**Table 6.1: Neuron and synaptic connection parameters.** The parameters are taken to emulate biophysically-realistic neurons, in accordance with Bartos et al. 2002 [12]. these parameters were specifically derived from neural data, corresponding to neurons responsible for generative gamma oscillations in the hippocampus.  $p_{0,1,2}$  were found by a mathematical reduction of the Hodgkin-Huxley model [1].

#### 6.3.2 Offline phase measurement

For measuring the phase of a cyclic signal, we utilize a well established procedure. For efficiency, the signal is downsampled to 1 kHz and normalized. A power spectrum of the signal is calculated using a Morlet wavelet transform, from which we determine the location and halfway points of the gamma peak. Then, we apply a zero-phase ('filtfilt' command in Matlab) finite-impulse response (FIR) bandpass filter with bandstops at the halfway points found in the power spectrum. This gives us the gamma component of the signal without distorting the phase. Afterwards, the signal is passed through a Hilbert transform [25], providing us with the complex analytical signal. The argument of

the analytical signal gives us the instantaneous gamma phase of the signal. The narrow range of the bandpass filter is necessary, since the instantaneous phase only becomes accurate and meaningful if the filter bandwidth is sufficiently narrow [171].

This sort of a procedure is prone to edge effects and especially to the artifacts induced by sudden spikes in activity due to stimulation pulses used in this study. To decrease the effect of these artifacts, the affected region is set to zero after normalization. Empirical tests showed that the edge and artifact effects on instantaneous phase measurement becomes insignificant around 2 cycles away from the affected region, around 30ms for gamma oscillations.

### 6.3.3 Realtime phase measurement

When forecasting a discrete time signal  $X_t$ , given its past time points  $X_{t-i}$ , an autoregressive model of order  $p$  is defined as

$$X_t = c + \sum_{i=1}^p \alpha_i X_{t-i} + \varepsilon_t$$

where  $\alpha_1, \dots, \alpha_p$  are the parameters of the model,  $c$  is a constant, and  $\varepsilon_t$  is white noise. The parameters and the magnitude of the noise are trained on a pre-existing set of data using the Burg lattice method ('arburg' command in Matlab). The model order  $p$  selection depends on the sampling rate and the characteristics of the input signal and is determined empirically to provide the most accurate phase measurements when compared to the offline phase measurements [150].

For speed and efficiency, the AR model was applied to downsampled 1kHz signals, for which the optimal order  $p$  was found to correspond to the the average number of time steps within a single cycle of oscillatory activity (approx 15 ms for gamma oscillations). For every condition, a separate AR model is trained on an existing 10 second trial, which provides sufficient amount of data to converge on the appropriate AR parameters.

### 6.3.4 Significance level computation

Chance levels for  $\overline{SC}_{xy}$  are calculated by pairing up the network activity with surrogate input signals. The resulting distribution of SC values allows us to extract the 95th percentile  $\overline{SC}_{95\%}$ , allowing us to evaluate the significance of the information measure score. Further, spectral coherence is affected by sampling size bias. Thus, in order to compare signal routing scores across conditions, they were consistently computed from 100 simulations 10 seconds each.

### 6.3.5 Conditioning of input drive on internal noise

Increasing the level of noise inherently raises the spiking rates of the affected neurons. Since our network relies on a series of recurrent coupling, a change in mean spiking rate would result in drastically different behavior. Thus, in order to keep the comparison between the different noise levels fair, we scale the magnitude of the mean input drive to the system ( $S_x$  and  $S_y$ ) in order to sustain comparable activity. Thus, in order to obtain comparable model activity between the different internal noise magnitude model conditions, the input drives,  $S_e(t)$  and  $S_i(t)$  were adjusted to achieve a 15Hz average firing rate for the excitatory and 60Hz for the inhibitory pools of neurons. This was achieved

via a simple gradient descent procedure. For example, for a simple oscillator and for the first layer populations  $X$  and  $Y$  of the bistable model, if the initial drive to the inhibitory neurons led to a firing rate higher (lower) than the desired 60Hz, the inhibitory drive  $S_i(t)$  was decreased (increased) by an amount proportional to the mean-squared error of the firing rate. Simultaneously, if the excitatory pool's average firing rate was lower (higher) than desired, the excitatory drive  $S_e(t)$  was increased (decreased). The model was then simulated with the updated driving rates and new firing rates were acquired, new firing rate errors were computed and the gradient procedure was repeated until convergence onto the desired firing rate values. In the bistable multi-population model, once the desired firing rates were attained for the  $X$  and  $Y$  populations, the same procedure was applied to adjust the connection probabilities from  $X_e$  and  $Y_e$  onto  $Z_e$  and  $Z_i$ ,  $p_{Z_e}$  and  $p_{Z_i}$ .

### 6.3.6 PRC and PDRC collection details

To collect the PRC curve data, we simulate 2500 runs of one second duration across all the possible conditions (noise level, pulse strength, which population pulsed). In each run, the perturbation occurs at 0.5 seconds, providing us with enough signal before and after the pulse to extract the relevant phase information. In addition, we add a control group where the pulse magnitude is set to 0 - no pulse. For each run, we compute the offline phase across the entire trial. In addition, we determine the instantaneous phase at stimulation onset  $\varphi$  by using the AR signal prediction procedure to avoid any artifacts caused by the pulse. By pairing up the appropriate trials between the pulsed and the control groups, we calculate the phase difference  $\Delta\Phi$  between the unpulsed and pulsed runs at time  $\tau$  after  $t_{onset}$ . In the independent oscillator case, the pairing process is only concerned with putting trials together with a minimal difference between their corresponding values of  $\varphi$  at pulse onset. In the bistable network, the AR procedure is used to evaluate both the onset phase of the pulsed population as well as the phase-state difference  $Z-X$  and  $Z-Y$  at pulse onset, with the pairing procedure accounting for both, the network state and the stimulation pulse onset phase.

## 6.4 DISCUSSION

The goal of this study was to investigate how precise perturbations can control a recurrently coupled neural network by using its natural tendency to be in one of several preferred network states. For this purpose, we developed a closed-loop paradigm to monitor the system state in realtime and utilized the results to deliver rare, but accurately timed stimulation pulses of proper magnitude. First, we evaluated the method on a structurally simple system – the model of a single cortical population. Here, it was possible to synchronize two independent oscillators up to a critical noise level, and to determine the optimal pulse strength. Next, we applied our paradigm to a more elaborate network of local populations representing recurrently coupled cortical populations, proposed [102] as a prototypical implementation for selective information processing via communication-through-coherence (CTC) in the visual cortex. For successfully interacting with such a system, our results demonstrate that understanding the behavior of one of its constituents in isolation (e.g. by obtaining the phase-response curves, PRCs) is not sufficient – instead one has to probe the network as a whole, which required to compute phase-difference-response curves (PDRCs). Furthermore, we investigated several ways

of interacting with the system, targeting either upstream or downstream neural populations. Ultimately, we could simulate the effect of physiological attention and gate signals by bringing the desired population(s) into a preferred (or non-preferred) phase relationship.

Certainly, the network is still an abstraction of the real networks performing selective information processing in the visual cortex. We only considered three coupled populations, back-projections from downstream visual areas were not modeled, and we assumed a lateral recurrent coupling structure which is still subject to on-going physiological and anatomical research. Furthermore, we restricted ourselves to investigate ING-oscillators only (for details, see paragraphs below). Additionally, the effects of our perturbation pulses on neural processes are highly simplified in the simulations. However, even when taking these restrictions into account, we believe our work contributes in three important aspects to the field:

- For being successful in interacting with a neural system, the current state of the system *does matter*. This is particularly obvious when trying to construct a visual intracortical prosthesis [139]. Since there are on-going dynamics in the cortex even in the absence of an actual visual stimulus [7], it is important to know when an artificial stimulus would be most effective, either in inducing a certain percept or in pushing the system into or towards a desired network state. Another requirement is to ensure an ongoing stimulus processing in downstream visual areas. For this purpose, it would be necessary to first bring the network into a state where incoming information can be successfully gated across different stages. This goal was successfully reached in model simulations of our closed-loop stimulation paradigm.
- With respect to selective information processing, we investigate *one specific* of potentially many implementations of the CTC principle. Our results therefore constitute a prediction of how the real network would behave if it would work according to our hypothesis. In particular, we predict that pulsing the populations representing the unattended stimulus would be very effective in switching between the different network states and in selectively gating a stimulus. This should not be the case if the recurrent interactions would not push the upstream populations  $X$  and  $Y$  into an antiphase relation, thus providing an opportunity to test this critical assumption.
- Finally, our study brings together the tools needed to establish realtime control of stochastic neural systems. One important insight for us were the severe restrictions imposed by noise, be it intrinsic or on the observation level. Crucially, we present a paradigm that relies on single and rare stimulation pulses, allowing to network to spend the majority of the time unperturbed. This is in opposition to utilizing continuous stimulation or repetitive pulses that explicitly entrain the system, which we argue results in non-natural and forced brain activity. Thus, we conclude that instead of explicitly forcing a network state, it should be of great benefit to account for the system's inherent multistable attractor states and utilize the minimal perturbation to let the network settle naturally in a desired network state.

Below, we discuss the relation of the model to experimental data and possible consequences of changes to the model structure for our stimulation paradigm.

#### 6.4.1 *Intra-population connectivity*

As briefly mentioned in the preceding paragraph, there are two major assumptions in the connectivity between the X,Y and Z modules in the network. First, the connectivity between the lower layer populations X and Y forces them to establish a stable and symmetrical anti-phase relationship between their activities, without establishing a clear winner between the two. Second, there are no back-projections from Z back onto X or Y.

By increasing the connection strength and changing the delays in the X–Y connection it is possible for the populations to synchronize at a different phase, exhibiting the phenomenon of biased competition [163] already in the first layer, and controlling the overall bistability of the model. In such a system, the bistable dynamics are evoked as the two populations switch between which one leads and which one follows. The phase response characteristics of such a scenario of two interconnected oscillators have been thoroughly explored in [248]. If we employed this sort of connectivity between X and Y in our model, the winner of the biased competition in the first layer would also entrain Z. As [248] show, in this scenario one is also able to control the stable state via a precisely timed stimulation pulse.

#### 6.4.2 *Local circuitry*

The source of gamma frequency oscillations in the brain has been attributed primarily to two mechanisms: ING - interneuron gamma - which we utilize in our model, and PING - pyramidal interneuron gamma [217]. In the ING mechanism, a population of mutually connected inhibitory neurons generate synchronous IPSPs, creating an ongoing rhythm which is then imposed onto the excitatory neurons [246]. In the PING mechanism a volley of excitation stimulates delayed feedback inhibition, resulting in consistent cyclic behavior when the ratio between excitation and inhibition is appropriate. Research shows that both mechanisms can work together to generate gamma frequency oscillations [18, 33, 41, 87]. Either mechanism or a combination of the two constitutes a self-sustaining oscillator and exhibits phase-response characteristics. Hence, we speculate that regardless of the oscillation generating mechanism, the method established in this study can be used to establish desired phase-locking between populations of neurons and route information – however, with a potentially different phase-(difference)-response characteristics.

#### 6.4.3 *Transient synchrony*

Even at high noise levels, the rhythmic behavior of our system is an idealized version of what is observed in the visual cortex where the amplitude of oscillations, along with the strength of synchronization phenomena occur as transient events that rarely last longer than 100ms. In particular, for the V1-V4 interaction explored in this study, gamma activity tends to occur in bursts at theta frequency through phase-amplitude coupling, corresponding to the rate of attentional sampling [44, 128, 207]. If theta phase amplitude coupling was included in our model, we presume that it should still be possible to control information routing by injecting the appropriate perturbation towards *the beginning* of each theta-coupled gamma burst.

#### 6.4.4 Modeling the perturbation

In the present study, the applied perturbations involved injecting the same amount of current into all the neurons within a local population. This was designed to model the effect of intracortical microstimulation (ICMS). If we wanted to get closer to the true postsynaptic effect of an ICMS pulse, it would be necessary to work out advanced kernels to convolve with the square wave function that we used. Additionally, it would benefit to have different weights of the perturbations effect by neuron type, physical orientation, and distance to the electrode. As long as the final perturbation is sufficiently short and precise relative to the oscillation cycle, the network dynamics should still exhibit a PRC. We believe that the method employed provides a generic pulse that can be easily modified for other potential stimulation techniques. For example, in the case of modeling an optogenetics pulse [248], the stimulation affects just a specific subset of neurons within local population (of type affected by the viral injection of a particular light-sensitive protein).

#### 6.4.5 Simulating different levels of background noise

The background noise magnitude  $\sigma_n$  has two effects. First, it masks the flicker signal to be transferred by the excitatory population, and second, it reduces amplitude and frequency of the gamma oscillations generated by the inhibitory population. By allowing for different noise magnitudes  $\sigma_n^e$  and  $\sigma_n^i$ ,  $\sigma_n^e$  would therefore predominantly attenuate signal transfer, while  $\sigma_n^i$  would rather reduce gamma amplitude and stability. As long as the noise level remains sufficiently low for the network to still exhibit stable oscillations, the conclusions of the research should not be affected: signal routing by precise perturbations with two different noise levels should work at least equally well, or even better, than in a case where a common noise level of  $\sigma_n = \max(\sigma_n^e, \sigma_n^i)$  is assumed.

#### 6.4.6 Simulating frequency jitter

A rough match of natural frequencies is indeed important for realizing anti-phase sync between X and Y, and bi-stable synchronization of up- and down-stream populations. However, coupled oscillators can tolerate a certain amount of frequency mismatch until (in- or out-of-phase) synchronization breaks down. Stronger couplings allow for larger frequency mismatches, quantified by the width of Arnolds' tongues known from the theory of coupled oscillators (see e.g. [182]). For the case of two coupled gamma oscillators realized in PING networks, this property has been thoroughly quantified in [140].

Actually, since noise introduces frequency jitter in our model we already have a situation in which the momentary frequencies are always different and can change rapidly, but still bi-stability and entrainment persist until a critical noise level. From these considerations one can conclude that our results are robust against moderate mismatches of the natural frequencies of X, Y, and Z. In particular, the strong coupling from X/Y to Z allows for larger natural frequency deviations between up- and down-stream populations before synchronization breaks down. In any case, asymmetries in natural frequencies induce asymmetries in the preferred states, making one of them more stable than the other.

If natural frequencies are different between populations X and Y, a lopsided leader/-follower relationship could emerge, similar to the one reported in [248]. The network as a

whole will still be bistable and allow switching between  $Tr^X$  and  $Tr^Y$  states, by changing which oscillator leads, and which oscillator follows. Alternatively, we could observe X-Y flip between in-phase and anti-phase states. Here the in-phase state was accompanied with a different working frequency than exhibited by the anti-phase state. We speculate that in this case, perturbation control of signal transmission could still be possible but will be more difficult, since it is essential to prevent in-phase synchronization of X and Y. With even larger natural frequency differences, bistability can vanish completely and making switches between two stable states impossible

With respect to Z synchronizing to X or Y, in our specific model setup we have observed state switches going 'forward', i.e. Z briefly speeding up, as well as going 'backward', i.e. Z briefly slowing down, in order to switch its entrainment from X to Y or vice versa. In consequence, when X and Y maintain a 'proper' anti-phase relationship and Z's natural frequency is different from X and Y, it would favor state switches primarily of the appropriate type: always slowing down if its frequency is sufficiently lower, and speeding up if its oscillation frequency is higher.

Apart from our model, in the visual system, it is important to consider two possibilities for how differences between natural frequencies could emerge: First, attending one of two competing stimuli can enhance the neural representation of the attended stimulus relative to the representation of the stimulus that has to be ignored. This enhancement can be accompanied by relative rate and/or gamma frequency increases of up to 4 Hz [29, 183]. On this subject, Fries speculates in his 2015 review "Rhythms for Cognition: Communication through Coherence" that after a theta-rhythm evoked phase reset, the faster gamma rhythm would allow the higher frequency V1 population (representing the attended stimulus) have its first burst of activity arrive to V4 prior to the competing V1 population, triggering a wave of inhibition suppressing the inputs from the slower oscillating inputs. Second, differences between two competing stimuli such as their sizes or contrasts could also lead to natural frequency differences. In fact, we expect stimulus manipulations such as a higher contrast of the non-attended stimulus to compete with attentional mechanisms, which might lead to break-down of routing by synchrony if natural frequency mismatches in favor of the non-attended stimulus are becoming too large.

Part IV

CUMULATIVE OUTLOOK



## OUTLOOK

---

Here, we present the outcome of the research presented in this dissertation, which focused on investigating the routing by synchronization (RBS) mechanism – wherein flexible routing of information during selective attention is performed by having neurons establish coherence between their gamma-rhythmic activities in order to modulate the effective connectivity between them. With the benefit of insight gained throughout performing the investigations, we discuss various challenges that were faced and the possible solutions and new questions to research throughout future experiments.

### 7.1 ANIMAL DATA ANALYSIS

#### 7.1.1 *Laminar ambiguity*

Part II of the dissertation presented a series of analyses on neural recordings collected from areas V1 and V4 processing attended and non-attended visual stimuli. The results showed that stimulus information content encoded within neural activity is linked to its neural activity's gamma cycle, as predicted by the RBS mechanism. One of challenges faced during the investigation was the discovery that the recordings were collected across different layers of the cortical column. Separating the V4 recordings by their laminar location, performed in chapters 3 and 4, was not within the initial plan. After all, the laminar location of the recordings did not affect total amounts of attended versus non-attended information within V4 activity, as presented in Grothe et al 2018 [99]. Moreso, the initial formulation of hypothesis behind the RBS mechanism in 2005 [77] proposed that gamma-rhythmic coherence opens a channel of enhanced information routing between neural populations in both directions – feedforward/bottom-up processing from V1 to V4 as well as the feedback/top-down processing from V4 to V1.

It is only fairly recently that experiments were able to produce evidence that feedforward and feedback communication utilizes distinct frequency channels and occur within distinct layers of the cortical column [15, 158, 225]. This led to a re-evaluation of the RBS mechanism in 2015 [79], wherein intra-areal information routing through gamma-rhythmic coherence is proposed to only be responsible for bottom-up information processing, occurring predominantly within the granular and supragranular (surface) layers of the cortex. In part, these discoveries were made possible through advancing technology – making laminar electrodes accessible, which allowed to record neural activity at multiple depths within a cortical column simultaneously, able to accurately identify the distinct cortical layers.

In our case, with recordings collected with classical single-site electrodes, we were only able to crudely split the available data into surface and deep layer groups. Thus, each group contained recordings from multiple cortical layers, which may have greatly diminished the magnitude of the reported effects. In chapter 3, the analysis on the neural activity within the surface layers of V4 confirmed a detailed hypothesis based on the RBS mechanism, predicting that stimulus information encoded within neural activity is conveyed in gamma-rhythmic packages. As predicted, this effect is particularly strong for the attended stimulus information, and weaker/absent for non-attended sig-

nals. In chapter 4, we perform the same analysis for the deep layer group, to contrast the results with the ones from the surface group. We only had access to a few deep layer recordings from just one animal, which nonetheless produced interesting results – showing that there is, indeed, gamma-rhythmic information coding within the deep layers, however results on stimulus information content modulation by gamma are distinct in comparison to the surface recordings, incoherent with our hypothesis on gamma-rhythmic feedforward information routing. Thus, our results indicate a stark difference between gamma-rhythmic information processing within surface and deep cortical layers, reinforcing previous findings that the different layers perform functionally different computation.

In chapter 5, we analyzed the influence of gamma on stimulus information content within V1 activity, a critical component utilized in our prediction for gamma-rhythmic information coding within V4. Similar to chapter 4, we only had data from one animal. Moreso, our analysis on the laminar location of the recordings revealed that they were not obtained from the surface layers of V1, making it ambiguous whether the data can be used to investigate feedforward information routing. Nonetheless, some of the available V1 recordings provided support that information coding in V1 is gamma-rhythmic. Crucially, unlike the difference between the attention conditions for V4 data, there appeared to be no attention-dependent influence on gamma-rhythmic information coding within V1. Next, by accounting for the attention-dependent coherence between pairings of V1 and V4 recordings, we showed how the gamma-rhythmic packaging of stimulus information within V1 is retained when the information is passed on to V4 for the attended condition when V1 and V4 establish strong coherence in the gamma-frequency range, and lost for the non-attended condition due to a lack of V1-V4 coherence. Cumulatively, the V1 results showed promising support for the RBS mechanism, showing that stimulus information in the output of V1 does occur in gamma-rhythmic packages, and it is the coherence between V1 and V4 rhythms that results in selective routing of attended/non-attended signals. However, due to the ambiguity of the laminar location of the recordings and only having data from one animal, these produced results serve as a pilot study, requiring further investigation to produce a fully comprehensible and consistent outcome.

### 7.1.2 Future research – laminar recordings in V1 and V4

New laminar electrodes are being developed [196], and laminar-resolved animal data is being collected in the Kreiter research group. The experimental setup and selective attention task is primarily the same, keeping the crucial luminance modulation signal superimposed on the visual stimuli, allowing to compute the information content of attended and non-attended signal within neural activity. Ultimately, this will provide an extremely rich data-set, allowing to analyze the influence of rhythmic dynamics on information coding between V1 and V4 in feedforward and feedback directions, the information processing occurring within a cortical column across its different layers, as well as the influence between neighboring V1 populations processing distinct visual stimuli.

First and foremost, the data set will allow to embellish the results from chapter 3 and bring the pilot studies presented in chapters 4 and 5 to fruition. In particular, in order to investigate bottom-up gamma-rhythmic routing of stimulus information between V1 and V4, we are most interested in recordings collected specifically from the output layers of V1 and the input layers of V4. Using such layer-specific recordings should result in

a much cleaner and reliable understanding of the gamma-rhythmic interaction between V1 and V4, as opposed to the results produced from grouping of recordings into broad "surface" and "deep" recordings. The analysis can then be extended across the different layers of a cortical column in order to investigate the effect of inter-columnar dynamics on stimulus information coding. In chapter 4, we uncovered that there is gamma-rhythmic coding of stimulus information in the deep layers of V4, with a qualitatively different pattern compared to the surface layers. Observing how gamma-rhythmic stimulus coding changes throughout the layers would allow to better understand the nature of this effect. Is there a specific source of the gamma-rhythm within the column, entraining other layers, or do the layers produce their own rhythmic activity, establishing complex rhythmic interplay between the layers? Is the gamma-rhythmic information coding within the deep layers merely an echo of the processing within the superficial layers or does it imply a different functional role for gamma in the deep layers? What are the steps leading up to producing the appropriate gamma-rhythmic output from V1 to V4?

### 7.1.3 *Beyond gamma – attention is mediated by multiple rhythms*

This dissertation focused exclusively on gamma, however, the rhythm does not operate alone. A laminar-resolved data set can be utilized in order to explore the functional role and interaction between multiple rhythms active within the visual cortex during selective attention. The other prominent rhythms observed within the visual system during selective attention are the low frequency theta rhythm (4-8Hz) and the intermediate frequency alpha/beta rhythm (8-20Hz).

The theta rhythm has been reported to be tied with gamma via phase-amplitude coupling [29, 30, 44, 236], and has been heavily implicated to be responsible for attentional-sampling through numerous behavioural studies [36, 62, 128, 129, 226]. Attentional sampling, not to be confused with selective attention, is the hypothesis that visual attention might not be a continuous process, but rather explores the different items or different locations of interest within the visual input through rhythmic sampling. In other words, the findings suggest that during feedforward information routing, gamma-rhythmic activity is itself entrained by theta, with periods of higher levels of gamma activity occurring at theta frequency, where each burst of gamma activity represents a period of processing potentially distinct stimuli. Thus, indirectly, by analyzing how stimulus information content depends on gamma amplitude in chapter 3, we have already probed at the influence of theta on stimulus information coding. With the ability to compute stimulus information content within neural activity, a future analysis could investigate whether each theta-coupled burst of gamma activity is indeed processing a new target.

A recent study showed that selective attention reduces theta-rhythmic activity and consequently the phase-amplitude coupling between theta and gamma in V1 and in V4 [207]. Considering that neither firing rates [35, 142] nor the amplitude of gamma-rhythmic activity [29, 34] are reported to be modulated by attention in V1, this attention-dependent effect on theta processes within V1 is particularly interesting. Investigating theta and gamma together would shed light on numerous questions regarding feedforward information routing: What is the functional role of having lower theta levels when processing attended signals? How does this affect the resultant gamma-rhythmic information coding? Does the strong attention-dependent effect on theta activity in V1 affect the attention-dependent gamma-rhythmic coherence between V1 and V4?

Additionally, theta rhythm is particularly prominent within the frontal and parietal areas of the brain, which would ostensibly serve as a source of top-down attentional control [36, 104, 177]. However, the influence of theta between V1 and V4 has been reported to occur primarily in the feedforward direction [207], granted the study was limited to surface recordings of the brain. Future analyses, for instance utilizing new laminar-resolved data from the Kreiter research group, will have the opportunity to expand the investigation across multiple layers of the cortex. What is the profile of theta activity across the different layers of V1 and V4 cortical columns? Where and how does theta exert top-down control over attentional processing?

Regarding top-down control, it is beta-band activity that has been reported to exert feedback influence throughout the visual system within the deep layers of the cortex [15, 34, 168, 193, 225]. Increased attentional demand leads to higher levels of beta activity, accompanied by higher levels of beta-rhythmic coherence between areas. However, unlike the clear phase-amplitude coupling between gamma and theta, experimental results up until this point have not been able to precisely work out how the top-down beta interacts with the other rhythms. As a possible mechanism for the beta-gamma interaction, a modeling study had proposed that neurons participating in beta-rhythmic activity within the deep layers may project to the inhibitory neurons within the superficial layers, enhancing the stimulus driven gamma-rhythm of the local population [132]. A recent experimental study, utilizing an ECOG array to record from areas V1, V4 and parietal area 7a from monkeys performing a selective attention task, reported that attention does lead to enhanced beta-rhythmic coherence from V4/7a to V1, which is then significantly correlated with enhanced gamma-band activity [187]. However, by the nature of the recordings, this result is specific to the surface layers of the cortex. Thus, the nature and the mechanism behind the potential beta-gamma interaction remains enigmatic. A future study could use the laminar-resolved data set from the Kreiter research group to accurately investigate the attention-dependent feedback V4-V1 influence in the deep layers and then how this beta-band activity within the deep layers of V1 influences the rest of the cortical column. How does the feedback beta-band activity in the deep layers affect the routing of stimulus content in the surface layers?

## 7.2 MODELING STIMULATION IN THE VISUAL SYSTEM

### 7.2.1 *Microstimulation relying on inherent network dynamics*

Part III of the dissertation presented a model showcasing RBS-driven information routing between V1 and V4 to investigate a novel closed-loop method of injecting precise stimulation pulses into the neural populations in order to control information flow. Intracortical microstimulation and other methods of providing artificial input to the brain are a useful tool for investigating neural information processing in a causal manner. These techniques can be employed in order to treat cognitive disorders and to produce brain prostheses, helping patients to compensate for disabilities in vision, hearing and touch. In the periphery systems of the brain, the sensory surfaces, devices such as a cochlea [51] or retinal [50] implants have already been successfully deployed. But what about the next stages in the brain? For example, for patients with a damaged optical nerve, an implant must interface with the primary visual cortex directly. Here, one would have to cope with on-going processes, feedback from higher areas, and a strong recurrent coupling – the state of the system. Overriding these processes and directly providing the stimulus in a one to one mapping is difficult and could exert substantial stress to the

tissue, potentially making long-term applications unfeasible [117]. We propose that one should rather try to swim with the tide, using the natural tendencies of the network as far as this is possible.

By performing the investigation, we started to think about the appropriate strategies and methods and tested them on a very simplistic model, replicating the gamma-rhythmic information routing interaction between V1 and V4, akin to the experimental setup from part II. Notably, only the gamma-rhythm was modelled, in order to allow the system to route information via the RBS mechanism. Considering the rhythmic dynamics of the network, using phase response curves (PRCs) and accounting for natural stable states of the system proved to be a viable method in order to control information flow within the system, even when injecting the system with a lot of noise. However, if the goal is to test this approach *in vivo*, it is quite likely that the model is still too simple, failing to account for the complex dynamics observed within the neural populations, e.g. the transient nature of the experimentally observed gamma rhythms, the feedback V4-V1 influence, the interaction between the different rhythms involved in selective attention. How would the PRC stimulation method fare in live subjects?

### 7.2.2 Future research - expanding the model

The activity produced by the model was in the form of a sustained consistent-frequency gamma-rhythm, allowing the effect of a stimulation pulse to linger. However, neural activity data recording from live animals has indicated that gamma-rhythmic activity is usually transient in nature. It's worth to note that the experimental evidence for PRCs is limited to a study that analyzed rhythmic activity within a neural tissue microcircuit *in vitro* [5], and in epileptic rats [229, 230] – all involved recordings with sustained rhythmic activity.

Experimental evidence shows that the transient nature of gamma-rhythmic activity is tied to the theta rhythm through phase-amplitude coupling [236, 237]. The resulting dynamics of the model would necessitate changing the closed-loop stimulation algorithm to account for the short lived nature of bursts of gamma activity. Theoretically, using gamma-rhythm PRCs in order to deliver precise stimulation is still possible, applying a stimulation pulse at the appropriate phase at the beginning of each theta-cycle. However, it is also possible that the theta-rhythm fully subserves gamma, making it impossible to control gamma directly. Rather than trying to establish gamma-rhythmic coherence directly, one could experiment with controlling the theta-rhythm itself. Models on phase-amplitude coupling have been explored for hippocampal circuits, responsible for maintaining working memory [107, 134, 206]. Surprisingly, we are not aware of any modeling studies that have accounted the theta rhythm's influence in the visual system. A recent modeling study did investigate how flexible information routing is achieved through transient gamma-rhythmic coherence, producing a network where gamma-rhythmic activity occurred in bursts [176]. However, the timing of the bursts in the system was not linked to theta. Expanding our model to include theta rhythmic influence would provide insight on the dynamics and functional role of the two rhythms.

The model could also be expanded to include feedback, beta-driven influences in the deep layers. This would open the potential to investigate and interact directly with the top-down attentional control signal. Numerous studies have already produced network models of the visual system, accounting for beta and gamma rhythms [132, 154]. Is there enough experimental evidence available in order to construct a model that accurately recreates the dynamics and mechanisms in the visual cortex? A future modeling

investigation could take inspiration directly from analyses on the laminar data-set that is being collected by the Kreiter research group. In the ideal scenario, the experimental findings from this data set would inform the model, which would aim to reproduce the observed dynamics. Then, the model can be used to make concrete predictions to be tested back in the experimental studies.

### 7.2.3 *Future research - testing state-dependent stimulation in animals*

Researchers have already utilized trains of period stimulation pulses in order to investigate attention-dependent information routing within the visual system [46, 172, 201, 225]. We are not aware of any published research that has investigated the effect of single pulses. However, single stimulation pulses are being activity investigated in the Kreiter research group [58, 61]. Excitingly, preliminary results indicate that the gamma-phase at which a single stimulation pulse is delivered to a population has a significant effect on behaviour [59].

One of the challenges faced in these investigations is the large amounts of recordings that need to be collected in order to acquire a sufficient amount of data for the ensuing analyses. In part, this is due to the small amount of stimulation pulses that can be applied throughout each trial, ensuring that each stimulation pulse is independent of the previous one. This results in acquiring only a few data points from each trial. In order to investigate whether the phase of stimulation has a significant effect, these data points are split into numerous phase-bins, requiring large amounts of data to produce significant results. If one then desires to also account for multiple factors, for instance the phase of stimulation delivery and the strength/phase of gamma-rhythmic coherence between V1 and V4, the data needs to be split even further. Moreso, due to the transient nature of gamma-rhythmic activity, many of the stimulation pulses occur during periods when there is no gamma activity to begin with.

This challenge could be resolved by having the ability to deliver a stimulation pulse corresponding to a desired state of the neural activity. For instance, one could run a session of trials where every single stimulation pulse occurs at the peak of gamma activity, to be compared with unpulsed trials. The current experimental setup does not involve online monitoring of neural activity. Implementing a system that would be capable of analyzing realtime neural activity in order to deliver a stimulation pulse during a period of interest would make for a good future research project [192].

## 7.3 CONCLUSION

The notion that the gamma-rhythmic synchronization of neural activity could be just be an epiphenomenon of the neural circuitry is not without merit [157, 184]. After all – oscillatory dynamics, with and without function, are commonly encountered throughout nature – from planetary systems to vibrating strings to the electromagnetic spectrum to subatomic particles. In neural circuits, oscillatory activity may arise simply due to the interaction between excitatory and inhibitory neurons in order to maintain stable activity output. Attention-dependent information routing could be possible by exclusively modulating the firing rates of sender neurons [109, 148]. However, more and more evidence, including the investigations presented here, is accumulating in support of oscillatory dynamics playing a functional role. This does not mean that any existing

firing-rate based mechanisms are wrong – rather, rhythms and firing rates work together to achieve greater information processing capabilities [4].

In the case of the RBS mechanism – utilizing gamma-rhythmic coherence for information transfer allows for the flexibility necessary to quickly adapt which information is routed through to get processed by higher-up areas, simply by shifting which sender populations establish synchronize with the receiving population. The fact that selective processing is realized by modulating effective connectivity instead of directly modulating the sender's output keeps the unattended bottom-up information active and available, just in case it is needed in the next moment.

Even though our investigations focused specifically on selective attention in the visual cortex, gamma-rhythms between neural populations has been observed throughout the brain, similarly proposed to be responsible for flexible information routing by modulating effective connectivity [40]. Altogether, evidence suggests that the interaction between beta, theta and gamma rhythms may be a canonical functional motif [251], active in different systems of the brain [46, 55, 201] underpinning cognitive functions such as working memory [159], learning [161] and decision making [6]. Understanding the full scope of how these rhythms interact and the mechanisms they subserve will inevitably help resolve many of key questions in neuroscience.



## BIBLIOGRAPHY

---

1. Abbott, L. & Kepler, T. B. in *Statistical Mechanics of Neural Networks* 5–18 (Springer, 1990).
2. Achuthan, S. & Canavier, C. C. Phase-resetting curves determine synchronization, phase locking, and clustering in networks of neural oscillators. *Journal of Neuroscience* **29**, 5218–5233 (2009).
3. Aertsen, A., Gerstein, G., Habib, M. & Palm, G. Dynamics of neuronal firing correlation: modulation of "effective connectivity". *Journal of Neurophysiology* **61**, 900–917 (1989).
4. Ainsworth, M., Lee, S., Cunningham, M. O., Traub, R. D., Kopell, N. J. & Whittington, M. A. Rates and rhythms: a synergistic view of frequency and temporal coding in neuronal networks. *Neuron* **75**, 572–583 (2012).
5. Akam, T., Oren, I., Mantoan, L., Ferenczi, E. & Kullmann, D. M. Oscillatory dynamics in the hippocampus support dentate gyrus–CA3 coupling. *Nature Neuroscience* **15**, 763 (2012).
6. Amemiya, S. & Redish, A. D. Hippocampal theta-gamma coupling reflects state-dependent information processing in decision making. *Cell Reports* **22**, 3328–3338 (2018).
7. Arieli, A., Sterkin, A., Grinvald, A. & Aertsen, A. Dynamics of ongoing activity: explanation of the large variability in evoked cortical responses. *Science* **273**, 1868–1871 (1996).
8. Arons, B. A review of the cocktail party effect. *Journal of the American Voice I/O Society* **12**, 35–50 (1992).
9. Atallah, B. V. & Scanziani, M. Instantaneous Modulation of Gamma Oscillation Frequency by Balancing Excitation with Inhibition. *Neuron* **62**, 566–577 (2009).
10. Azouz, R. & Gray, C. M. Adaptive coincidence detection and dynamic gain control in visual cortical neurons in vivo. *Neuron* **37**, 513–523 (2003).
11. Barry, R. J., Clarke, A. R., Hajos, M., McCarthy, R., Selikowitz, M. & Dupuy, F. E. Resting-state EEG gamma activity in children with attention-deficit/hyperactivity disorder. *Clinical Neurophysiology* **121**, 1871–1877 (2010).
12. Bartos, M., Vida, I., Frotscher, M., Meyer, A., Monyer, H., Geiger, J. R., Jonas, P. & Heidelberg. Fast synaptic inhibition promotes synchronized gamma oscillations in hippocampal interneuron networks. *Proceedings of the National Academy of Sciences of the United States of America* **99**, 13222–13227 (2002).
13. Bartos, M., Vida, I. & Jonas, P. Synaptic mechanisms of synchronized gamma oscillations in inhibitory interneuron networks. *Nature Reviews Neuroscience* **8**, 45–56 (2007).
14. Başar, E. A review of gamma oscillations in healthy subjects and in cognitive impairment. *International Journal of Psychophysiology* **90**, 99–117 (2013).

15. Bastos, A. M., Vezoli, J., Bosman, C. A., Schoffelen, J.-M., Oostenveld, R., Dowdall, J. R., De Weerd, P., Kennedy, H. & Fries, P. Visual areas exert feedforward and feedback influences through distinct frequency channels. *Neuron* **85**, 390–401 (2015).
16. Bédard, C. & Destexhe, A. Modeling local field potentials and their interaction with the extracellular medium. *Handbook of Neural Activity Measurement*, 136–191 (2012).
17. Bédard, C., Kröger, H. & Destexhe, A. Modeling Extracellular Field Potentials and the Frequency-Filtering Properties of Extracellular Space. *Biophysical Journal* **86**, 1829–1842 (2004).
18. Belluscio, M. A., Mizuseki, K., Schmidt, R., Kempter, R. & Buzsáki, G. Cross-frequency phase–phase coupling between theta and gamma oscillations in the hippocampus. *Journal of Neuroscience* **32**, 423–435 (2012).
19. Benabid, A. L., Chabardes, S., Mitrofanis, J. & Pollak, P. Deep brain stimulation of the subthalamic nucleus for the treatment of Parkinson’s disease. *The Lancet Neurology* **8**, 67–81 (2009).
20. Bengio, Y., Lecun, Y. & Hinton, G. Deep learning for AI. *Communications of the ACM* **64**, 58–65 (2021).
21. Berényi, A., Belluscio, M., Mao, D. & Buzsáki, G. Closed-loop control of epilepsy by transcranial electrical stimulation. *Science* **337**, 735–737 (2012).
22. Besserve, M., Lowe, S. C., Logothetis, N. K., Schölkopf, B. & Panzeri, S. Shifts of Gamma Phase across Primary Visual Cortical Sites Reflect Dynamic Stimulus-Modulated Information Transfer. *PLoS Biology* **13**, 1002257 (2015).
23. Bichot, N. P., Rossi, A. F. & Desimone, R. Parallel and serial neural mechanisms for visual search in macaque area V4. *Science* **308**, 529–534 (2005).
24. Blinowska, K. J. & Malinowski, M. Non-linear and linear forecasting of the EEG time series. *Biological Cybernetics* **66**, 159–165 (1991).
25. Boashash, B. Estimating and interpreting the instantaneous frequency of a signal. II. Algorithms and applications. *Proceedings of the IEEE* **80**, 540–568 (1992).
26. Börgers, C., Epstein, S. & Kopell, N. J. Background gamma rhythmicity and attention in cortical local circuits: a computational study. *Proceedings of the National Academy of Sciences* **102**, 7002–7007 (2005).
27. Börgers, C. & Kopell, N. Synchronization in networks of excitatory and inhibitory neurons with sparse, random connectivity. *Neural Computation* **15**, 509–538 (2003).
28. Börgers, C. & Kopell, N. J. Gamma oscillations and stimulus selection. *Neural Computation* **20**, 383–414 (2008).
29. Bosman, C. A., Schoffelen, J. M., Brunet, N., Oostenveld, R., Bastos, A. M., Womelsdorf, T., Rubehn, B., Stieglitz, T., De Weerd, P. & Fries, P. Attentional Stimulus Selection through Selective Synchronization between Monkey Visual Areas. *Neuron* **75**, 875–888 (2012).
30. Bosman, C. A., Womelsdorf, T., Desimone, R. & Fries, P. A microsaccadic rhythm modulates gamma-band synchronization and behavior. *Journal of Neuroscience* **29**, 9471–9480 (2009).
31. Broadbent, D. *Perception and Communication* (1958).

32. Brunel, N. & Latham, P. E. Firing rate of the noisy quadratic integrate-and-fire neuron. *Neural Computation* **15**, 2281–2306 (2003).
33. Brunel, N. & Wang, X.-J. What determines the frequency of fast network oscillations with irregular neural discharges? I. Synaptic dynamics and excitation-inhibition balance. *Journal of Neurophysiology* **90**, 415–430 (2003).
34. Buffalo, E. A., Fries, P., Landman, R., Buschman, T. J. & Desimone, R. Laminar differences in gamma and alpha coherence in the ventral stream. *Proceedings of the National Academy of Sciences* **108**, 11262–11267 (2011).
35. Buffalo, E. A., Fries, P., Landman, R., Liang, H. & Desimone, R. A backward progression of attentional effects in the ventral stream. *Proceedings of the National Academy of Sciences* **107**, 361–365 (2010).
36. Busch, N. A. & VanRullen, R. Spontaneous EEG oscillations reveal periodic sampling of visual attention. *Proceedings of the National Academy of Sciences* **107**, 16048–16053 (2010).
37. Buschman, T. J. & Miller, E. K. Top-down versus bottom-up control of attention in the prefrontal and posterior parietal cortices. *Science* **315**, 1860–1862 (2007).
38. Buzsáki, G., Anastassiou, C. A. & Koch, C. The origin of extracellular fields and currents—EEG, ECoG, LFP and spikes. *Nature reviews neuroscience* **13**, 407–420 (2012).
39. Buzsáki, G. & Draguhn, A. Neuronal oscillations in cortical networks. *Science* **304**, 1926–1929 (2004).
40. Buzsáki, G. & Schomburg, E. W. What does gamma coherence tell us about inter-regional neural communication? *Nature Neuroscience* **18**, 484–489 (2015).
41. Buzsáki, G. & Wang, X.-J. Mechanisms of gamma oscillations. *Annual Review of Neuroscience* **35**, 203–225 (2012).
42. Canavier, C. C. Phase-resetting as a tool of information transmission. *Current Opinion in Neurobiology* **31**, 206–213 (2015).
43. Cannon, J., McCarthy, M. M., Lee, S., Lee, J., Börgers, C., Whittington, M. A. & Kopell, N. Neurosystems: brain rhythms and cognitive processing. *European Journal of Neuroscience* **39**, 705–719 (2014).
44. Canolty, R. T., Edwards, E., Dalal, S. S., Soltani, M., Nagarajan, S. S., Kirsch, H. E., Berger, M. S., Barbaro, N. M. & Knight, R. T. High gamma power is phase-locked to theta oscillations in human neocortex. *Science* **313**, 1626–1628 (2006).
45. Carandini, M. & Heeger, D. J. Normalization as a canonical Neural Computation. *Nature Reviews Neuroscience* **13**, 51–62 (2012).
46. Cardin, J. A., Carlén, M., Meletis, K., Knoblich, U., Zhang, F., Deisseroth, K., Tsai, L. H. & Moore, C. I. Driving fast-spiking cells induces gamma rhythm and controls sensory responses. *Nature* **459**, 663–667 (2009).
47. Carrasco, M. & McElree, B. Covert attention accelerates the rate of visual information processing. *Proceedings of the National Academy of Sciences* **98**, 5363–5367 (2001).
48. Chen, L. L., Madhavan, R., Rapoport, B. I. & Anderson, W. S. Real-time brain oscillation detection and phase-locked stimulation using autoregressive spectral estimation and time-series forward prediction. *IEEE transactions on Biomedical Engineering* **60**, 753–762 (2013).

49. Cherry, E. C. Some experiments on the recognition of speech, with one and with two ears. *The Journal of the Acoustical Society of America* **25**, 975–979 (1953).
50. Chuang, A. T., Margo, C. E. & Greenberg, P. B. Retinal implants: a systematic review. *British Journal of Ophthalmology* **98**, 852–856 (2014).
51. Clark, G. in *Speech Processing in the Auditory System* 422–462 (Springer, 2004).
52. Clayton, M. S., Yeung, N. & Kadosh, R. C. The roles of cortical oscillations in sustained attention. *Trends in Cognitive Sciences* **19**, 188–195 (2015).
53. Coenen, A., Fine, E. & Zayachkivska, O. Adolf Beck: A forgotten pioneer in electroencephalography. *Journal of the History of the Neurosciences* **23**, 276–286 (2014).
54. Delorme, A., Mullen, T., Kothe, C., Akalin Acar, Z., Bigdely-Shamlo, N., Vankov, A. & Makeig, S. EEGLAB, SIFT, NFT, BCILAB, and ERICA: New tools for advanced EEG processing. *Computational Intelligence and Neuroscience* **2011** (2011).
55. Doesburg, S. M., Green, J. J., McDonald, J. J. & Ward, L. M. Theta modulation of inter-regional gamma synchronization during auditory attention control. *Brain Research* **1431**, 77–85 (2012).
56. Douglas, R. J., Martin, K. A. & Whitteridge, D. A canonical microcircuit for neo-cortex. *Neural computation* **1**, 480–488 (1989).
57. Drachman, D. A. *Do we have brain to spare?* 2005.
58. Drebitz, E., Rausch, L.-P. & Kreiter, A. K. A novel approach for removing micro-stimulation artifacts and reconstruction of broad-band neuronal signals. *Journal of Neuroscience Methods* **332**, 108549 (2020).
59. Drebitz, E., Rausch, L.-P. & Kreiter, A. K. *Information processing in monkey's visual cortex is causally dependent on precise gamma-synchronization* in *Proceedings of 14th Göttingen Meeting of the German Neuroscience Society* (2021).
60. Drebitz, E., Schledde, B., Kreiter, A. K. & Wegener, D. Optimizing the yield of multi-unit activity by including the entire spiking activity. *Frontiers in Neuroscience* **13**, 83 (2019).
61. Drebitz, E., Stemmann, H. & Kreiter, A. K. *Effectiveness of electrically evoked input depends on the gamma-phase of the receiving population in monkey area V4* in *Proceedings of 12th Göttingen Meeting of the German Neuroscience Society* (2017).
62. Dugué, L., Marque, P. & VanRullen, R. The phase of ongoing oscillations mediates the causal relation between brain excitation and visual perception. *Journal of Neuroscience* **31**, 11889–11893 (2011).
63. Duncan, J. Selective attention and the organization of visual information. *Journal of Experimental Psychology: General* **113**, 501 (1984).
64. Einevoll, G. T., Kayser, C., Logothetis, N. K. & Panzeri, S. Modelling and analysis of local field potentials for studying the function of cortical circuits. *Nature Reviews Neuroscience* **14**, 770–785 (2013).
65. Engbert, R. & Kliegl, R. Microsaccades uncover the orientation of covert attention. *Vision Research* **43**, 1035–1045 (2003).
66. Engel, A. K., König, P., Gray, C. M. & Singer, W. Stimulus-dependent neuronal oscillations in cat visual cortex: Inter-columnar interaction as determined by cross-correlation analysis. *European Journal of Neuroscience* **2**, 588–606 (1990).

67. Eriksen, C. W. & Hoffman, J. E. Temporal and spatial characteristics of selective encoding from visual displays. *Perception & Psychophysics* **12**, 201–204 (1972).
68. Ermentrout, G. B. & Kopell, N. Fine structure of neural spiking and synchronization in the presence of conduction delays. *Proceedings of the National Academy of Sciences* **95**, 1259–1264 (1998).
69. Fecteau, J. H. & Munoz, D. P. Saliency, relevance, and firing: a priority map for target selection. *Trends in Cognitive Sciences* **10**, 382–390 (2006).
70. Felleman, D. J. & Van Essen, D. C. Distributed hierarchical processing in the primate cerebral cortex. *Cerebral cortex (New York, NY: 1991)* **1**, 1–47 (1991).
71. Fenno, L., Yizhar, O. & Deisseroth, K. The development and application of optogenetics. *Annual Review of Neuroscience* **34** (2011).
72. Fisch, L., Privman, E., Ramot, M., Harel, M., Nir, Y., Kipervasser, S., Andelman, F., Neufeld, M. Y., Kramer, U., Fried, I., *et al.* Neural “ignition”: enhanced activation linked to perceptual awareness in human ventral stream visual cortex. *Neuron* **64**, 562–574 (2009).
73. Fisher, R., Salanova, V., Witt, T., Worth, R., Henry, T., Gross, R., Oommen, K., Osorio, I., Nazzaro, J., Labar, D., *et al.* Electrical stimulation of the anterior nucleus of thalamus for treatment of refractory epilepsy. *Epilepsia* **51**, 899–908 (2010).
74. Fitzgerald, P. J. & Watson, B. O. Gamma oscillations as a biomarker for major depression: an emerging topic. *Translational Psychiatry* **8**, 1–7 (2018).
75. Fourcaud, N. & Brunel, N. Dynamics of the Firing Probability of Noisy Integrate-and-Fire Neurons. *Neural Computation* **14**, 2057–2110 (2002).
76. Fries, P., Reynolds, J. H., Rorie, A. E. & Desimone, R. Modulation of oscillatory neuronal synchronization by selective visual attention. *Science* **291**, 1560–1563 (2001).
77. Fries, P. A mechanism for cognitive dynamics: neuronal communication through neuronal coherence. *Trends in Cognitive Sciences* **9**, 474–480 (2005).
78. Fries, P. Neuronal gamma-band synchronization as a fundamental process in cortical computation. *Annual Review of Neuroscience* **32**, 209–224 (2009).
79. Fries, P. Rhythms for Cognition: Communication through Coherence. *Neuron* **88**, 220–235 (2015).
80. Fries, P., Nikolić, D. & Singer, W. The gamma cycle. *Trends in neurosciences* **30**, 309–316 (2007).
81. Frischen, A., Bayliss, A. P. & Tipper, S. P. Gaze cueing of attention: visual attention, social cognition, and individual differences. *Psychological Bulletin* **133**, 694 (2007).
82. Friston, K. J. Functional and effective connectivity in neuroimaging: a synthesis. *Human Brain Mapping* **2**, 56–78 (1994).
83. Friston, K. J. Functional and effective connectivity: a review. *Brain Connectivity* **1**, 13–36 (2011).
84. Gabriel, S., Lau, R. W. & Gabriel, C. The dielectric properties of biological tissues: III. Parametric models for the dielectric spectrum of tissues. *Physics in Medicine and Biology* **41**, 2271–2293 (1996).

85. Galashan, F. O., Saßen, H. C., Kreiter, A. K. & Wegener, D. Monkey area MT latencies to speed changes depend on attention and correlate with behavioral reaction times. *Neuron* **78**, 740–750 (2013).
86. Gandal, M. J., Edgar, J. C., Klook, K. & Siegel, S. J. Gamma synchrony: towards a translational biomarker for the treatment-resistant symptoms of schizophrenia. *Neuropharmacology* **62**, 1504–1518 (2012).
87. Geisler, C., Brunel, N. & Wang, X.-J. Contributions of intrinsic membrane dynamics to fast network oscillations with irregular neuronal discharges. *Journal of Neurophysiology* **94**, 4344–4361 (2005).
88. Gennari, F. De Peculiari Structura Cerebri Parma Ex Regio Typographeo (1782).
89. Gerstein, G. L. & Perkel, D. H. Simultaneously recorded trains of action potentials: analysis and functional interpretation. *Science* **164**, 828–830 (1969).
90. Gieselmann, M. & Thiele, A. Comparison of spatial integration and surround suppression characteristics in spiking activity and the local field potential in macaque V1. *European Journal of Neuroscience* **28**, 447–459 (2008).
91. Gilbert, C. D. & Wiesel, T. N. Receptive field dynamics in adult primary visual cortex. *Nature* **356**, 150–152 (1992).
92. Givre, S. J., Schroeder, C. E. & Arezzo, J. C. Contribution of extrastriate area V4 to the surface-recorded flash VEP in the awake macaque. *Vision Research* **34**, 415–428 (1994).
93. Glickstein, M. & Rizzolatti, G. Francesco Gennari and the structure of the cerebral cortex. *Trends in Neurosciences* **7**, 464–467 (1984).
94. Gloor, P. Neuronal generators and the problem of localization in electroencephalography: application of volume conductor theory to electroencephalography. *Journal of Clinical Neurophysiology* **2**, 327–354 (1985).
95. Goertzel, B. Artificial general intelligence: concept, state of the art, and future prospects. *Journal of Artificial General Intelligence* **5**, 1 (2014).
96. Gray, C. M., König, P., Engel, A. K. & Singer, W. Oscillatory responses in cat visual cortex exhibit inter-columnar synchronization which reflects global stimulus properties. *Nature* **338**, 334–337 (1989).
97. Gregoriou, G. G., Gotts, S. J., Zhou, H. & Desimone, R. High-Frequency, long-range coupling between prefrontal and visual cortex during attention. *Science* **324**, 1207–1210 (2009).
98. Grothe, I., Neitzel, S. D., Mandon, S. & Kreiter, A. K. Switching neuronal inputs by differential modulations of gamma-band phase-coherence. *Journal of Neuroscience* **32**, 16172–16180 (2012).
99. Grothe, I., Rotermund, D., Neitzel, S. D., Mandon, S., Ernst, U. A., Kreiter, A. K. & Pawelzik, K. R. Attention selectively gates afferent signal transmission to area V4. *Journal of Neuroscience* **38**, 3441–3452 (2018).
100. Guevara Erra, R., Perez Velazquez, J. L. & Rosenblum, M. Neural Synchronization from the Perspective of Non-linear Dynamics. *Frontiers in Computational Neuroscience* **11**, 98 (2017).
101. Haider, B., Schulz, D. P., Häusser, M. & Carandini, M. Millisecond coupling of local field potentials to synaptic currents in the awake visual cortex. *Neuron* **90**, 35–42 (2016).

102. Harnack, D., Ernst, U. A. & Pawelzik, K. R. A model for attentional information routing through coherence predicts biased competition and multistable perception. *Journal of Neurophysiology* **114**, 1593–1605 (2015).
103. Harris, K. D. & Mrsic-Flogel, T. D. Cortical connectivity and sensory coding. *Nature* **503**, 51–58 (2013).
104. Hawellek, D. J., Wong, Y. T. & Pesaran, B. Temporal coding of reward-guided choice in the posterior parietal cortex. *Proceedings of the National Academy of Sciences* **113**, 13492–13497 (2016).
105. Herculano-Houzel, S. The human brain in numbers: a linearly scaled-up primate brain. *Frontiers in Human Neuroscience* **3**, 31 (2009).
106. Herculano-Houzel, S., Munk, M. H., Neuenschwander, S. & Singer, W. Precisely synchronized oscillatory firing patterns require electroencephalographic activation. *Journal of Neuroscience* **19**, 3992–4010 (1999).
107. Herman, P. A., Lundqvist, M. & Lansner, A. Nested theta to gamma oscillations and precise spatiotemporal firing during memory retrieval in a simulated attractor network. *Brain Research* **1536**, 68–87 (2013).
108. Hinton, G., Deng, L., Yu, D., Dahl, G. E., Mohamed, A.-r., Jaitly, N., Senior, A., Vanhoucke, V., Nguyen, P., Sainath, T. N., *et al.* Deep neural networks for acoustic modeling in speech recognition: The shared views of four research groups. *IEEE Signal Processing Magazine* **29**, 82–97 (2012).
109. Histed, M. H. & Maunsell, J. H. Cortical neural populations can guide behavior by integrating inputs linearly, independent of synchrony. *Proceedings of the National Academy of Sciences* **111**, E178–E187 (2014).
110. Hodgkin, A. L. & Huxley, A. F. A quantitative description of membrane current and its application to conduction and excitation in nerve. *The Journal of Physiology* **117**, 500–544 (1952).
111. Hodgkin, A. L., Huxley, A. F. & Katz, B. Measurement of current-voltage relations in the membrane of the giant axon of *Loligo*. *The Journal of Physiology* **116**, 424–448 (1952).
112. Hodgkin, A. L. & Huxley, A. F. Currents carried by sodium and potassium ions through the membrane of the giant axon of *Loligo*. *The Journal of Physiology* **116**, 449–472 (1952).
113. Hodgkin, A. L. & Huxley, A. F. The components of membrane conductance in the giant axon of *Loligo*. *The Journal of Physiology* **116**, 473–496 (1952).
114. Hughes, J. R. in *International Review of Neurobiology* 99–152 (Elsevier, 1964).
115. Jia, X., Tanabe, S. & Kohn, A. Gamma and the coordination of spiking activity in early visual cortex. *Neuron* **77**, 762–774 (2013).
116. Jia, X., Xing, D. & Kohn, A. No consistent relationship between gamma power and peak frequency in macaque primary visual cortex. *Journal of Neuroscience* **33**, 17–25 (2013).
117. Johnson, A., Klassen, G., McGregor, M. & Dobell, A. Long-term electrical stimulation of the heart in Stokes-Adams disease. *Canadian Medical Association journal* **89**, 683 (1963).

118. Jung, R. & Berger, W. Fiftieth anniversary of Hans Berger's publication of the electroencephalogram. His first records in 1924–1931 (author's transl). *Archiv fur Psychiatrie und Nervenkrankheiten* **227**, 279–300 (1979).
119. Kandel, E. R., Schwartz, J. H., Jessell, T. M., Siegelbaum, S. & Hudspeth, A. J. *Principles of Neural Science. 5th edition* (McGraw-Hill New York, 2013).
120. Kaspar, K. & König, P. Overt attention and context factors: the impact of repeated presentations, image type, and individual motivation. *PloS One* **6**, e21719 (2011).
121. Kopell, N. & Ermentrout, G. B. Mechanisms of phase-locking and frequency control in pairs of coupled neural oscillators. *Handbook of Dynamical Systems* **2**, 3–54 (2002).
122. Kreiter, A. K. How do we model attention-dependent signal routing? *Neural Networks* **19**, 1443–1444 (2006).
123. Kreiter, A. K. Synchrony, flexible network configuration and linking neural events to behavior. *Current Opinion in Physiology* (2020).
124. Kreiter, A. K. & Singer, W. Stimulus-dependent synchronization of neuronal responses in the visual cortex of the awake macaque monkey. *Journal of Neuroscience* **16**, 2381–2396 (1996).
125. Krizhevsky, A., Sutskever, I. & Hinton, G. E. Imagenet classification with deep convolutional neural networks. *Advances in Neural Information Processing Systems* **25**, 1097–1105 (2012).
126. Kusunoki, M., Gottlieb, J. & Goldberg, M. E. The lateral intraparietal area as a salience map: the representation of abrupt onset, stimulus motion, and task relevance. *Vision Research* **40**, 1459–1468 (2000).
127. Kwon, J. S., O'Donnell, B. F., Wallenstein, G. V., Greene, R. W., Hirayasu, Y., Nestor, P. G., Hasselmo, M. E., Potts, G. F., Shenton, M. E. & McCarley, R. W. Gamma frequency-range abnormalities to auditory stimulation in schizophrenia. *Archives of General Psychiatry* **56**, 1001–1005 (1999).
128. Landau, A. N. & Fries, P. Attention samples stimuli rhythmically. *Current Biology* **22**, 1000–1004 (2012).
129. Landau, A. N., Schreyer, H. M., Van Pelt, S. & Fries, P. Distributed attention is implemented through theta-rhythmic gamma modulation. *Current Biology* **25**, 2332–2337 (2015).
130. Lavie, N. Perceptual load as a necessary condition for selective attention. *Journal of Experimental Psychology: Human Perception and Performance* **21**, 451 (1995).
131. Lee, J. & Maunsell, J. H. Attentional modulation of MT neurons with single or multiple stimuli in their receptive fields. *Journal of Neuroscience* **30**, 3058–3066 (2010).
132. Lee, J. H., Whittington, M. A. & Kopell, N. J. Top-down beta rhythms support selective attention via interlaminar interaction: a model. *PLoS Computational Biology* **9**, e1003164 (2013).
133. Lee, K.-H., Williams, L. M., Breakspear, M. & Gordon, E. Synchronous gamma activity: a review and contribution to an integrative neuroscience model of schizophrenia. *Brain Research Reviews* **41**, 57–78 (2003).
134. Lega, B., Burke, J., Jacobs, J. & Kahana, M. J. Slow-theta-to-gamma phase–amplitude coupling in human hippocampus supports the formation of new episodic memories. *Cerebral Cortex* **26**, 268–278 (2016).

135. Lenz, D., Krauel, K., Schadow, J., Baving, L., Duzel, E. & Herrmann, C. S. Enhanced gamma-band activity in ADHD patients lacks correlation with memory performance found in healthy children. *Brain Research* **1235**, 117–132 (2008).
136. Leopold, D. A. & Logothetis, N. K. Microsaccades differentially modulate neural activity in the striate and extrastriate visual cortex. *Experimental Brain Research* **123**, 341–345 (1998).
137. Liu, T.-Y., Hsieh, J.-C., Chen, Y.-S., Tu, P.-C., Su, T.-P. & Chen, L.-F. Different patterns of abnormal gamma oscillatory activity in unipolar and bipolar disorder patients during an implicit emotion task. *Neuropsychologia* **50**, 1514–1520 (2012).
138. Logothetis, N. K., Augath, M., Murayama, Y., Rauch, A., Sultan, F., Goense, J., Oeltermann, A. & Merkle, H. The effects of electrical microstimulation on cortical signal propagation. *Nature Neuroscience* **13**, 1283 (2010).
139. Lowery, A. J. *Introducing the monash vision group's cortical prosthesis in 2013 IEEE International Conference on Image Processing* (2013), 1536–1539.
140. Lowet, E., Roberts, M., Hadjipapas, A., Peter, A., van der Eerden, J. & De Weerd, P. Input-dependent frequency modulation of cortical gamma oscillations shapes spatial synchronization and enables phase coding. *PLoS Computational Biology* **11**, e1004072 (2015).
141. Lozano, A. M., Fosdick, L., Chakravarty, M. M., Leoutsakos, J.-M., Munro, C., Oh, E., Drake, K. E., Lyman, C. H., Rosenberg, P. B., Anderson, W. S., *et al.* A phase II study of fornix deep brain stimulation in mild Alzheimer's disease. *Journal of Alzheimer's Disease* **54**, 777–787 (2016).
142. Luck, S. J., Chelazzi, L., Hillyard, S. A. & Desimone, R. Neural mechanisms of spatial selective attention in areas V1, V2, and V4 of macaque visual cortex. *Journal of Neurophysiology* **77**, 24–42 (1997).
143. Mably, A. J. & Colgin, L. L. Gamma oscillations in cognitive disorders. *Current Opinion in Neurobiology* **52**, 182–187 (2018).
144. Maris, E. & Oostenveld, R. Nonparametric statistical testing of EEG- and MEG-data. *Journal of Neuroscience Methods* **164**, 177–190 (2007).
145. Markov, N. T., Vezoli, J., Chameau, P., Falchier, A., Quilodran, R., Huissoud, C., Lamy, C., Misery, P., Giroud, P., Ullman, S., *et al.* Anatomy of hierarchy: feed-forward and feedback pathways in macaque visual cortex. *Journal of Comparative Neurology* **522**, 225–259 (2014).
146. Martin, J. L. R., Barbanj, M. J., Schlaepfer, T. E., Thompson, E., Pérez, V. & Kulishevsky, J. Repetitive transcranial magnetic stimulation for the treatment of depression: systematic review and meta-analysis. *The British Journal of Psychiatry* **182**, 480–491 (2003).
147. Martin-Vazquez, G., Makarova, J., Makarov, V. A. & Herreras, O. Determining the true polarity and amplitude of synaptic currents underlying gamma oscillations of local field potentials. *PLoS One* **8** (2013).
148. Maunsell, J. H. Neuronal mechanisms of visual attention. *Annual Review of Vision Science* **1**, 373–391 (2015).
149. McAdams, C. J. & Maunsell, J. H. Effects of attention on orientation-tuning functions of single neurons in macaque cortical area V4. *Journal of Neuroscience* **19**, 431–441 (1999).

150. McFarland, D. J. & Wolpaw, J. R. Sensorimotor rhythm-based brain–computer interface (BCI): model order selection for autoregressive spectral analysis. *Journal of Neural Engineering* **5**, 155 (2008).
151. McIntosh, R. D. & Schenk, T. Two visual streams for perception and action: current trends. (2009).
152. McLelland, D. & VanRullen, R. Theta-gamma coding meets communication-through-coherence: neuronal oscillatory multiplexing theories reconciled. *PLoS Computational Biology* **12** (2016).
153. Mehta, A. D., Ulbert, I. & Schroeder, C. E. Intermodal selective attention in monkeys. I: distribution and timing of effects across visual areas. *Cerebral Cortex* **10**, 343–358 (2000).
154. Mejias, J. F., Murray, J. D., Kennedy, H. & Wang, X. J. Feedforward and feedback frequency-dependent interactions in a large-scale laminar network of the primate cortex. *Science Advances* **2**, e1601335 (2016).
155. Melcher, D., Papathomas, T. V. & Vidnyánszky, Z. Implicit attentional selection of bound visual features. *Neuron* **46**, 723–729 (2005).
156. Merel, J., Botvinick, M. & Wayne, G. Hierarchical motor control in mammals and machines. *Nature Communications* **10**, 1–12 (2019).
157. Merker, B. Cortical gamma oscillations: the functional key is activation, not cognition. *Neuroscience & Biobehavioral Reviews* **37**, 401–417 (2013).
158. Michalareas, G., Vezoli, J., Van Pelt, S., Schoffelen, J.-M., Kennedy, H. & Fries, P. Alpha-beta and gamma rhythms subserve feedback and feedforward influences among human visual cortical areas. *Neuron* **89**, 384–397 (2016).
159. Miller, E. K., Lundqvist, M. & Bastos, A. M. Working Memory 2.0. *Neuron* **100**, 463–475 (2018).
160. Milner, P. M. A model for visual shape recognition. *Psychological Review* **81**, 521 (1974).
161. Miltner, W. H., Braun, C., Arnold, M., Witte, H. & Taub, E. Coherence of gamma-band EEG activity as a basis for associative learning. *Nature* **397**, 434–436 (1999).
162. Mitchell, J. F., Sundberg, K. A. & Reynolds, J. H. Spatial attention decorrelates intrinsic activity fluctuations in macaque area V4. *Neuron* **63**, 879–888 (2009).
163. Moran, J. & Desimone, R. Selective attention gates visual processing in the extrastriate cortex. *Science* **229**, 782–784 (1985).
164. Mortezapouraghdam, Z., Corona-Strauss, F. I., Takahashi, K. & Strauss, D. J. Reducing the Effect of Spurious Phase Variations in Neural Oscillatory Signals. *Frontiers in Computational Neuroscience* **12**, 82 (2018).
165. Motter, B. C. Focal attention produces spatially selective processing in visual cortical areas V1, V2, and V4 in the presence of competing stimuli. *Journal of Neurophysiology* **70**, 909–919 (1993).
166. Mountcastle, V. B. The columnar organization of the neocortex. *Brain: A Journal of Neurology* **120**, 701–722 (1997).
167. Munk, M. H., Roelfsema, P. R., König, P., Engel, A. K. & Singer, W. Role of reticular activation in the modulation of intracortical synchronization. *Science* **272**, 271–274 (1996).

168. Nandy, A. S., Nassi, J. J. & Reynolds, J. H. Laminar organization of attentional modulation in macaque visual area V4. *Neuron* **93**, 235–246 (2017).
169. Nelson, M. J., Pouget, P., Nilsen, E. A., Patten, C. D. & Schall, J. D. Review of signal distortion through metal microelectrode recording circuits and filters. *Journal of Neuroscience Methods* **169**, 141–157 (2008).
170. Netoff, T., Schwemmer, M. A. & Lewis, T. J. in *Phase Response Curves in Neuroscience* 95–129 (Springer, 2012).
171. Nho, W. & Loughlin, P. J. When is instantaneous frequency the average frequency at each time? *IEEE Signal Processing Letters* **6**, 78–80 (1999).
172. Ni, J., Wunderle, T., Lewis, C. M., Desimone, R., Diester, I. & Fries, P. Gamma-Rhythmic Gain Modulation. *Neuron* **92**, 240–251 (2016).
173. Niedermeyer, E. Dipole theory and electroencephalography. *Clinical Electroencephalography* **27**, 121–131 (1996).
174. Oathes, D. J., Ray, W. J., Yamasaki, A. S., Borkovec, T. D., Castonguay, L. G., Newman, M. G. & Nitschke, J. Worry, generalized anxiety disorder, and emotion: Evidence from the EEG gamma band. *Biological Psychology* **79**, 165–170 (2008).
175. Packer, A. M. & Yuste, R. Dense, unspecific connectivity of neocortical parvalbumin-positive interneurons: a canonical microcircuit for inhibition? *Journal of Neuroscience* **31**, 13260–13271 (2011).
176. Palmigiano, A., Geisel, T., Wolf, F. & Battaglia, D. Flexible information routing by transient synchrony. *Nature Neuroscience* **20**, 1014–1022 (2017).
177. Phillips, J. M., Vinck, M., Everling, S. & Womelsdorf, T. A long-range frontoparietal 5-to 10-Hz network predicts “top-down” controlled guidance in a task-switch paradigm. *Cerebral Cortex* **24**, 1996–2008 (2014).
178. Plonsey, R. Bioelectric phenomena. *Wiley Encyclopedia of Electrical and Electronics Engineering* (2001).
179. Posner, M. I., Petersen, S. E., Fox, P. T. & Raichle, M. E. Localization of cognitive operations in the human brain. *Science* **240**, 1627–1631 (1988).
180. Prinz, A. A., Thirumalai, V. & Marder, E. The functional consequences of changes in the strength and duration of synaptic inputs to oscillatory neurons. *Journal of Neuroscience* **23**, 943–954 (2003).
181. Purves, D., Augustine, G. J., Fitzpatrick, D., Hall, W. C., LaMantia, A., Mooney, R. D., Platt, M. L. & White, L. *Neuroscience* (Oxford University Press, 2017).
182. Rasband, S. N. *Chaotic dynamics of nonlinear systems* 130–131 (Courier Dover Publications, 2015).
183. Ray, S. & Maunsell, J. H. Differences in gamma frequencies across visual cortex restrict their possible use in computation. *Neuron* **67**, 885–896 (2010).
184. Ray, S. & Maunsell, J. H. Do gamma oscillations play a role in cerebral cortex? *Trends in Cognitive Sciences* **19**, 78–85 (2015).
185. Reynolds, J. H., Chelazzi, L. & Desimone, R. Competitive mechanisms subserve attention in macaque areas V2 and V4. *Journal of Neuroscience* **19**, 1736–1753 (1999).
186. Reynolds, J. H. & Desimone, R. Interacting roles of attention and visual salience in V4. *Neuron* **37**, 853–863 (2003).

187. Richter, C. G., Thompson, W. H., Bosman, C. A. & Fries, P. Top-down beta enhances bottom-up gamma. *Journal of Neuroscience* **37**, 6698–6711 (2017).
188. Roberts, M. J., Lowet, E., Brunet, N. M., Ter Wal, M., Tiesinga, P., Fries, P. & De Weerd, P. Robust gamma coherence between macaque V1 and V2 by dynamic frequency matching. *Neuron* **78**, 523–536 (2013).
189. Roelfsema, P. R., Engel, A. K., König, P. & Singer, W. Visuomotor integration is associated with zero time-lag synchronization among cortical areas. *Nature* **385**, 157–161 (1997).
190. Roelfsema, P. R., Lamme, V. A. & Spekreijse, H. Object-based attention in the primary visual cortex of the macaque monkey. *Nature* **395**, 376–381 (1998).
191. Rohenkohl, G., Bosman, C. A. & Fries, P. Gamma Synchronization between V1 and V4 Improves Behavioral Performance. *Neuron* **100**, 953–963.e3 (2018).
192. Rotermund, D., Ernst, U. A. & Pawelzik, K. R. Open Hardware for neuro-prosthesis research: A study about a closed-loop multi-channel system for electrical surface stimulations and measurements. *HardwareX* **6**, e00078 (2019).
193. Saalmann, Y. B., Pinsk, M. A., Wang, L., Li, X. & Kastner, S. The pulvinar regulates information transmission between cortical areas based on attention demands. *Science* **337**, 753–756 (2012).
194. Salinas, E. & Sejnowski, T. J. Impact of correlated synaptic input on output firing rate and variability in simple neuronal models. *Journal of Neuroscience* **20**, 6193–6209 (2000).
195. Salkoff, D. B., Zagha, E., Yüzgeç, Ö. & McCormick, D. A. Synaptic mechanisms of tight spike synchrony at gamma frequency in cerebral cortex. *Journal of Neuroscience* **35**, 10236–10251 (2015).
196. Schander, A., Stemmann, H., Tolstosheeva, E., Roese, R., Biefeld, V., Kempen, L., Kreiter, A. & Lang, W. Design and fabrication of novel multi-channel floating neural probes for intracortical chronic recording. *Sensors and Actuators A: Physical* **247**, 125–135 (2016).
197. Schroeder, C. E., Mehta, A. D. & Givre, S. J. A spatiotemporal profile of visual system activation revealed by current source density analysis in the awake macaque. *Cerebral Cortex (New York, NY: 1991)* **8**, 575–592 (1998).
198. Schultheiss, N. W., Prinz, A. A. & Butera, R. J. *Phase response curves in neuroscience: theory, experiment, and analysis* (Springer Science & Business Media, 2011).
199. Senova, S., Chaillet, A. & Lozano, A. M. Fornical closed-loop stimulation for Alzheimer's disease. *Trends in Neurosciences* **41**, 418–428 (2018).
200. Shadlen, M. N. & Movshon, J. A. Synchrony unbound: a critical evaluation of the temporal binding hypothesis. *Neuron* **24**, 67–77 (1999).
201. Siegle, J. H., Pritchett, D. L. & Moore, C. I. Gamma-range synchronization of fast-spiking interneurons can enhance detection of tactile stimuli. *Nature Neuroscience* **17**, 1371–1379 (2014).
202. Silver, D., Huang, A., Maddison, C. J., Guez, A., Sifre, L., Van Den Driessche, G., Schrittwieser, J., Antonoglou, I., Panneershelvam, V., Lanctot, M., *et al.* Mastering the game of Go with deep neural networks and tree search. *Nature* **529**, 484–489 (2016).

203. Silver, D., Hubert, T., Schrittwieser, J., Antonoglou, I., Lai, M., Guez, A., Lanctot, M., Sifre, L., Kumaran, D., Graepel, T., *et al.* A general reinforcement learning algorithm that masters chess, shogi, and Go through self-play. *Science* **362**, 1140–1144 (2018).
204. Singer, W. Binding by synchrony. *Scholarpedia* **2**. revision #124403, 1657 (2007).
205. Smeal, R. M., Ermentrout, G. B. & White, J. A. Phase-response curves and synchronized neural networks. *Philosophical Transactions of the Royal Society of London B: Biological Sciences* **365**, 2407–2422 (2010).
206. Sotero, R. C. Modeling the generation of phase-amplitude coupling in cortical circuits: From detailed networks to neural mass models. *BioMed research international* **2015** (2015).
207. Spyropoulos, G., Bosman, C. A. & Fries, P. A theta rhythm in macaque visual cortex and its attentional modulation. *Proceedings of the National Academy of Sciences*, 201719433 (2018).
208. Stam, C. J., van Walsum, A. M. v. C., Pijnenburg, Y. A., Berendse, H. W., de Munck, J. C., Scheltens, P. & van Dijk, B. W. Generalized synchronization of MEG recordings in Alzheimer's disease: evidence for involvement of the gamma band. *Journal of Clinical Neurophysiology* **19**, 562–574 (2002).
209. Steinmetz, P. N., Roy, A., Fitzgerald, P. J., Hsiao, S. S., Johnson, K. O. & Niebur, E. Attention modulates synchronized neuronal firing in primate somatosensory cortex. *Nature* **404**, 187–190 (2000).
210. Stepanyants, A., Martinez, L. M., Ferecskó, A. S. & Kisvárdy, Z. F. The fractions of short-and long-range connections in the visual cortex. *Proceedings of the National Academy of Sciences* **106**, 3555–3560 (2009).
211. Stettler, D. D., Das, A., Bennett, J. & Gilbert, C. D. Lateral connectivity and contextual interactions in macaque primary visual cortex. *Neuron* **36**, 739–750 (2002).
212. Strata, P. & Harvey, R. Dale's principle. *Brain Research Bulletin* **50**, 349–350 (1999).
213. Taylor, K., Mandon, S., Freiwald, W. A. & Kreiter, A. K. Coherent oscillatory activity in monkey area v4 predicts successful allocation of attention. *Cerebral Cortex* **15**, 1424–1437 (2005).
214. Tehovnik, E., Tolias, A., Sultan, F., Slocum, W. & Logothetis, N. Direct and indirect activation of cortical neurons by electrical microstimulation. *Journal of Neurophysiology* **96**, 512–521 (2006).
215. Thiele, A. & Stoner, G. Neuronal synchrony does not correlate with motion coherence in cortical area MT. *Nature* **421**, 366–370 (2003).
216. Thompson, K. G. & Bichot, N. P. A visual salience map in the primate frontal eye field. *Progress in Brain Research* **147**, 249–262 (2005).
217. Tiesinga, P. & Sejnowski, T. J. Cortical Enlightenment: Are Attentional Gamma Oscillations Driven by ING or PING? *Neuron* **63**, 727–732 (2009).
218. Träschütz, A., Kreiter, A. K. & Wegener, D. Transient activity in monkey area MT represents speed changes and is correlated with human behavioral performance. *Journal of Neurophysiology* **113**, 890–903 (2015).
219. Treisman, A. M. Selective attention in man. *British Medical Bulletin* **20**, 12–16 (1964).

220. Treue, S. & Maunsell, J. H. Attentional modulation of visual motion processing in cortical areas MT and MST. *Nature* **382**, 539–541 (1996).
221. Tsodyks, M., Kenet, T., Grinvald, A. & Arieli, A. Linking spontaneous activity of single cortical neurons and the underlying functional architecture. *Science* **286**, 1943–1946 (1999).
222. Uhlhaas, P. J. & Singer, W. Neural Synchrony in Brain Disorders: Relevance for Cognitive Dysfunctions and Pathophysiology. *Neuron* **52**, 155–168 (2006).
223. Van Deursen, J., Vuurman, E., Verhey, F., van Kranen-Mastenbroek, V. & Riedel, W. Increased EEG gamma band activity in Alzheimer’s disease and mild cognitive impairment. *Journal of Neural Transmission* **115**, 1301–1311 (2008).
224. Van Essen, D. C. & Maunsell, J. H. Hierarchical organization and functional streams in the visual cortex. *Trends in Neurosciences* **6**, 370–375 (1983).
225. Van Kerkoerle, T., Self, M. W., Dagnino, B., Gariel-Mathis, M. A., Poort, J., Van Der Togt, C. & Roelfsema, P. R. Alpha and gamma oscillations characterize feedback and feedforward processing in monkey visual cortex. *Proceedings of the National Academy of Sciences of the United States of America* **111**, 14332–14341 (2014).
226. VanRullen, R. Visual attention: a rhythmic process? *Current Biology* **23**, R1110–R1112 (2013).
227. VanRullen, R. Perceptual cycles. *Trends in Cognitive Sciences* **20**, 723–735 (2016).
228. Vaswani, A., Shazeer, N., Parmar, N., Uszkoreit, J., Jones, L., Gomez, A. N., Kaiser, Ł. & Polosukhin, I. *Attention is all you need* in *Advances in neural information processing systems* (2017), 5998–6008.
229. Velazquez, J. P., Erra, R. G. & Rosenblum, M. The epileptic thalamocortical network is a macroscopic self-sustained oscillator: evidence from frequency-locking experiments in rat brains. *Scientific Reports* **5**, 8423 (2015).
230. Velazquez, J. P., Galan, R., Dominguez, L. G., Leshchenko, Y., Lo, S., Belkas, J. & Erra, R. G. Phase response curves in the characterization of epileptiform activity. *Physical Review E* **76**, 061912 (2007).
231. Vinck, M., Lima, B., Womelsdorf, T., Oostenveld, R., Singer, W., Neuenschwander, S. & Fries, P. Gamma-phase shifting in awake monkey visual cortex. *Journal of Neuroscience* **30**, 1250–1257 (2010).
232. Vinck, M., Womelsdorf, T., Buffalo, E. A., Desimone, R. & Fries, P. Attentional Modulation of Cell-Class-Specific Gamma-Band Synchronization in Awake Monkey Area V4. *Neuron* **80**, 1077–1089 (2013).
233. Vodenicarevic, D., Locatelli, N., Grollier, J. & Querlioz, D. Nano-oscillator-based classification with a machine learning-compatible architecture. *Journal of Applied Physics* **124**, 152117 (2018).
234. Vodenicarevic, D., Locatelli, N. & Querlioz, D. *A neural network based on synchronized pairs of nano-oscillators* in *2017 IEEE 17th International Conference on Nanotechnology (IEEE-NANO)* (2017), 512–514.
235. Vogels, T. P., Sprekeler, H., Zenke, F., Clopath, C. & Gerstner, W. Inhibitory plasticity balances excitation and inhibition in sensory pathways and memory networks. *Science* **334**, 1569–1573 (2011).

236. Voloh, B., Valiante, T. A., Everling, S. & Womelsdorf, T. Theta–gamma coordination between anterior cingulate and prefrontal cortex indexes correct attention shifts. *Proceedings of the National Academy of Sciences* **112**, 8457–8462 (2015).
237. Voloh, B. & Womelsdorf, T. A role of phase-resetting in coordinating large scale neural networks during attention and goal-directed behavior. *Frontiers in Systems Neuroscience* **10**, 18 (2016).
238. Von Helmholtz, H. *Handbuch der physiologischen Optik: mit 213 in den Text eingedruckten Holzschnitten und 11 Tafeln* (Voss, 1867).
239. Von Helmholtz, H. *Helmholtz's treatise on physiological optics* (Optical Society of America, 1925).
240. Wang, X.-J. & Buzsáki, G. Gamma oscillation by synaptic inhibition in a hippocampal interneuronal network model. *Journal of Neuroscience* **16**, 6402–6413 (1996).
241. Weinberger, M., Hutchison, W. D., Lozano, A. M., Hodaie, M. & Dostrovsky, J. O. Increased gamma oscillatory activity in the subthalamic nucleus during tremor in Parkinson's disease patients. *Journal of Neurophysiology* **101**, 789–802 (2009).
242. Wessinger, C., VanMeter, J., Tian, B., Van Lare, J., Pekar, J. & Rauschecker, J. P. Hierarchical organization of the human auditory cortex revealed by functional magnetic resonance imaging. *Journal of Cognitive Neuroscience* **13**, 1–7 (2001).
243. Wheeler, J. A. Information, physics, quantum: The search for links. *Complexity, Entropy, and the Physics of Information* **8** (1990).
244. Whittington, M. A., Cunningham, M. O., LeBeau, F. E., Racca, C. & Traub, R. D. Multiple origins of the cortical gamma rhythm. *Developmental Neurobiology* **71**, 92–106 (2011).
245. Whittington, M. A., Traub, R., Kopell, N., Ermentrout, B. & Buhl, E. Inhibition-based rhythms: experimental and mathematical observations on network dynamics. *International Journal of Psychophysiology* **38**, 315–336 (2000).
246. Whittington, M. A., Traub, R. D. & Jefferys, J. G. Synchronized oscillations in interneuron networks driven by metabotropic glutamate receptor activation. *Nature* **373**, 612 (1995).
247. Wilson, H. R. & Cowan, J. D. Excitatory and inhibitory interactions in localized populations of model neurons. *Biophysical Journal* **12**, 1–24 (1972).
248. Witt, A., Palmigiano, A., Neef, A., El Hady, A., Wolf, F. & Battaglia, D. Controlling the oscillation phase through precisely timed closed-loop optogenetic stimulation: a computational study. *Frontiers in Neural Circuits* **7**, 49 (2013).
249. Womelsdorf, T., Lima, B., Vinck, M., Oostenveld, R., Singer, W., Neuenschwander, S. & Fries, P. Orientation selectivity and noise correlation in awake monkey area V1 are modulated by the gamma cycle. *Proceedings of the National Academy of Sciences* **109**, 4302–4307 (2012).
250. Womelsdorf, T., Schoffelen, J. M., Oostenveld, R., Singer, W., Desimone, R., Engel, A. K. & Fries, P. Modulation of neuronal interactions through neuronal synchronization. *Science* **316**, 1609–1612 (2007).
251. Womelsdorf, T., Valiante, T. A., Sahin, N. T., Miller, K. J. & Tiesinga, P. Dynamic circuit motifs underlying rhythmic gain control, gating and integration. *Nature Neuroscience* **17**, 1031–1039 (2014).

252. Woodbury, J. *Medical Physiology and Biophysics, Edited by Ruch, TC AND Fulton, JF* 1960.
253. Wurtz, R. H. Using perturbations to identify the brain circuits underlying active vision. *Phil. Trans. R. Soc. B* **370**, 20140205 (2015).
254. Zandvakili, A. & Kohn, A. Coordinated neuronal activity enhances corticocortical communication. *Neuron* **87**, 827–839 (2015).

#### COLOPHON

This document was typeset using the typographical look-and-feel `classicthesis` developed by André Miede. The style was inspired by Robert Bringhurst's seminal book on typography "*The Elements of Typographic Style*". `classicthesis` is available for both  $\text{\LaTeX}$  and  $\text{\LyX}$ :

<https://bitbucket.org/amiede/classicthesis/>

*Final Version* as of January 25, 2022 (`classicthesis` version 1.0).